Development and Application of Enzymatic Biosensors in the Investigation of Organophosphate Toxicity and Neurotransmission

By

Ethan Stuart McClain

Dissertation

Submitted to the Faculty of the

Graduate School of Vanderbilt University

in partial fulfillment of the requirements

for the degree of

DOCTOR OF PHILOSOPHY

in

Chemistry

May 14, 2021

Nashville, Tennessee

Approved:

David E. Cliffel, Ph.D.

John A. McLean, Ph.D.

John P. Wikswo, Ph.D.

David W. Wright, Ph.D.

To my family.

ACKNOWLEDGEMENTS

The research presented within this dissertation would not have been possible without the help and support of many people along the way. First, I would like to thank my advisor, Dr. David E. Cliffel, for his guidance throughout graduate school and providing me the opportunity to come to Vanderbilt and join his research group. I would also like to thank my dissertation committee members Dr. John A. McLean, Dr. John P. Wikswo, and Dr. David W. Wright for their support, and for challenging me to be a better scientist. Additionally, I would like to thank the many collaborators that assisted in this work: Dr. Diana Neely, Dr. Jacquelyn Brown, Dr. Jody May, Dr. Kazi Tasneem, and Dr. Mason McClatchey. Their expertise contributed greatly to the projects that we worked on together. I would like to thank my colleagues in the Cliffel Lab, both past and present, for being great coworkers and friends. I am especially appreciative of Dr. Dusty Miller and Sara Melow for their help and advice over the last five years. Finally, I certainly would not have made it this far without the love and support of my family. Thank you to my parents, especially, for always supporting me in everything that I do.

TABLE OF CONTENTS

DEDICATION ii

ACKNOWLEDGMENTS iii

LIST OF FIGURES vi

LIST OF TABLES viii

Chapter

I. INTRODUCTION 1

II. EXPERIMENTAL METHODS AND DATA ANALYSIS 9

Cleaning Screen-Printed Electrodes 9
Creation of Ag/AgCl Reference Electrode 12
Deposition of Enzyme Films 13
Performing Electrochemical Analysis 14
Data Analysis 16

III. DEVELOPMENT OF A GLUTAMATE BIOSENSOR AND THE REAL-TIME ANALYSIS OF CELLULAR RESPONSE TO GLUTAMATE-INDUCED EXCITOTOXICITY 19

Introduction 19
Experimental 23
Results and Discussion 28
Conclusions 38
Acknowledgments 38

IV. EFFECTS OF ORGANOPHOSPHATE TOXICITY ON ACETYLCHOLINE METABOLISM IN A MODEL BLOOD-BRAIN BARRIER 40

Introduction 40
Experimental 44
Results and Discussion 48
Conclusions 61
Acknowledgements 62

V. DEVELOPMENT OF A BIOSENSOR FOR THE SIMULTANEOUS DETECTION OF MULTIPLE NEUROTRANSMITTERS 63

Introduction 63

Experimental 67
Results and Discussion 74
Conclusions 88
Acknowledgements 88

VI. MODELING DOWNSTREAM ELECTROCHEMICAL ANALYSIS OF AN ORGAN-ON-A-CHIP SYSTEM 89

Introduction 89
Experimental 91
Results and Discussion 96
Conclusions 106
Acknowledgements 107

VII. CONCLUSIONS AND OUTLOOK 108

Appendix

A. FIBROUS ENCAPSULATION AND THE DELAY OF CONTINUOUS GLUCOSE MONITOR READINGS 114

Introduction 114
Experimental 116
Results and Discussion 117
Conclusions 121
Acknowledgements 121

B. DATA ANALYSIS WITH MATLAB 122

REFERENCES 126

CURRICULUM VITAE 143

LIST OF FIGURES

Figure **Page**

1.1 Enzymatic Mechanisms for Neurotransmitter Biosensors....3

2.1 Cyclic Voltammogram of Clean Platinum Electrode....11

2.2 Drawings of Microformulator Pump and Valve System....15

2.3 Cyclic Voltammogram of Hydrogen Peroxide and Amperometric Calibration....17

3.1 Drawings of Glutamate-Sensitive Electrode Array and μCA Bioreactor....22

3.2 Stability of Glutamate Sensor Over 72 Hours....29

3.3 Representative Calibration Curve of Glutamate Sensor....31

3.4 Real-Time Data of Glutamate Uptake by PC12 Cells....33

3.5 Glutamate Uptake by PC12 Cells Across Two Exposures....35

3.6 Real-Time Data of Glutamate Uptake by CC3 and TSP8-15 Cells....36

3.7 Glutamate Uptake by CC3 and TSP8-15 Cells Exposed to 50 and 500 μM Glutamate....37

4.1 Schematic of Acetylcholine and Chlorpyrifos Biochemistry....42

4.2 Enzyme Kinetics and Sensor Parameters for the Acetylcholine Sensor....50

4.3 Stability of Acetylcholine Sensor Over 68 Hours....51

4.4 Acetylcholine Sensor Response to CPF and CPO....53

4.5 Inhibition and Regeneration of an Acetylcholine Sensor....55

4.6 Electrochemical Analysis of Acetylcholine Concentration in NVU Eluate....57

4.7 Distribution of CPF and its Primary Metabolites Within the NVU....59

4.8 PDMS Absorption of CPF....60

5.1 Drawings of the 8-Channel Electrode, Microfluidic, and Housing....66

5.2 Stability of mPD Layer Over One Week....77

5.3 Representative Calibrations of Neurotransmitter Sensors on the 8-Channel Electrode 79

5.4 Stability of Neurotransmitter Sensors 82

5.5 Individual Calibrations of the Neurotransmitter Sensors....84

5.6 Dopamine Interference and Correction....85

5.7 Glutamate Uptake by CE3 Astrocytes Treated with CPF or TBOA 87

6.1 Experimental Setup for Monitoring Analyte Consumption and Production 92

6.2 Downstream Measurement of the Consumption of Ferricyanide 98

6.3 Downstream Measurement of the Production of Ferrocyanide 100

6.4 Crosstalk Between Electrodes with Normal Flow Configuration....102

6.5 Crosstalk Between Electrodes with Inverted Flow Configuration 103

6.6 Effects of Membrane Pore Size and Flow Rate on NVU Permeability....105

A.1 Electrochemical Data Collected Using Continuous Glucose Monitor 118

A.2 Natural Logarithm Versus Time Used for T_{50} Calculation....119

LIST OF TABLES

Table **Page**

2.1 Amperometric i-t Parameters for Cleaning Electrodes 10

2.2 Cyclic Voltammetry Parameters for Assessing SPE Cleanliness 10

2.3 Sweep-Step Parameters for Silver Plating an SPE 12

2.4 Enzyme Details for Sensor Modification 13

5.1 Testing mPD Deposition Times and Concentrations 75

5.2 Characteristics of Neurotransmitter Enzyme Sensors 80

5.3 Optimization of Adenosine Detection Parameters 81

6.1 Consumption of Ferricyanide by Upstream SPE 97

6.2 Production of Ferrocyanide by Upstream SPE 99

A.1 T_{50} Measurements of a Continuous Glucose Monitor *In Vitro* 120

Chapter I

INTRODUCTION

Neurotransmitters are a group of over 100 signaling molecules involved in a variety of biological functions that encompass both physical and psychological processes in humans. These chemical messengers can take many different forms, from amino acids and peptides to monoamines and catecholamines. Depending on binding location, neurotransmitters can function as excitatory or inhibitory—with both types being essential to proper modulation of synaptic transmission.[1] Excitatory neurotransmitters, like glutamate and dopamine, increase the likelihood of neuronal signaling and are responsible for processes ranging from learning and memory to motor control and emotional regulation.[2,3] Gamma-aminobutyric acid (GABA) and adenosine are examples of inhibitory neurotransmitters and can act as central nervous system depressants—promoting sleep.[4] Adenosine has also been demonstrated to stimulate differentiation and myelination of neurons, both integral processes for proper neuronal development.[5] In addition to these two classifications, neurotransmitters like acetylcholine can serve as neuromodulators within the brain. Neuromodulators can alter the state of whole groups of neurons at the same time, modifying their response to subsequent stimuli.[6] Due to the various functions of neurotransmitters, the capability to detect and quantify them is essential to understanding the mechanisms behind many biological processes.

The development of biosensors that can monitor the real-time, dynamic changes in multiple neurotransmitters is necessary to better understand neurological disorders and their treatments. The dysregulation of dopamine and acetylcholine equilibrium, for example, is known to be in part

responsible for decreasing motor function in the progression of Parkinson's Disease.[7] Monitoring neurotransmitters *in vivo* is made challenging due to the quick clearance of neurotransmitters from the extracellular space, as well as the low concentrations that are generally present.[8,9] The most widely used techniques for *in vivo* detection are microdialysis and fast-scan cyclic voltammetry (FSCV). In microdialysis, analyte present in the brain is perfused through a semi-permeable probe and collected for analysis—generally with high performance liquid chromatography and mass spectrometry.[10] Though sensitive, microdialysis generally suffers from a temporal resolution on the order of minutes. FSCV has a high temporal resolution but is complicated by the presence of many chemical species with similar oxidation potentials, as well as neurotransmitters like glutamate and acetylcholine that require high potentials for FSCV detection.[11] To overcome these challenges, enzyme sensors have been developed for many neurotransmitters that maintain high temporal resolution while providing for more specific detection.

Enzyme sensors have been developed to detect a wide range of neurotransmitters, including glutamate, acetylcholine, dopamine, and adenosine.[12–15] Though some of these sensors—like acetylcholine and adenosine—require multiple enzymes to function, many utilize oxidase enzymes as their final step to generate hydrogen peroxide that can be oxidized at 0.6 V (vs. a Ag/AgCl reference) and detected electrochemically (**Figure 1.1**). Because dopamine oxidizes at 0.6 V on its own, tyrosinase is used to make the sensor more specific by converting the dopamine to dopamine-o-quinone—which can then be reduced at a negative potenital.[14] The main drawback to enzymatic sensors is their instability, as the degradation of the enzymes over time means frequent calibration is necessary for accurate measurements. While this makes their utilization within *in vivo* systems difficult, enzymatic biosensors are still a viable method to study neurotransmission.

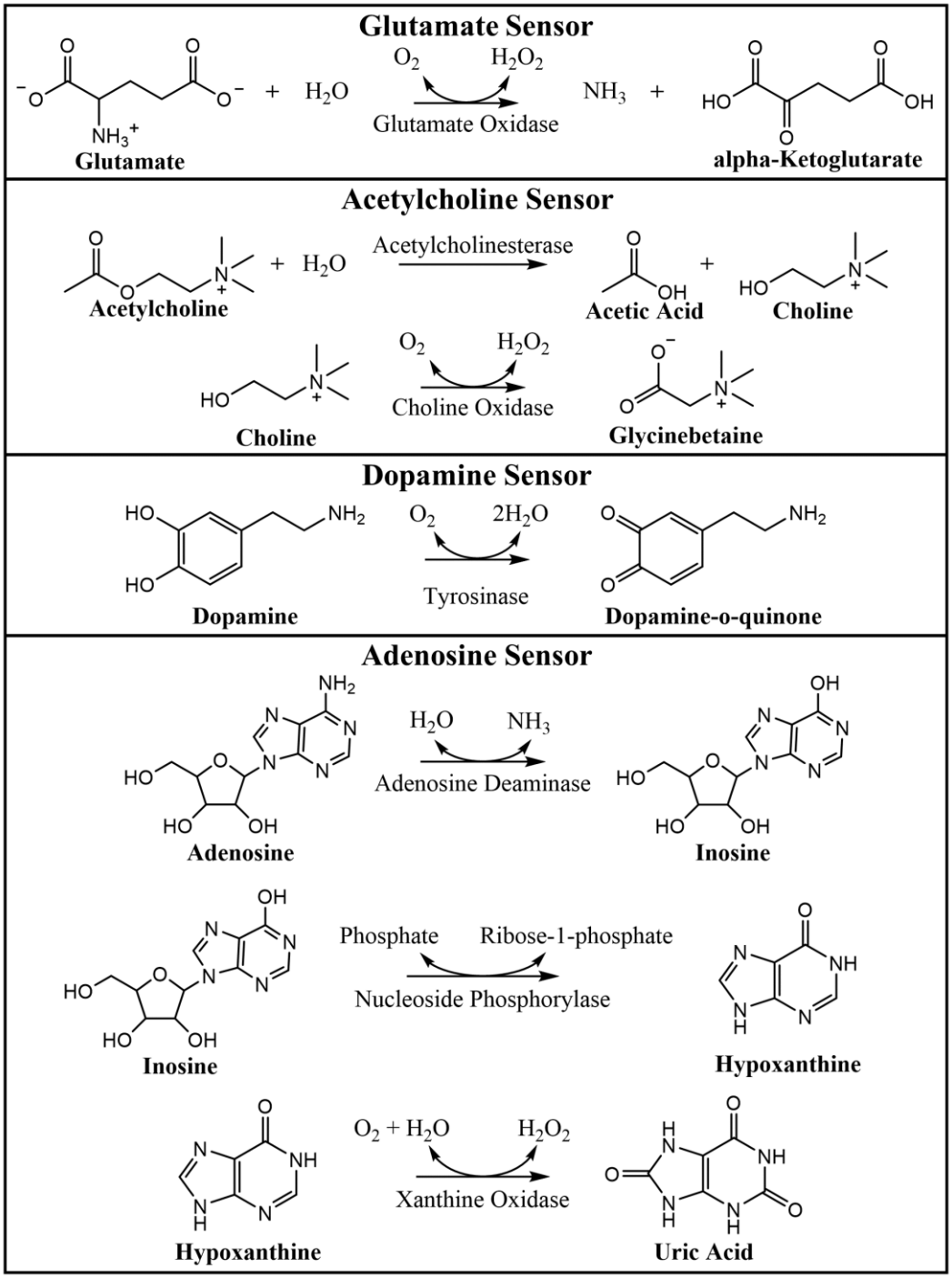

Figure 1.1. Enzymatic Mechanisms for Neurotransmitter Biosensors. Sensors for glutamate, acetylcholine, and adenosine utilize oxidase enzymes that produce hydrogen peroxide (H_2O_2), which can be electrochemically detected through oxidation at 0.6 V vs. Ag/AgCl. While dopamine is also oxidized at 0.6 V vs. Ag/AgCl, there is not enough specificity without the addition of enzyme. Tyrosinase oxidizes dopamine to dopamine-o-quinone, which can then detected through reduction at -0.2 V vs. Ag/AgCl providing for a more specific dopamine sensor.

The integration of electrochemical sensors with microfluidic systems provides a platform for automated calibration and analysis, and limits the effects of enzymatic degradation.[16,17] The further incorporation of these systems with organs-on-chips (OoCs) may allow for the *in vitro* analysis of biological analytes, including neurotransmitters, in real time.

OoCs are microfluidic cell culture systems that aim to reproduce the structure and physiological response of entire organs and tissues. Currently, OoCs are being developed for a wide range of human organs including the lung, heart, and liver—along with other systems like the blood-brain barrier and fetal membrane.[18–22] In many cases, these types of systems can be used in place of early-phase animal studies allowing for a reduction in the number of animals necessary for toxicological experiments.[23] Additionally, OoC systems provide for a more controlled experimental environment, and can produce results more accurately representative of human response than animal studies due to the flexibility they provide in cell selection. A significant effort has been put towards designing OoC systems that can contain the cell types necessary to accurately represent the brain and blood-brain barrier (BBB) environment.

The BBB is a major component in maintaining the health of the brain, regulating the transport of nutrients while also preventing the influx of pathogens and toxicants into the brain.[24] The BBB requires the presence of multiple cell types including neurons, endothelial cells, astrocytes, and pericytes—each necessary for developing a barrier with the proper structure and cell to cell communication to function.[25] To mimic BBB structure, models have been developed that utilize porous membranes to separate the vascular side of the barrier from the neuronal side. These models can then be used to test the response of the barrier to toxicant exposure, or even the ability of novel drugs to cross into the brain.[21,26] Due to their microfluidic nature, these *in vitro*

systems are then well suited to the integration of analysis through a variety of methods, including *in situ* and in line.

Fully recognizing the potential of OoC systems requires the integration of analysis platforms that can provide high temporal resolution for an extended period. This provides for the precise assessment of the dynamic responses of these organ systems following toxicant or drug exposure. Several analysis platforms have been reported for use with OoCs in the analysis of glucose, lactate, and oxygen.[27,28] Additionally, microfluidic systems with integrated biosensors have been designed that can be used downstream of an OoC system.[17] However, many of these systems are limited in their integration or the time frame that they can be used. Analysis of analytes downstream of the organ system, while providing some technical benefits compared to *in situ*, may suffer from diffusion and liquid mixing—lowering the resolution of the collected data. Further research is needed into the effects of downstream analysis on collected data, and in the design of simple, biocompatible platforms that can perform real-time analysis over biologically relevant time frames.

This dissertation presents the development and application of multiple enzymatic biosensors to study a variety of neurotransmitters and their actions within biological systems. Chapter 3 presents a glutamate sensor and its application to studying glutamate metabolism. The microclinical analyzer (μCA) is used in this work as a bioreactor, with cells grown on a transwell membrane and placed directly on the sensor surface enabling the real-time analysis of glutamate uptake. As a proof-of-concept, PC12 cells are used to demonstrate the uptake of glutamate upon glucose starvation and depolarization of the cell membrane with KCl. Treatment with excitotoxic glutamate concentrations stimulated significant uptake, which not only relieves excitotoxicity, but

may indicate that the cells are using glutamate in place of glucose as a source of energy in the citric acid cycle.

Tuberous sclerosis complex (TSC) is a disease that manifests in the growth of hamartomas on the brain and other organs.[29] One of the main symptoms reported by those with TSC is seizures. A possible explanation as to the cause of the seizures is the dysregulation of glutamate transporters like excitatory amino acid transporter (EAAT) 1 and EAAT2.[30,31] These transporters are responsible for moving glutamate inside of the cell from the extracellular space. If not functioning properly, glutamate may build up outside of the cells—triggering excitotoxicity and seizures. Once again using the μCA as a bioreactor, astrocytes from patients with TSC were shown to take up less glutamate than astrocytes from control patients. This work demonstrates just one of many ways that electrochemical biosensors can be used to study cellular mechanisms in real time.

Chapter 4 presents a two-enzyme acetylcholine sensor and its characterization with the organophosphate (OP) pesticides chlorpyrifos (CPF) and chlorpyrifos oxon (CPO). CPF and one of its metabolites, CPO, are known to inhibit the function of the enzyme acetylcholinesterase—responsible for the breakdown of acetylcholine following its release by neurons.[32,33] The sensor, which contains acetylcholinesterase, was not inhibited upon exposure to CPF though the response was inhibited by CPO. This inhibition was shown to be linear with concentration, providing the ability to use the sensor for the biorecognition of CPO if desired.

Additionally, the sensor was applied to the analysis of eluate from a model blood-brain barrier (BBB), the neurovascular unit (NVU), that had been treated with 10 μM CPF for 24 hours. While toxicological experiments have traditionally been performed using animal models, organotypic models can use human cells to better represent human response to toxicants. Though the effects of CPF on the BBB are not well understood, the application of electrochemistry and

mass spectrometry to the analysis of model organ systems like the NVU can provide new insight. Analysis of CPF-treated NVUs with mass spectrometry showed only the downstream metabolite trichloropyridinol (TCP) in the vascular eluate, while neither CPF nor any of its metabolites were able to be quantified in the neuronal eluate. The acetylcholine sensor was used within the μCA to analyze eluate from both the vascular and neuronal chambers of the NVUs exposed to CPF. Though CPF was only introduced into the vascular chambers of the devices, acetylcholine levels were significantly elevated in both chambers—indicating substantial metabolic disruption.

Chapter 5 presents the development of a sensor for the simultaneous detection of multiple neurotransmitters, composed of two glutamate, acetylcholine, adenosine, and dopamine sensors on the 8-channel electrode. A sensor capable of monitoring multiple neurotransmitters simultaneously may provide for more in-depth analyses of biological systems. Here, both the adenosine and dopamine enzyme sensors were modified from previous works to function alongside the previously developed glutamate and acetylcholine sensors in the μCA system. The ability of an m-phenylenediamine (mPD) layer to block interference from ascorbic acid and dopamine was investigated and optimized. The detection parameters and stability of each enzyme sensor were determined, and the ability to monitor all four neurotransmitters simultaneously was demonstrated. Following characterization, the sensor was used to investigate the effects of CPF and DL-threo-β-benzyloxyaspartic acid on glutamate uptake in human induced pluripotent stem cell-derived astrocytes. DL-threo-β-benzyloxyaspartic acid, a known inhibitor of glutamate uptake, resulted in less uptake compared to the control. CPF, however, was shown to significantly increase glutamate uptake by astrocytes—indicating that CPF may dysregulate the metabolic processes of glutamate in the brain.

Chapter 6 presents an investigation into the effects of downstream electrochemical analysis with the μCA on the accurate quantification of analytes from OoC systems. As microfluidic OoC systems continue to be developed, questions arise as to the best way integrate analysis platforms. Analysis can be performed *in situ*—directly within the area being studied—or in line, which involves the connection of an analysis platform for downstream analyte detection. Here, a two-μCA setup was used to replicate an upstream OoC with *in situ* electrodes, and a downstream μCA for in-line detection. Low flow rates, such as 2 μL min^{-1}, were determined to be optimal for in-line quantification as higher flow rates resulted in greater concentration losses due to diffusion and mixing. In addition, the effects of flow rate, flow path, and electrode orientation on crosstalk within the μCA were studied. Crosstalk increased with decreasing flow rate and was higher between electrodes in the same flow path. Similarly, the effects of flow rate and membrane pore size on the permeability of an empty NVU were investigated—with permeability increasing as pore size and flow rate increased. Overall, the accurate analysis of OoC systems downstream is dependent upon many factors, and each should be carefully considered during the experimental design process.

The appendix of this dissertation presents a project that, though not related to neurotransmission, illustrates the versatility of electrochemical analysis. In Appendix A, the cause of significant delay in glucose measurements by continuous glucose monitors (CGMs) was studied. The CHI 1440 potentiostat was connected to a commercially available CGM to determine how quickly the CGM measured changes in glucose concentration *in vitro*. Similar experiments were then performed *in vivo*, with the conclusion being that fibrotic encapsulation of the CGM following implantation is responsible for the delay. Lastly, Appendix B presents the MATLAB code used to analyze much of the electrochemical data collected throughout the experiments discussed within this dissertation.

Chapter 2

EXPERIMENTAL METHODS AND DATA ANALYSIS

The studies presented within this dissertation are performed predominately using electrochemical methods. This chapter will provide general methods for preparing screen-printed electrodes, using the microclinical analyzer and microformulator systems, performing amperometric electrochemistry, and analyzing electrochemical data. Subsequent chapters will address more detailed methods specific to those studies.

Cleaning Screen-Printed Electrodes

Before the creation of the reference electrode or the deposition of enzyme films, all electrodes on the screen-printed electrode (SPE) must be cleaned. This process is first done with 1 M nitric acid, followed by 0.5 M sulfuric acid. Cleaning is carried out within a small beaker, with the electrode to be cleaned attached to an edge card connector and the electrodes completely submerged in solution. The working cables (green or yellow) of the potentiostat, either the CHI 1440 or CHI 1030, are attached to the edge card connector endings that are in contact with the electrodes that require cleaning. The reference (white) cable is attached to an external Ag/AgCl reference containing a 3 M KCl solution. The counter (red) cable is attached to a platinum mesh electrode that has been flame polished using a Bunsen burner. Both the reference and counter electrodes are placed in the cleaning solution with the SPE. The technique on the CH Instruments software is set to *Amperometric i-t*, and the parameters are set as in **Table 2.1**. Following cleaning with nitric and sulfuric acid, the electrodes are rinsed and resubmerged in the sulfuric acid solution to assess the cleanliness of the SPE. To do this, the potentiostat technique is set to *Cyclic*

Voltammetry, and the parameters are entered as in **Table 2.2**. If clean, the cyclic voltammogram should look like **Figure 2.1**. If not, the cleaning process with nitric acid and sulfuric acid may be repeated. Once clean, the SPE is ready for plating and creation of the Ag/AgCl reference electrode. Both the 3-electrode and 8-channel SPEs were designed in house and purchased from Pine Research (Durham, NC). The CHI 1030 and 1440 potentiostats were purchased from CH Instruments (Austin, TX).

Parameter	Setting
Initial E (V)	6 (for H_2SO_4) 3 (for HNO_3)
Sample Interval (s)	1
Sampling Time (s)	300
Quiet Time (s)	0
Scales During Run	1
Sensitivity (A/V)	1e-003
E1 On	Selected

Table 2.1. Amperometric i-t Parameters for Cleaning Electrodes. SPEs are first cleaned in 0.5 M H_2SO_4 followed by 1 M HNO_3. The potential, sensitivity, and on/off status is input for each electrode being cleaned.

Parameter	Setting
Initial E (V)	-0.2
High E (V)	-0.7
Low E (V)	-0.2
Initial Scan Polarity	Positive
Scan Rate (V/s)	0.5
Sweep Segments	5
Sample Interval	0.001
Quiet Time (s)	2
Sensitivity (A/V)	1e-004

Table 2.2. Cyclic Voltammetry Parameters for Assessing SPE Cleanliness. Cyclic voltammogram is taken in H_2SO_4. All electrodes being cleaned are checked.

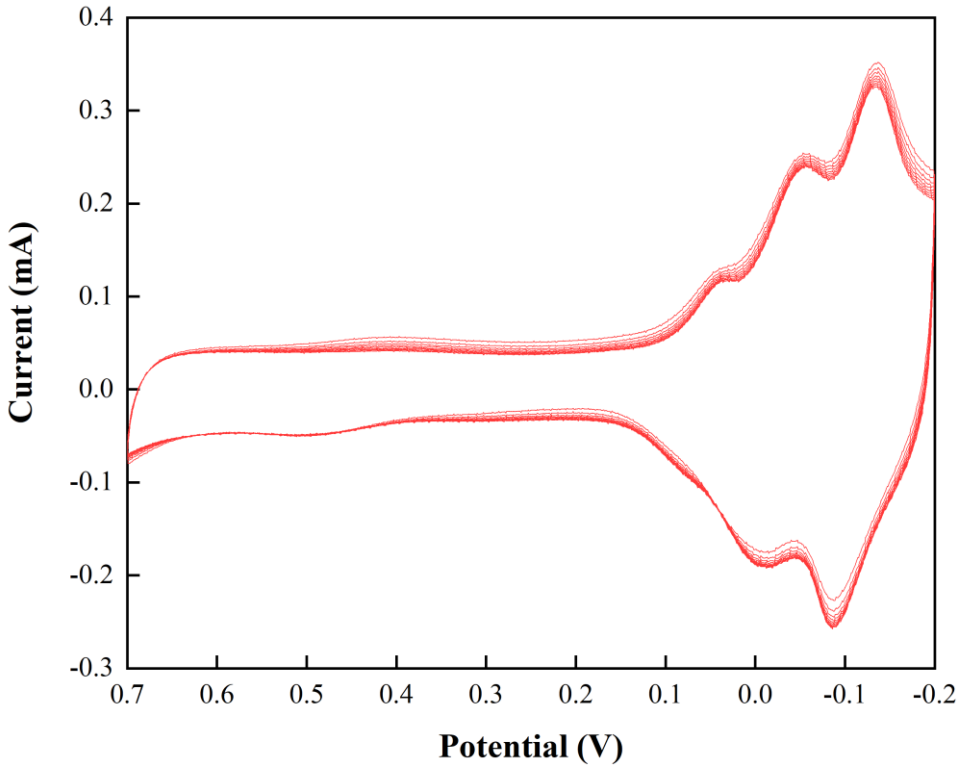

Figure 2.1. Cyclic Voltammogram of Clean Platinum Electrode. Following cleaning with 1 M HNO_3 and 0.5 M H_2SO_4, an SPE was electrochemically cycled in 0.5 M H_2SO_4 as detailed in *Table 2.2*. If cleaned properly, the voltammogram shows three distinct reduction peaks.

Creation of Ag/AgCl Reference Electrode

Following cleaning of the electrodes, the reference electrode can be plated with silver and agitated in an $FeCl_3$ solution to create the Ag/AgCl reference electrode.[17] On the 3-electrode SPE, either the 19 mm^2 band electrode can be plated and used as both reference and counter, or the 0.08 mm^2 band electrode can be plated as the reference with the larger band electrode as the bare platinum counter. The 8-channel SPE has a circular electrode for plating with silver and a separate large rectangular electrode to serve as the counter. The electrode to be plated is placed in a solution of 0.3 M $AgNO_3$ in 1 M NH_3 with a stir bar. The external reference and counter are connected and submerged in solution as before, and the first working cable is connected to the electrode that is going to be plated. The plating procedure is performed using the sweep-step function of the CHI potentiostats, with the parameters for the technique listed in **Table 2.3**. The procedure is run while the solution is stirring. Following silver plating, the electrode is rinsed with deionized water and agitated in a solution of 50 mM $FeCl_3$ for approximately 60 seconds. The electrode is then rinsed again and stored in a dark place until use to prevent oxidation of the reference electrode.

Parameter	**Sequence 1**	**Sequence 3**	**Parameter**	**Setting**
Initial E (V)	0.3	0.95	Initial E (V)	0.3
Final E (V)	0.95	-0.15	Sweep S.I. (V)	0.001
Scan Rate (V/s)	0.5	0.5	Step S.I. (s)	0.002
Parameter	**Sequence 2**	**Sequence 4**	Quiet Time (s)	0
Step E (V)	0.95	-0.15	Sensitivity (A/V)	1e-003
Step Time (s)	30	450	E1	ON

Table 2.3. Sweep-Step Parameters for Silver Plating an SPE. Sweep-step parameters are entered as above with all other settings left as default.

Deposition of Enzyme Films

Following cleaning and plating of the SPE, enzyme films can be deposited onto the electrode surface to make the SPE specific to the analyte of interest. To begin, 50 mg of bovine serum albumin (BSA, Fraction V) is dissolved in 800 µL of 50 mM phosphate buffer solution. Powdered enzyme is then dissolved in this BSA solution to the desired concentration (**Table 2.4**). At this point, enzyme can be stored at -18 °C until needed or used immediately. Before depositing onto the electrode surface, glutaraldehyde (25% in water) is added to the enzyme solution to a concentration of 1% by volume (2% for acetylcholine enzyme solution) and vortexed for ~5 seconds before being drop cast onto the working electrodes. If using the 3-electrode SPE, 1 µL is deposited onto the electrode surface. Only 0.5 µL is used if modifying the smaller 8-channel working electrodes. SPEs are air dried for at least an hour before use.

Enzyme	Sensor	State	Concentration (units/µL)
Glutamate Oxidase	Glutamate[12]	Solid	0.05
Acetylcholinesterase	Acetylcholine[13]	Solid	1.4
Choline Oxidase	Acetylcholine	Solid	0.15
Tyrosinase	Dopamine	Solid	72
Adenosine Deaminase	Adenosine	Liquid	1.0
Nucleoside Phosphorylase	Adenosine	Solid	0.1
Xanthine Oxidase	Adenosine	Solid	0.1

Table 2.4. Enzyme Details for Sensor Modification. Solid enzymes are dissolved in BSA solution before glutaraldehyde addition and casting onto the electrode surface. In the case of acetylcholine and adenosine, all enzymes needed are mixed before the addition of glutaraldehyde. Adenosine deaminase, provided as a liquid, was added as is to the enzyme solution. Glutaraldehyde concentration was adjusted based on the amount of BSA in solution (see Chapter 5).

Performing Electrochemical Analysis

Once the deposited enzyme is dry, the SPE is inserted into the microclinical analyzer (μCA) and connected to the microformulator. The μCA and microformulator have previously been used to perform a variety of electrochemical experiments with the 3-electrode SPE.[12,13,17] Briefly, the μCA is opened and the 3-electrode SPE is inserted. Applying a few drops of water on top of the electrode surface can help keep air out while the device is closed. To close the device, magnets are aligned, and the screws are tightened down. If using the 8-channel SPE, a polydimethylsiloxane (PDMS) fluidic is used in place of the μCA housing. The PDMS fluidic is placed on top of an 8-channel SPE that has been covered in water to prevent bubbles. Careful consideration should be given to aligning the fluidic channels with the electrodes. Application of a thin layer of ethanol to the channels of the fluidic can assist in keeping bubbles from forming upon fluidic placement. Once the fluidic is properly positioned, the housing is screwed down to hold the fluidic in place.

With the sensors in place, the microformulator is connected and an experimental protocol developed. The microformulator is a pump and valve system that can be used with both the 3-electrode and 8-channel SPEs to assist in calibration and sample analysis (**Figure 2.2**). Flow rates of the pump can range from 2 μL min^{-1} up to nearly 1 mL min^{-1}. The valve is available in 5 and 24 port variations, allowing for flexibility in the number of calibrants or samples that can be run in one experiment. Prior to performing an experiment, pump flow rate should be checked if necessary, and the valve tared using the AMPERE software to ensure proper function. Tubing from the valve is then inserted into the calibrants or samples. Generally, the sensor is first calibrated followed by any samples being analyzed—with a buffer solution in between each calibrant and sample to set an electrochemical baseline. Prior to electrochemical analysis, the tubing from each sample to the valve ball bearings is primed with the solution to be analyzed to

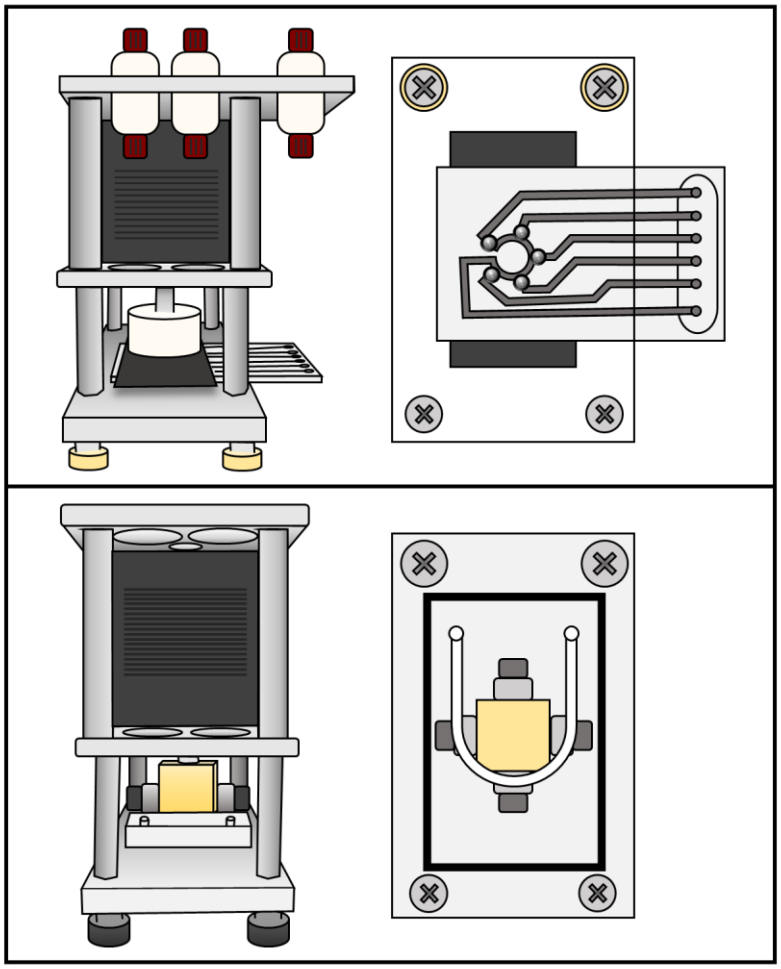

Figure 2.2. Drawings of Microformulator Pump and Valve System. Top) 5-port rotary planar valve and Bottom) rotary planar pump, both used in conjunction with the microclinical analyzer to analyze calibrants and sample solutions and perform real-time electrochemical experiments. Both the pump and valve are shown from the front (left) and from underneath (right).

clear any unwanted solution from the tubing. Most of the electrochemical experiments within this dissertation were performed using the *Amperometric i-t* technique on the CHI 1440 or CHI 1030 potentiostats. The protocol is set up like the cleaning protocol in **Table 2.1**, with a few changes. For all sensors presented in this dissertation, except for dopamine, the potential is set to 0.6 V to oxidize the generated H_2O_2 (**Figure 2.3**). Dopamine analysis is performed at -0.2 V, as it utilizes a reduction reaction instead. The sample time may be changed depending on the experiment, and the sensitivity increased if necessary. Electrode potential is set for every electrode being used, and those electrodes are selected as ON. The μCA, microformulator, and AMPERE software discussed in this section were purchased from the Vanderbilt Institute for Integrative Biosystems Research and Education (Nashville, TN).

Data Analysis

The analysis of data generated by 1030 and 1440 CHI potentiostats generally requires the use of other software, such as Microsoft Excel. For the experiments reported on within this dissertation, potentiostats were set up to record a new data point every second—sometimes resulting in tens of thousands of data points. To cut down on the number of data points, and increase experimental accuracy and precision, some simple MATLAB scripts were written allowing the user to find the average and standard deviation of a set number of data points (**Appendix B**). The output of this script results in a substantially lower number of data points, making the creation of calibration curves and analysis of sample data more efficient.

To begin the analysis process, the collected data must be converted into a text file. This is done using the 1030 or 1440 potentiostat software. The data is put into an Excel spreadsheet and saved as a .xlsx. Following this, MATLAB is opened and the data_application.m file is run. A

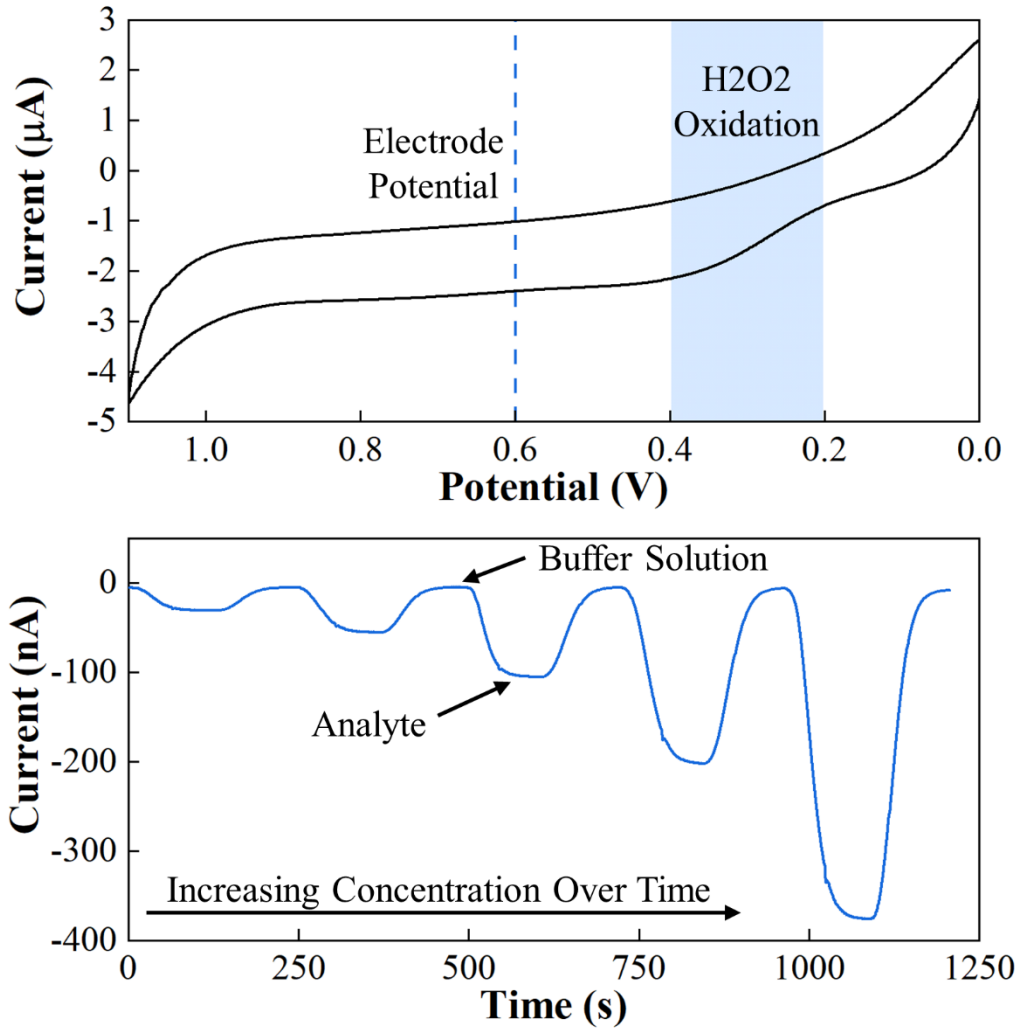

Figure 2.3. Cyclic Voltammogram of Hydrogen Peroxide and Amperometric Calibration. Top) Cyclic voltammogram of H_2O_2 demonstrating its oxidation from 0.2 to 0.4 V. Based on this, an electrode potential of 0.6 V was chosen for amperometric electrochemical experiments using H_2O_2 detection. Bottom) Representative electrochemical calibration for amperometric detection of an analyte through H_2O_2. Potential was held at 0.6 V vs. Ag/AgCl, with current magnitude increasing as analyte concentration increased.

window will appear with the options of *Read File*, *Average*, *Standard Deviation*, and *Exit Program*. After selecting *Read File*, the user is prompted to enter the name of the Excel file. There are also options to state which sheet of the file to import, or which columns. Sheets are specified as positive integers, e.g., 1, 2, 5 etc. If specifying a column range, it must be done in Excel notation (e.g., A1:A100 or B25:B50). Selecting OK loads in the file, and the window will reappear with the program options. From here, users can either exit the program or choose to find the average or standard deviation of a portion of the data. Selecting *Average* or *Standard Deviation* prompts the user to input the number of data points they would like to average or find the standard deviation of. If collecting only one data point per second—as is common in the *amperometric i-t* experiments within this dissertation—the number input is equivalent to the amount of time to be averaged in seconds. Users may choose to input the time that each calibration or sample was run (e.g., 120 seconds), or a smaller period can be input (e.g., 20 seconds) allowing users to find the average value at the steady state of a calibrant or sample. Using the same input for the *Standard Deviation* option provides the standard deviation of the averaged values, allowing users to choose the averaged value with the lowest standard deviation and more easily find the steady state area of the measurement.

Chapter III

DEVELOPMENT OF A GLUTAMATE BIOSENSOR AND THE REAL-TIME ANALYSIS OF CELLULAR RESPONSE TO GLUTAMATE-INDUCED EXCITOTOXICITY[1]

Introduction

Glutamate plays major roles in the proper function of organisms across domains, from *Escherichia coli* to humans. Not only is glutamate an amino acid involved in protein synthesis and a major metabolite in the citric acid cycle, but it is the also the most abundant excitatory neurotransmitter in the brain. As a neurotransmitter, glutamate is most prominently involved in synaptic plasticity—the ability to shape learning and memory through changes in synaptic strength.[2] During synaptic signaling, glutamate is released into the extracellular space to activate receptors before being taken back up by transporter proteins on the surface of astrocytes and neurons. Unlike some other neurotransmitters, like acetylcholine, there are no enzymes on the surface of these cells to break down glutamate.[34] When glutamate builds up in the extracellular space, the excessive activation of glutamate receptors triggers a process called excitotoxicity. This process can result in the damage or death of neurons, which may then lead to neurodegeneration.[35] Glutamate is essential in many metabolic and cognitive processes, with the dysregulation of these processes having significant consequences on health. Because of this, much effort has been put towards developing methods to detect glutamate.

[1]This chapter contains portions from the published research articles: 1. Miller, D. R.[=]; McClain, E. S.[=]; Cliffel, D. E. *J. Electrochem. Soc.* 2018, 165 (12), G3120–G3124.

The application of electrochemistry to the study of biological systems can result in low cost but selective methods of monitoring analytes of interest. Electrochemical sensors can be made selective using enzymes, many of which are oxidase enzymes, that catalyze a reaction resulting in a compound that can be electrochemically detected—like hydrogen peroxide. Enzymatic electrochemical sensors have already been developed for many different analytes, including glucose, lactate, acetylcholine, and cholesterol.[13,17,36] Other methods of detection, such as mass spectrometry, offer excellent sensitivity but can be costly or require extra sample preparation steps.[37] Enzymatic biosensors do present some challenges, namely enzymatic degradation, which necessitates frequent calibration.[3] Some biosensors, like the one presented here, can be coupled with microfluidic platforms—increasing throughput and providing the ability to automate the calibration and sample analysis process.[17] Additionally, these sensors can in many cases be placed in direct contact with the area of study as the electrodes can be made out of biocompatible materials, like platinum, and in sufficiently small sizes.[38]

The microclinical analyzer (μCA) is a low volume microfluidic device that can incorporate an enzymatically modified screen-printed electrode (SPE). The coupling of the μCA with a pump and valve microformulator system allows for the automated calibration of the enzymatic biosensor and analysis of eluate from the biological system of interest. The low volume (26 μL) of the microfluidic chamber enhances the temporal resolution of the platform and enables the detection of small metabolic changes—a necessity when studying mechanisms of glutamate transport. Because of the open chamber design, as opposed to microfluidic channels, cells can be positioned near the SPE surface for real-time, *in situ* analysis of cellular bioenergetics. Additionally, the flow of media over the cells creates flow-induced shear forces that aid in the recapitulation of the physiological environment—something that is difficult to accomplish in static cell culture. Similar

techniques have been used to grow organotypic cultures, which have been used to study pre-term birth, liver detoxification, and the blood-brain barrier.[21,39–41] In the μCA system, the incorporation of glial cells can enable the study of cellular response to glutamate-induced excitotoxicity in real-time.

Tuberous sclerosis complex (TSC) is a rare autosomal dominant genetic disease that manifests in the growth of non-cancerous tumors, hamartomas, on the brain and other organs.[29] These tumors have significant detrimental effects on neurological health, resulting in seizures and developmental delay. Patients with TSC report seizures in up to 90% of cases, with the seizures often beginning within the first year of life.[42] The dysregulation of excitatory amino acid transporter (EAAT) 1 and EAAT2 has been identified as one possible mechanism contributing to the effects seen in patients with TSC and other neurological disorders, as the buildup of extracellular glutamate may cause excitotoxicity and trigger seizures.[31,43] The application of real-time electrochemistry to the study of glutamate uptake in astrocytes from a TSC patient may provide insight into the uptake mechanisms, or lack thereof, of these cells and could in the future assist in the evaluation of novel therapeutics.

Here, a glutamate sensor is presented for the analysis of cellular bioenergetics in real time. The sensor was incorporated into the μCA analysis platform (**Figure 3.1**) and shown to be sensitive and stable throughout the temporal and concentration ranges necessary to study glutamate within biological systems. As a proof-of-concept, the system was used to quantify the uptake of glutamate by PC12 cells exposed to excitotoxic quantities. Following that, the uptake mechanisms of control astrocytes and diseased astrocytes from a TSC patient were investigated.

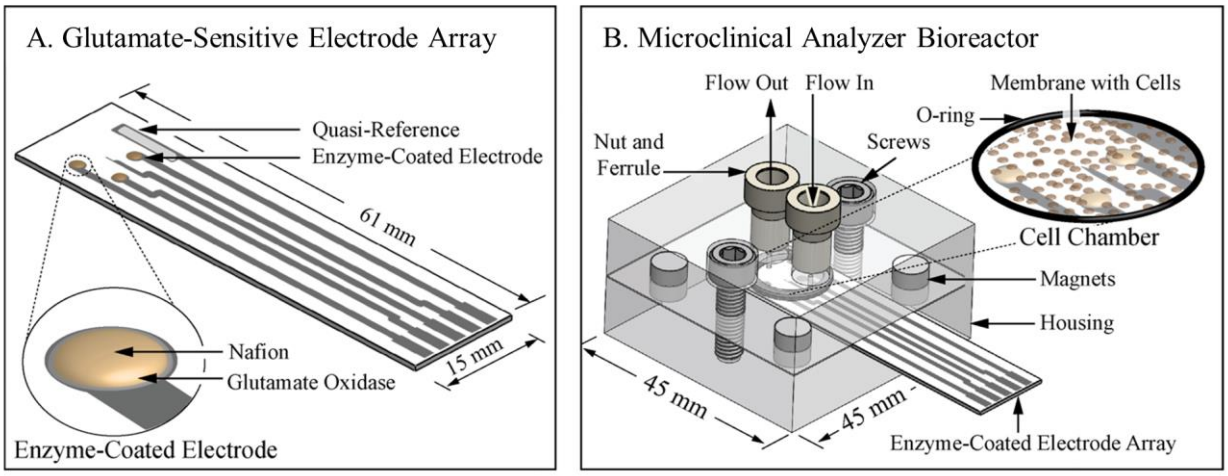

Figure 3.1. Drawings of Glutamate-Sensitive Electrode Array and μCA Bioreactor. A) The electrode array was screen-printed and modified as shown with glutamate oxidase and Nafion on three working electrodes and Ag/AgCl on the quasi-reference, before being inserted into B) the μCA bioreactor. The bioreactor housing separates so that the enzyme-coated SPE and membrane-immobilized cells can be inserted and removed. The magnets align the housing, SPE, and membrane, and the chamber is compressed by tightening the screws. Media was perfused through tubing (not pictured) that connects the housing's cell chamber to the media reservoirs, pumps, and valves (not pictured).

Experimental

Materials

PC12 cells were purchased from American Type Culture Collection (Manassas, VA). For cell culture and SPE modification, penicillin, streptomycin, T25 flasks, collagen type I, trypsin-EDTA, glutamate oxidase, bovine serum albumin, and glutaraldehyde were purchased from Sigma Aldrich (St. Louis, MO). Dulbecco's modified eagle's medium (DMEM) and Roswell Park Memorial Institute medium (RPMI) 1640 was purchased for cell culture from ThermoFisher (Waltham, MA). BrainPhys Neuronal Medium was purchased from StemCell Technologies (Cambridge, MA). Fetal bovine serum (FBS) was purchased from Atlanta Biologicals (Flowery Branch, GA). Nafion was purchased from Alfa Aesar (Ward Hill, MA). All transwells were purchased from Corning (Corning, NY). The μCA housing was designed by The Vanderbilt Institute for Integrative Biosystems Research and Education (VIIBRE, Nashville, TN) and fabricated from poly(methyl methacrylate) by the Vanderbilt Microfabrication Core (VMFC). Buna-N rubber O-rings, and screws were purchased from McMaster-Carr (Elmhurst, IL). Nut-and-ferrule fluid connections were purchased from IDEX (Oak Harbor, WA). Tygon tubing was purchased from Cole Parmer (Vernon Hills, IL). Magnets were purchased from K&J Magnetics (Pipersville, PA). SPEs were designed in house and purchased from Pine Research (Durham, NC). The rotary planar peristaltic micropump (RPPM, US patents 9,874,285 and 9,725,687 and applications claiming priority from US patent application 13/877,925), 5-port valves (VIIBRE, US patent 9,618,129), microcontrollers, and computer software were designed by and purchased from VIIBRE/VMFC. The CHI 1440 potentiostat was purchased from CH Instruments (Austin, TX).

Glutamate Sensor Fabrication

The SPE used here features five electrodes: three platinum disk electrodes and two band electrodes. The three platinum disk electrodes ($A = 1.8\ mm^2$) were used for enzymatic detection of glutamate. The larger of the two band electrodes ($A = 19\ mm^2$) was used as a Ag/AgCl quasi-reference. Glutamate oxidase from *Streptomyces* was dissolved in 800 mg/mL bovine serum albumin (BSA) in minimal buffer (2 mM phosphate buffer solution, pH 7) to 10 mg/mL (5 units/mg) and stored at -18 °C until use. When required glutamate oxidase solutions were thawed, glutaraldehyde was added to 0.25% wt/v, and the solution was vortexed for approximately five seconds. After mixing, 1 µL of the glutamate oxidase solution was drop cast onto the platinum disk electrode surface.[17] After drying for one hour, 1 µL of Nafion (5% v/v) was deposited on top of the enzyme. The sensors were then allowed to dry for an hour before calibration. If not used immediately, SPEs were stored in the dark to prevent oxidation of the Ag/AgCl reference.

Characterization of Glutamate Sensor

The limits of detection (LOD) and quantitation (LOQ), linear range, V_{max}, and K_m for the glutamate sensor were determined using the µCA as they were for other enzyme-based sensors.[12,17] Calibrations were performed within the µCA by monitoring the current generated by 21 calibrants ranging from 1 µM to 5 mM glutamate in buffer. Buffer for all experiments was made from a 50 mM potassium monobasic-sodium buffer (pH 7) and diluted in water with KCl to produce a 2 mM phosphate, 120 mM KCl, pH 7 buffer solution. Calibrants were sampled using the microformulator at a flow rate of 100 µL min^{-1} and monitored by a CHI 1440 potentiostat held at 0.6 V vs. Ag/AgCl. Linear regressions were performed on the linear range of the calibration data. The resulting slopes provided the sensitivity of the SPE. The limits of detection were calculated by multiplying the

error of the blank by three and dividing by the slope. The equation used for calculating the limit of quantitation was same, except the standard error was multiplied by ten instead of three. Because the enzyme saturation followed Michaelis-Menten kinetics, a hyperbolic function could be fit to the data to determine V_{max} and K_m. The resulting equation of the hyperbola provided coefficients corresponding to the values for V_{max} and K_m. All p-values calculated in this study were found by performing t-tests assuming unequal variance.

Sensor Stability During Use and Storage

To determine the stability of the sensor over experimentally relevant time periods, the current generated by a set of four glutamate calibrants (40 to 320 μM) in buffer was monitored every four hours for 72 hours. The sensitivity of each calibration was determined and compared to the sensitivity of the first calibration to determine how the response changed over time. In between glutamate calibrations, the baseline was set by measuring the current with the SPE in buffer.

PC12 Cell Culture

PC12 cells cryopreserved in liquid nitrogen were thawed, added to warmed DMEM culture media, and spun down (180 x g, 7 min). The supernatant was discarded, and the pellet was resuspended in 1 mL of DMEM with 5% FBS, 0.1 mg/mL penicillin, and 100 units/mL streptomycin. The resulting suspension was brought to ~1 million cells/mL and transferred to two T25 flasks. All cell culture flasks and transwells were coated in collagen type I overnight at room temperature before adding cells. The cells were grown to confluency (~10 days), trypsinized, (0.25% wt/v trypsin-EDTA) and plated onto two T25 flasks and a six-well PET track-etched 3.0

μm transwell. These cells were grown to confluency before use. All cell culture and cellular experiments were conducted at 37 °C and 5% CO_2 within an incubator.

PC12 Glutamate Microphysiometry

Confluent PC12 cells in a 6-well transwell were maintained in glucose-free RPMI media for twelve hours before being transferred into the μCA bioreactor. Before addition of the cells, the SPEs were calibrated. Calibrants were made in RPMI containing 100 mM KCl and ranged from 20 to 1000 μM glutamate. These calibrants were passed over the SPE at 20 μL min^{-1} while the current was monitored. During all valve switches, flow was momentarily paused to avoid pressure buildup. Following calibration, a transwell membrane with immobilized PC12 cells (10-14 days in culture) was removed from its plastic support and transferred to the μCA bioreactor. To transfer a membrane, the μCA housing was opened, and a membrane was placed on top of the SPE with the cells facing up. A second 3.0 μm membrane was placed on top to protect from flow-created shear forces and secure the cells in place. The two membranes were aligned with the SPE, and the housing was closed and compressed with screws to seal the cell chamber. During treatment, the bioreactor chamber was amperometrically monitored by three different glutamate oxidase-modified electrodes along the cell-covered membrane at 0.6 V vs. Ag/AgCl. The cells were equilibrated in RPMI for 30 minutes before RPMI with 100 mM KCl was passed over the cells for an additional 30 minutes. Lastly, RPMI with 1 mM glutamate and 100 mM KCl was passed over the cells for 30 minutes. This treatment cycle was repeated after a recovery period of 30 minutes of treatment with only RPMI. SPEs were calibrated every two treatment cycles. All calibrations and treatments were done at 37 °C in 5% CO_2 and at 20 μL min^{-1} in an incubator.

CC3 and TSP8-15 Glutamate Microphysiometry

The astrocytes used in this study were differentiated from two human induced pluripotent stem cell lines, CC3, a previously published cell line derived from a control female subject, and TSP8-15, derived from a female patient with TSC and epilepsy.[44] To assess glutamate homeostasis of CC3 and TSP8-15 astrocytes, cells were harvested and replated at equal density onto 12-well Transwell membranes (Corning #3462, Corning, NY). Glutamate uptake was quantified once the astrocyte cultures had reached confluency, and the presence of astrocytes confirmed by immunohistochemistry. Real-time electrochemistry was performed as with PC12 cells with some modifications. Calibrations were performed by monitoring the current generated by five solutions ranging from 0 to 500 μM glutamate in BrainPhys media. Following the transfer of a Transwell membrane with astrocytes (8-12 days in culture) to the μCA bioreactor, cells were equilibrated in BrainPhys without N2A and SM1 supplements (10 minutes) before 50 μM glutamate in the same medium was passed over the cells (10 minutes). BrainPhys was then passed over the cells again (10 minutes) before challenging the cells with 500 μM glutamate (10 minutes). As before, a flow of 20 μL min^{-1} was maintained for both the treatments and calibrations. Calibrations were performed before every two experiments. In analyzing uptake by PC12, CC3, and TSP8-15 cells, the glutamate concentration for a given current response was calculated using the slope and intercept generated from each calibration curve. The difference between the measured glutamate concentration and the glutamate concentration applied to the cells was then used to calculate cellular uptake.

Results and Discussion

Glutamate is one of the principal excitatory neurotransmitters in the brain and plays a key role in neurocognition, yet it is also excitotoxic in high quantities. The development of methods to detect glutamate is essential to advancing the understanding of glutamate biochemistry. Here, an SPE was enzymatically modified to be sensitive and selective to glutamate and incorporated into the μCA. As a proof-of-concept experiment, this versatile platform was used to study the response of PC12 model neurons to excitotoxic quantities of glutamate by placing the cells in direct contact with the SPE inside the μCA. Following this, two types of primary astrocytes—control CC3 and TSC-derived TSP8-15 cells—were incorporated into the μCA to further understand the effects of TSC on glutamate homeostasis.

To accurately measure the response of cells to glutamate, the developed sensor must span a temporal range sufficient to measure physiological and pathophysiological effects. In normal function, glutamate can be released from the synapse and subsequently taken up by neurons on a second time scale. On the other hand, extracellular glutamate levels during traumatic brain injury can build up to excitotoxic levels and take days to return to normal.[45] Therefore, a sensor that can respond on the second time scale while also remaining stable for hours to days is required to monitor the full range of glutamate biochemistry. Here, the glutamate sensor had a sub-second response time, making it suitable for monitoring typical synaptic signaling. The sensor also demonstrated stability over longer periods of time, maintaining 85 ± 6% of its signal following 72 hours of continuous use (**Figure 3.2**). The loss in sensor response over this period is likely due to decreasing enzyme activity.[46,47] Overall, the sensor demonstrated the quick response time and long-term stability necessary to monitor both glutamate signaling and trauma-induced excitotoxicity.

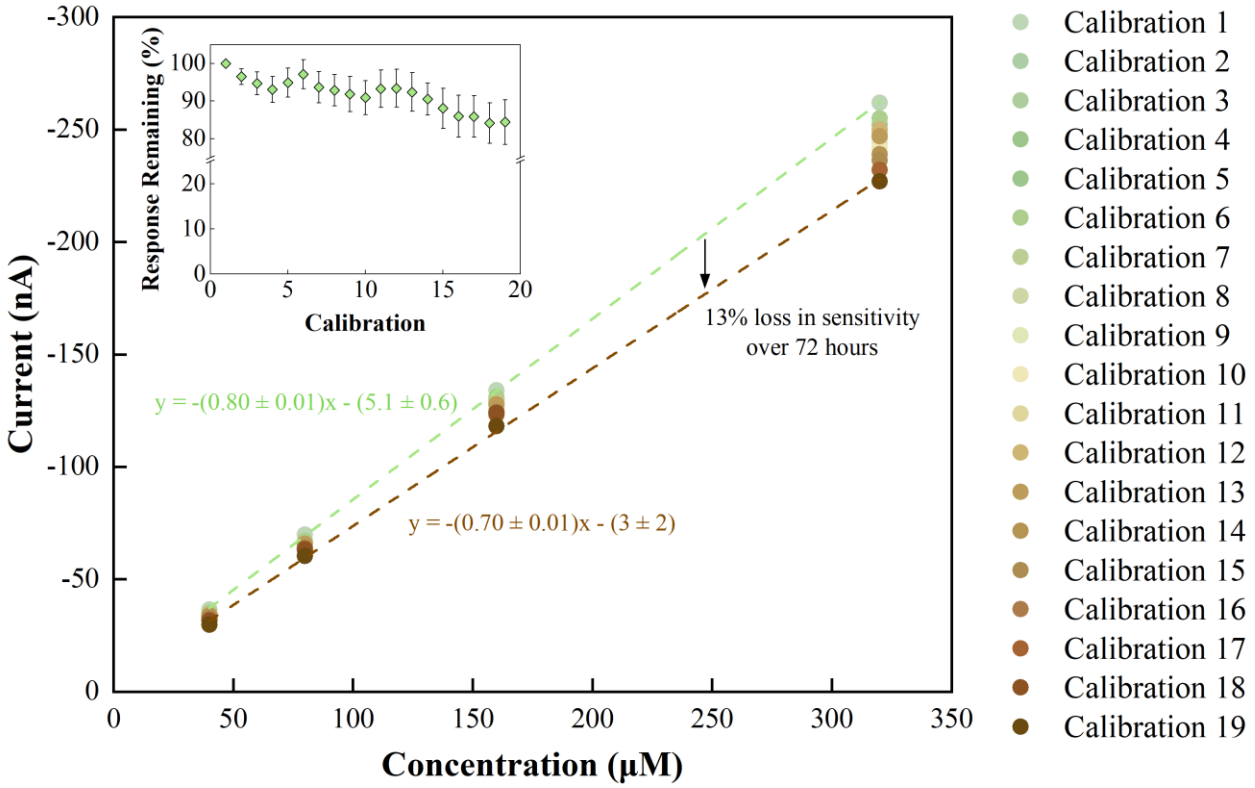

Figure 3.2. Stability of Glutamate Sensor Over 72 Hours. The response of the glutamate sensor to a set of 4 glutamate calibrants was tested every 4 hours for 72 hours. At the end of the experiment, the sensor retained 85 ± 6% of its original response. Inset: The sensitivity of each calibration was calculated and reported as a percentage of the first calibration sensitivity.

As further evidence of the glutamate sensor's biological relevance, the sensitivity of the sensor spanned from physiological to pathophysiological concentrations. Glutamate concentration within the brain is thought to range from low micromolar under normal conditions up to hundreds of micromolar in conditions of stress, such as stroke.[48,49] The sensitivity of the enzyme-modified electrodes, 0.17 ± 0.01 nA μM^{-1} mm^{-2}, enabled the detection of glutamate as low as 5 ± 1 μM and quantitation at 16 ± 4 μM (**Figure 3.3**). The upper limit of quantitation, past which the sensor could not linearly respond to glutamate, was 1 mM. Between these limits (16 μM to 1 mM), the sensor response was linear and able to be quantified, making the sensor suitable studying a wide range of biologicals systems.

To further understand the physiological usefulness of this sensor, values for V_{max} and K_m were calculated. As glutamate concentration exceeds 1 mM, the enzyme begins to saturate, and the current response of the sensor becomes hyperbolic. Eventually the amount of glutamate added has no effect on the current response, as the enzyme has reached its maximum rate of reaction, known as V_{max}. How V_{max} relates to concentration is dependent upon the affinity of the enzyme for its substrate, in this case glutamate. Using the same hyperbolic function, this affinity can be quantified by the K_m value, which is the concentration of substrate necessary to reach half of the V_{max}. Fitting the collected data to a hyperbolic function, the V_{max} and K_m values were determined to be 9.2 ± 0.2 pmol s^{-1} and 5.4 ± 0.2 mM, respectively. The importance of these values lies in the K_m of the enzyme compared to the concentration of the substrate under normal conditions. A low K_m value compared to physiological concentration means that, under standard conditions, the enzyme will turn over at a constant rate regardless of variations in concentration. On the other hand, a high K_m in comparison with physiological concentration results in an enzyme activity that varies with concentration. The K_m value of this sensor is much higher than even pathophysiological

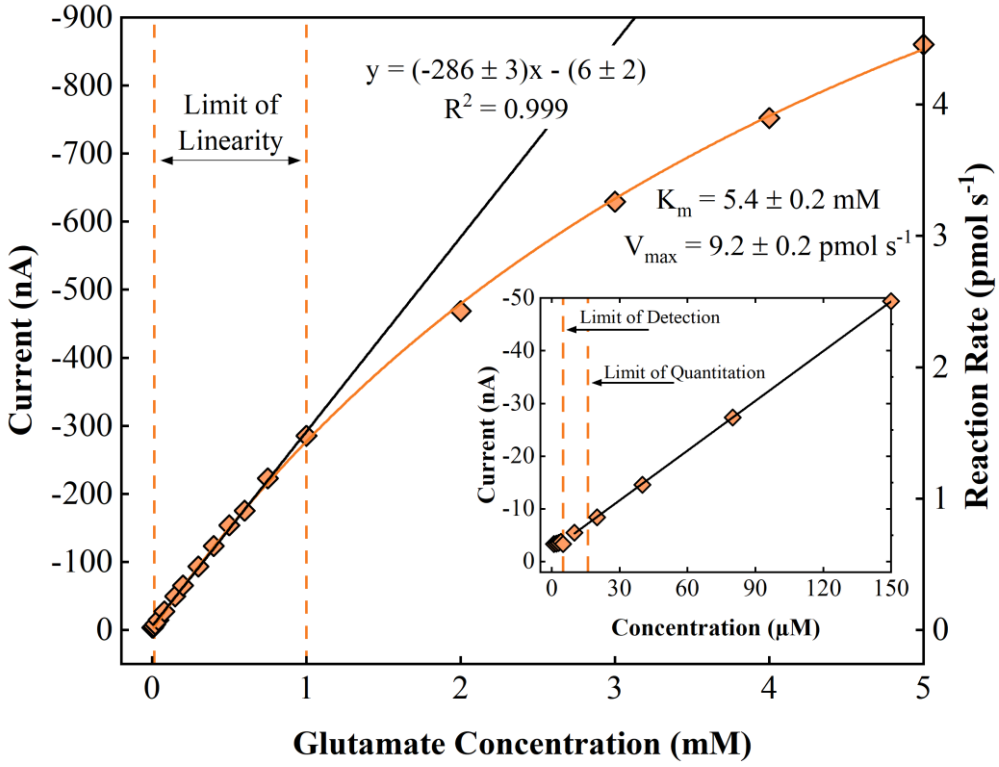

Figure 3.3. Representative Calibration Curve of Glutamate Sensor. Multiple calibrations were used to determine the limits of detection, quantitation, and linearity of the sensor as well as values for sensitivity, V_{max}, and K_m. Linear response was measured from 16 µM to 1 mM glutamate, with a sensitivity of 0.17 ± 0.01 nA μM^{-1} mm^{-2} (solid black line) in this region. The V_{max} and K_m were calculated by fitting the data to a hyperbolic function (solid orange line) and found to be 9.2 ± 0.2 pmol s^{-1} and 5.4 ± 0.2 mM, respectively. Inset: Focused views of lower glutamate concentrations delineating the limit of detection vs. the lower limit of linearity. The limit of detection was 5 ± 1 µM glutamate, while the limit of quantitation (lower limit of linearity) was 16 ± 4 µM.

concentrations of glutamate, indicating that the sensor is well suited for use in a wide range of biological systems without sacrificing sensitivity.

The μCA bioreactor and microfluidic system used in these experiments not only provides for automated calibration and analysis, but it also enhances analytical power. While microfluidics have been used in previous studies, the cells were spatially removed from the electrodes.[50] The μCA design accommodates cell placement directly on top of the electrochemical sensor. The low limit of quantitation of the glutamate sensor, combined with the small volume of the μCA bioreactor, allows for monitoring changes in glutamate such as those seen in synaptic signaling. This configuration improves analytical power by increasing signal-to-noise ratio and temporal resolution.[51]

In addition to increasing analytical efficiency, the microfluidic system can also impose shear stress on the cells that simulates those at physiological conditions. At a flow rate of 20 μL min^{-1}, the flow rate used for all cellular experiments, the cells experienced a calculated shear force of 0.32 dyne/cm^2 (assuming 25 °C, η = 0.89 cP, and laminar flow). In the brain, cells can experience anywhere from 0 to 40 dyne/cm^2.[52] The μCA can accommodate flow rates from the low μLs min^{-1} all the way up to nearly 1 mL min^{-1}, allowing for cellular response to be measured under a range of physiological conditions if desired.

To demonstrate the capability of the μCA to monitor cellular response to glutamate in real time, PC12 cells were exposed to glutamate and their response was electrochemically monitored. PC12 cells, derived from rat pheochromocytomas, have been extensively used as model neuronal cells to study glutamate metabolism, toxicity, and cell signaling.[53] Here, PC12 cells were glucose starved before being exposed to two 90 minute cycles of glucose-free media, 100 mM KCl, and 100 mM KCl plus 1 mM glutamate (**Figure 3.4**). Within the μCA bioreactor, glucose-starved

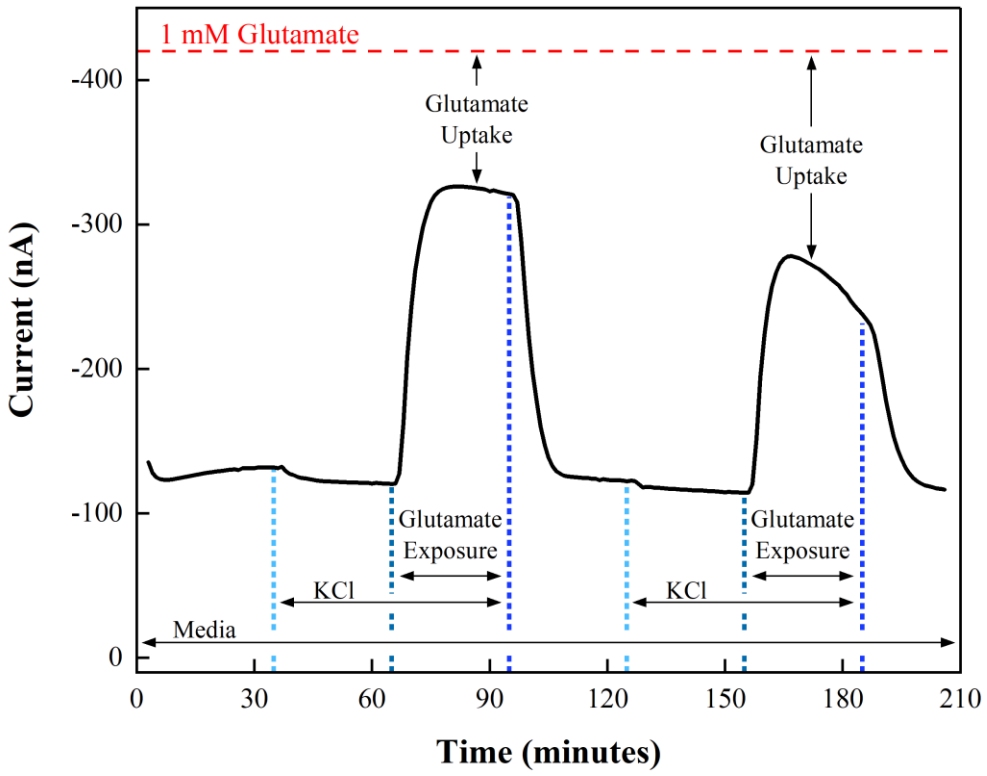

Figure 3.4. Real-Time Data of Glutamate Uptake by PC12 Cells. Over the course of the experiment PC12 cells were perfused with two cycles of media (glucose-free RPMI), 100 mM KCl, and 100 mM KCl plus 1 mM glutamate with each treatment lasting 30 minutes. The dashed red line indicates the current generated by the addition of 1 mM glutamate with no cells present. The decrease in current magnitude during glutamate treatment, compared to the current with no cells, indicates an uptake of glutamate by the PC12 cells.

PC12 cells took up 340 ± 60 nmoles of the provided glutamate (56 ± 10% or 11 ± 2 nmoles min^{-1}), which increased to 440 ± 40 nmoles (73 ± 7% or 15 ± 1 nmoles min^{-1}) during the second exposure (**Figure 3.5**). This uptake was not seen when cells were cultured in a glucose containing media. Extracellular exposure to glutamate triggers uptake by EAAT proteins.[54] Once inside the cell, glutamate may act as a fuel substrate for the citric acid cycle to assist in restoring bioenergetic homeostasis following prolonged depolarization and glucose starvation. An increase in the amount of glutamate taken up by the cells during the second treatment suggests that these neurotransmitter uptake systems were functional and may prioritize glutamate uptake to mitigate excitotoxicity. With this experiment serving as a proof-of-concept for monitoring cellular bioenergetics in real time within the μCA, future experiments can be designed to study more in-depth mechanisms of cellular function or disease—like TSC.

TSC is a rare genetic disease manifesting in part through seizures, which could be caused by excitotoxic quantities of glutamate present in the brain. Here, control (CC3) and diseased (TSP8-15) astrocytes were placed within the μCA and their response to both 50 μM and 500 μM glutamate was monitored electrochemically (**Figure 3.6**). Cells were first treated with 50 μM glutamate (10 nmoles), where CC3 cells took up 5.5 ± 0.7 nmoles compared to the TSP8-15 cells which took up 1.0 ± 0.8 nmoles. Increasing the concentration of glutamate to 500 μM glutamate (100 nmoles) resulted in an increase in uptake, where CC3 cells took up 74 ± 3 nmoles while the TSP8-15 cells took up 39 ± 5 nmoles (**Figure 3.7**). At both treatment concentrations, the uptake between the two cell types was significantly different (p-values $\leq$ 0.0006 and 0.0002 for 50 μM and 500 μM, respectively) with the diseased TSP8-15 cells taking up much less glutamate than the control. This reduced glutamate uptake by the TSC astrocytes may be at least in part

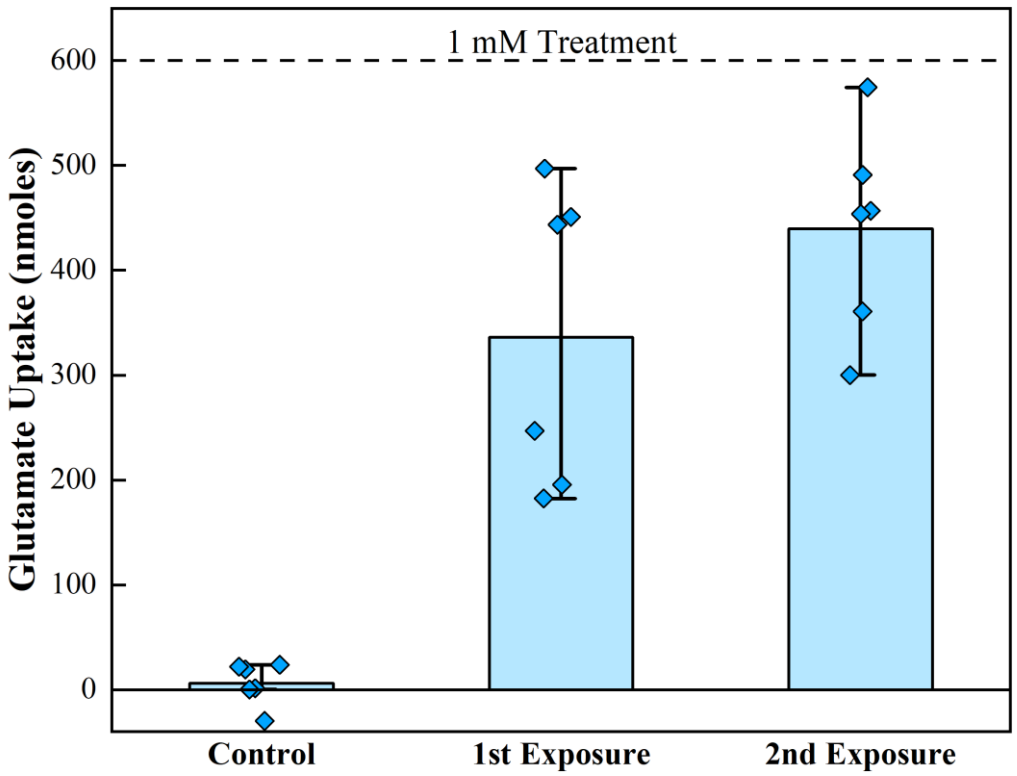

Figure 3.5. Glutamate Uptake by PC12 Cells Across Two Exposures. On average, cells took up 340 ± 60 nmoles (56 ± 10%) of the glutamate, which increased to 440 ± 40 nmoles (73 ± 7%) during the second exposure. All experiments are represented as the mean (n = 6) and standard error of the measurements, control vs. 1st exposure: $p \leq 0.002$: control vs. 2nd exposure: $p \leq 0.0001$: 1st exposure vs. 2nd exposure: $p \leq 0.18$.

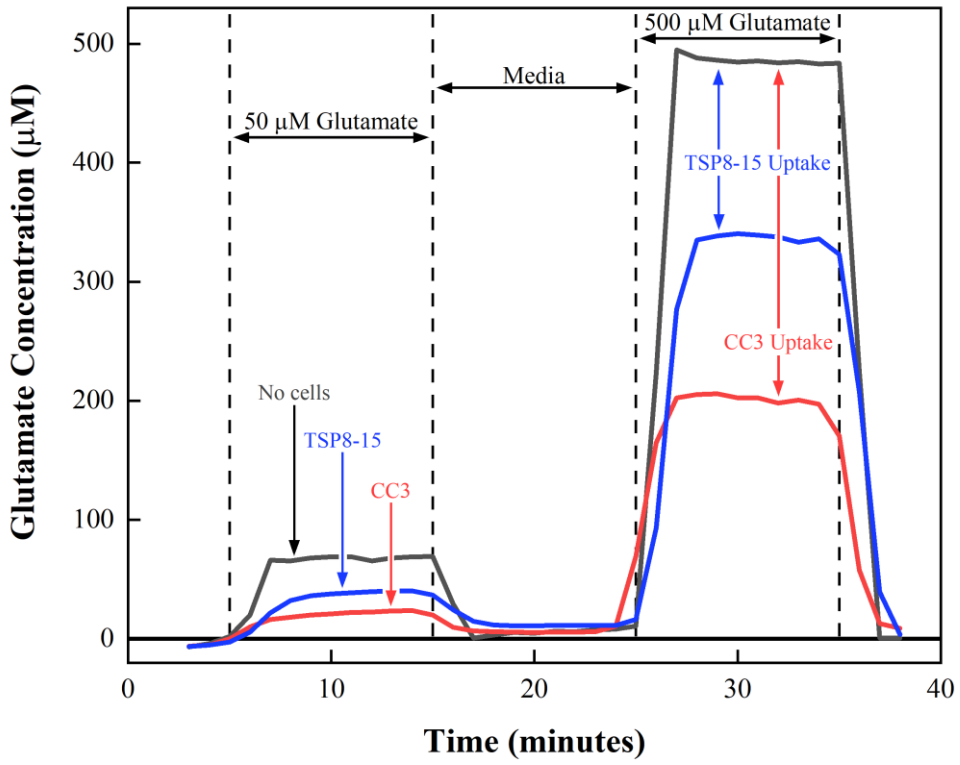

Figure 3.6. Real-Time Data of Glutamate Uptake by CC3 and TSP8-15 Cells. The µCA was used to monitor the response of control (CC3) and TSC (TSP8-15) astrocytes to glutamate stimulation in real time. CC3 and TSP8-15 cells were grown on 12-well Transwell membranes for 8 to 12 days before they were loaded into the µCA bioreactor and treated with both 50 and 500 µM glutamate in BrainPhys media, and their response was measured in real time. While both cell types took up glutamate, indicated by the decrease in current magnitude compared to the no cells data (gray), the diseased TSP8-15 cells (blue) took up significantly less glutamate than the CC3 control cells (red).

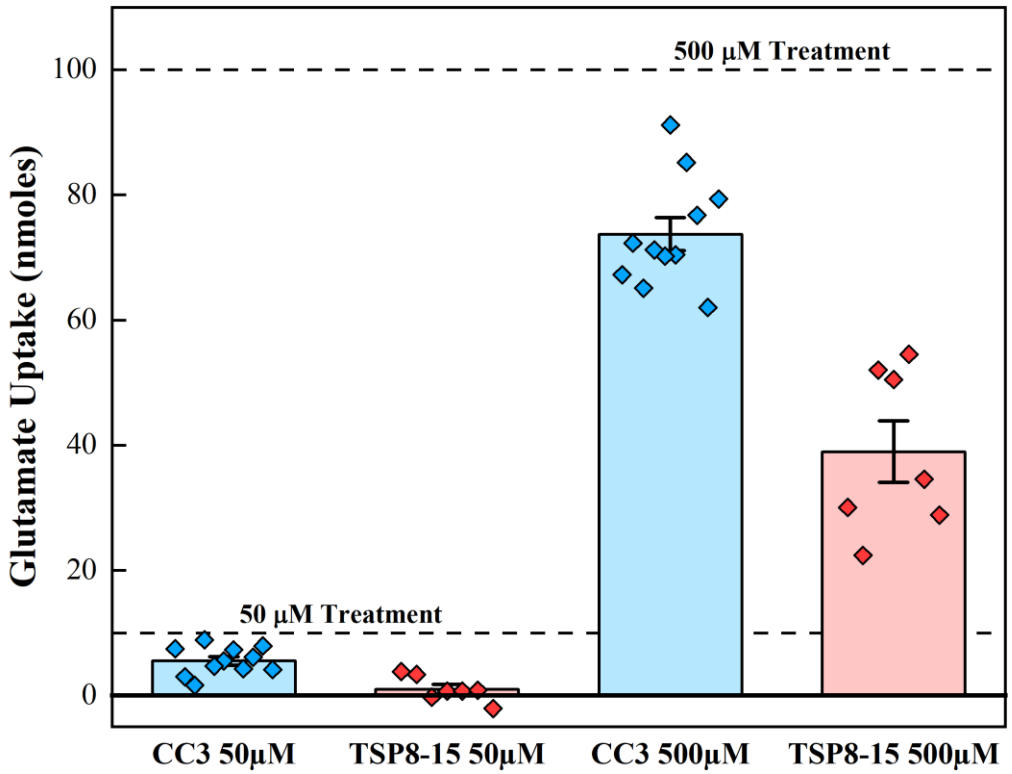

Figure 3.7. Glutamate Uptake by CC3 and TSP8-15 Cells Exposed to 50 and 500 µM Glutamate. Average glutamate uptake was calculated by subtracting the glutamate concentration measured from either TSP8-15 cells or CC3 cells from the treatment with no cells. When exposed to 50 µM glutamate, CC3 cells took up 5.5 ± 0.7 nmoles compared to the TSP8-15 cells which took up 1.0 ± 0.8 nmoles. During the 500 µM treatment, CC3 cells took up 74 ± 3 nmoles while the TSP8-15 cells took up 39 ± 5 nmoles. There was a significant difference in uptake between the two cells types for both 50 µM and 500 µM treatments, with p-values ≤ 0.0006 and 0.0002, respectively. All experiments were performed at 20 µL min^{-1}, 37 °C, and 5% CO2. Data are presented as mean and standard error for all measurements, n = 11 for CC3 and 7 for TSP8-15, p-values resulting from t-tests with unequal variance.

responsible for the seizures experienced by some with TSC, as the diminished uptake leads to increases in extracellular glutamate concentration. Future studies using this system could further evaluate the mechanisms responsible for the decreased glutamate uptake. This platform—allowing for microfluidic treatment of cells directly within the area of analysis—could also be used to investigate other rare and complex diseases, along with their possible treatments.

Conclusions

In this work, a glutamate sensor was developed and characterized within the microfluidic μCA platform and used to monitor the uptake of glutamate by cells in real time. The glutamate sensor was shown to have the response time, linear range, and stability necessary to monitor glutamate in a wide range of biological systems. A proof-of-concept experiment was done with PC12 cells demonstrating the ability of the glutamate sensor detect real-time uptake within the μCA. PC12 cells were shown to uptake significant amounts of glutamate when exposed to excitotoxic concentrations following depolarization and glucose starvation. Control CC3 and diseased TSP8-15 astrocytes were also shown to take up glutamate in response to excitotoxic concentrations. TSP8-15 astrocytes from those with TSC took up less glutamate than the control, leading to increased extracellular glutamate—a possible explanation for the seizures experienced by TSC patients. The application of the electrochemical, microfluidic μCA system could in the future be applied to the real-time study of other cellular mechanisms.

Acknowledgments

This work was supported in part by IARPA grant number 2017-17081500003 and used the resources of the Vanderbilt Microfabrication Core operated by the Vanderbilt Institute for

Integrative Biosystems Research and Education. The authors would like to thank Kazi Tasneem for the modeling of shear stress, M. Diana Neely for providing the astrocytes, and Dusty R. Miller for editorial and graphical support.

Chapter IV

EFFECTS OF ORGANOPHOSPHATE TOXICITY ON ACETYLCHOLINE METABOLISM IN A MODEL BLOOD-BRAIN BARRIER[2]

Introduction

Organophosphates (OPs) are used throughout the world as agricultural pesticides due to their high level of effectiveness and minimal environmental impact.[55] Though it was banned from residential use in 2001, between five and ten million pounds of the OP chlorpyrifos (CPF) are used agriculturally every year in the United States.[56] The states of California and New York have moved to institute complete bans on chlorpyrifos use based on epidemiological studies linking prenatal CPF exposure to neurobehavioral deficits in children.[57,58] At the same time, the consequences of CPF on human health are undergoing further evaluation to fully understand the extent of CPF's negative effects. One potential justification for its continued use is that CPF is excluded from the brain by the blood-brain barrier (BBB), though more research is necessary to provide clear scientific evidence of this. If able to cross the BBB, OPs like CPF may have significant effects on acetylcholine metabolism—resulting in serious health consequences. To this end, an acetylcholine sensor is presented and, together with an *in vitro* organotypic BBB, the effects of CPF on acetylcholine metabolism are investigated.

As pesticides, OP compounds cause neurotoxicity by preventing the breakdown of acetylcholine and, consequently, altering acetylcholine levels in the brain. When neurons are functioning properly, acetylcholine—a neurotransmitter regulating a diverse range of processes—

[2] This chapter contains portions from the published research articles 1. McClain, E. S.; Miller, D. R.; Cliffel, D. E. *J. Electrochem. Soc.* 2019, 166 (16), G178–G181.

is released into the neuronal synapse for signaling before being broken down by acetylcholinesterase and taken back up by presynaptic neurons.[59,60] Across the blood-brain barrier, OPs bind to a serine in the active site of acetylcholinesterase—inhibiting the cleavage of acetylcholine (**Figure 4.1, left**).[32,33] The subsequent increase in acetylcholine concentration leads to the overstimulation of the muscular, endocrine, and central nervous systems and can result in muscular fasciculation, decreasing motor activity, and respiratory depression.[61] OPs can also be quickly metabolized into their oxidized (oxon) forms, known to be more toxic and inhibiting acetylcholinesterase to a greater degree **(Figure 4.1, right**).[62] Due to this effect of OPs on acetylcholinesterase, the inhibition of plasma and red blood cell cholinesterase is sometimes used as a quantification method for characterizing OP exposure.[63] The ability to directly detect and quantify changes in acetylcholine levels may assist in the early detection and treatment of OP poisoning.

The development of enzymatic biosensors for the electrochemical detection of acetylcholine can provide a low-cost but selective method for acetylcholine detection. Other methods of identification, such as colorimetric and chromatographic techniques, provide high sensitivity but with greater time and expense required.[64–66] Electrochemical enzyme sensors have already been developed for other biological analytes, including glucose, lactate, and glutamate.[17,36] Some enzymatic sensors, like the one presented here, can be coupled with microfluidic platforms—such as the microclinical analyzer (μCA). The μCA system provides for increased throughput and enables the automation of the calibration and analysis process with custom flow rates and sampling times.[17] Coupling microfluidic systems with electrochemical sensors can provide new insight into the effects that toxicants like CPF may have on cellular metabolism. These analysis platforms are particularly well-suited to the analysis of eluate from *in vitro* organotypic systems.

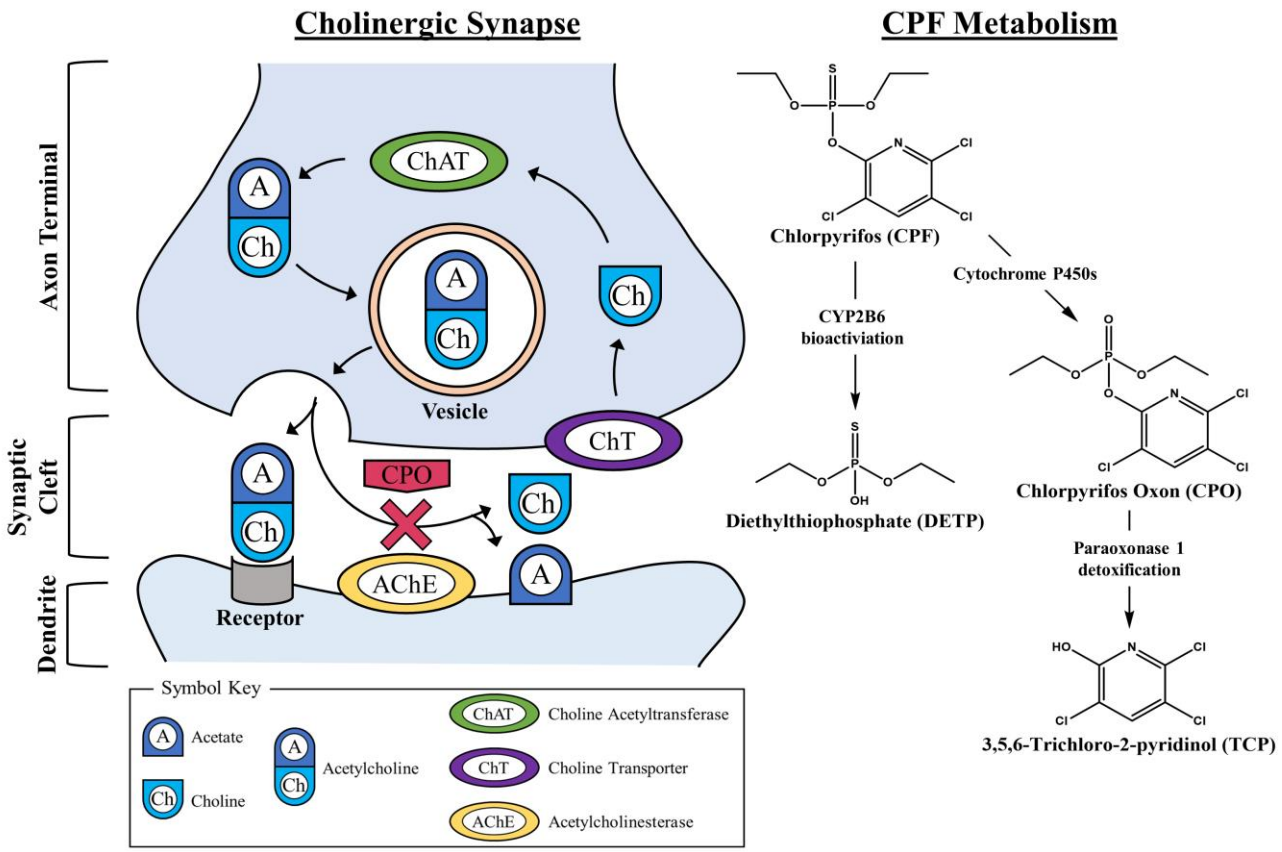

Figure 4.1. Schematic of Acetylcholine and Chlorpyrifos Biochemistry. Left) During typical function, acetylcholine is released from vesicles into the synaptic cleft where it can bind to a receptor. Following signaling, acetylcholinesterase breaks down acetylcholine into choline and acetate, with the choline being taken back up into the cell by a choline transporter and remade into acetylcholine by choline acetyltransferase. In the presence of CPO, however, acetylcholinesterase is inhibited from breaking down acetylcholine. This leads to a buildup of acetylcholine, and eventually, excitotoxicity and possible neurodegeneration. Right) The major metabolic pathway for CPF bioactivation and biodegradation showing associated primary metabolites including CPF, CPO, diethylthiophosphate (DETP), and 3,5,6-trichloro-2-pyridinol (TCP).

Though traditionally toxicological studies have been performed using animal models, organs-on-chips (OoCs) are becoming more common as substitutes for early-phase toxicology. OoCs are organotypic, three-dimensional cultures that grow to develop organ-like qualities.[67] Early work investigating the effects of toxins on BBB permeability was done using transwell assays, which led to the development of three-dimensional models of the BBB.[68–73] Wikswo and colleagues developed a neurovascular unit (NVU), an organotypic model that approximates the human BBB by creating a paracellular barrier comprised of endothelial cells, astrocytes, pericytes, and neurons.[21] This NVU has been shown to be a useful model to assess both acute and chronic toxic exposures.[21,74] The NVU is a dual-chambered design, with a neuronal (2.9 µL) and a vascular (17.5 µL) section, both equipped with independent microfluidic perfusion control. This is essential for simulating environmental exposure, as toxicants can be administered to only the vascular side. The neuronal side can then be analyzed—through electrochemical detection or other analytical methods—for metabolic changes and the infiltration of toxicants that breach the engineered BBB.

In this work, an enzymatic acetylcholine sensor was developed and used within the µCA for the analysis of eluate from the NVU. Detection parameters of the acetylcholine sensor were established both with and without CPF to confirm that the sensor was not sensitive to CPF. The sensor was shown to be useful for the biorecognition of chlorpyrifos oxon (CPO)—an active metabolite of CPF—through inhibitory mechanisms, and the reusability of these sensors was demonstrated through treatment with 2-pyridine aldoxime methyl chloride (2-PAM). The sensor was then used to evaluate the effects of CPF on the acetylcholine concentration of eluate from an NVU treated with 10 µM CPF. Following electrochemical and metabolomic analysis, the effects of PDMS on the concentration of CPF in solution was studied.

Experimental

Materials

Acetylcholine chloride, acetylcholinesterase from *Electrophorus electricus*, choline oxidase from *Alcaligenes*, bovine serum albumin, glutaraldehyde, chlorpyrifos, chlorpyrifos oxon, and 2-pyridine aldoxime methyl chloride were purchased from MilliporeSigma (Burlington, MA). Phosphate buffer solution (pH 7) and potassium chloride were purchased from Fisher Scientific (Waltham, MA). SPEs were designed in house and purchased from Pine Research (Durham, NC). Tygon tubing was purchased from Cole Parmer (Vernon Hills, IL). PDMS was purchased from the Vanderbilt Institute of Integrative Biosystems Research and Education (VIIBRE, Nashville, TN). The rotary planar peristaltic micropump, valves, microclinical analyzer, microcontrollers, and computer software were designed by and purchased from the Vanderbilt Microfabrication Core/VIIBRE. The CHI 1440 potentiostat was purchased from CH Instruments (Austin, TX).

Acetylcholine Sensor Fabrication

An SPE was enzymatically modified to be sensitive to acetylcholine. The largest band electrode on the electrode array was used as a Ag/AgCl quasi-reference, while the three disk electrodes were enzymatically modified using acetylcholinesterase from *Electrophorus electricus* (137 Units/mg), and choline oxidase from *Alcaligenes* (15 Units/mg). Each enzyme was dissolved separately to a concentration of 10 mg/mL in phosphate buffer solution (2 mM buffer solution, pH 7) with bovine serum albumin (800 mg/mL) and stored until use at -18°C. When required, these enzymes were combined equally (v/v), mixed with glutaraldehyde (0.5% wt/v, Sigma), vortexed (~5 sec), and 1 µL was drop cast onto each working electrode. These SPEs were then air dried for an hour before either use or storage (in low light conditions to reduce oxidation of silver). To

incorporate these sensors into the μCA, they were sealed within the housing and attached to a microformulator—a microfluidic pump and valve system providing for automated sensor calibration and sample analysis.[17]

Characterization of Acetylcholine Sensor

The limits of detection (LOD) and quantitation (LOQ), linear range, V_{max}, and K_m for the acetylcholine sensor were determined using the μCA as they were for other enzyme sensors.[12,17] Calibrations were performed by monitoring the current generated by calibrants (1 μM to 1 mM acetylcholine, with and without 50 μM CPF) in buffer. Buffer for all experiments was made from a 50 mM potassium monobasic-sodium buffer (pH 7) and diluted in water with KCl to produce a 2 mM phosphate, 120 mM KCl, pH 7 buffer solution. Current was monitored using a CHI 1440 potentiostat held at 0.6 V vs. Ag/AgCl. Calibrants were sampled at 100 μL min^{-1} using the microformulator. Linear regressions were performed on the linear ranges of the calibration data. The resulting slopes provided the sensitivity of the SPE with and without 50 μM CPF present. The limits of detection were calculated according to *Equation 1*, where S_E is the error of the y-intercept, and *m* is the slope of the calibration. The equation used for calculating the limit of quantitation is similar, except that the error was multiplied by ten instead of three. Because the enzyme saturation followed Michaelis-Menten kinetics, a hyperbolic function could be fit to the data to determine V_{max} and K_m. The resulting equation of the hyperbola provided coefficients corresponding to the values for V_{max} and K_m. All p-values calculated were found by performing t-tests assuming unequal variance. Stability of the sensor was tested by exposing the sensor to acetylcholine calibrants (20, 40, 60, 80, and 100 μM) every four hours for 68 hours and comparing the sensitivities of each calibration.

$$LOD = \frac{3S_E}{m} \quad (1)$$

Sensor Inhibition Using CPF and CPO.

To test the effect of CPF and CPO on acetylcholine detection, the sensor response to acetylcholine was measured both before and after exposure to each compound. For initial acetylcholine measurements, the sensor was first allowed to reach steady-state current in buffer (10 min.), before being treated with acetylcholine (50 µM, 5 measurements, 2 minutes each). After each acetylcholine measurement, buffer was run over the sensor (2 minutes) to return to baseline (100 µL min^{-1}). The sensor was then exposed to an OP solution (0.5 - 50 µM CPF or CPO, 100 - 500 µL min^{-1}, 10 - 30 minutes) to determine how flow rate, OP concentration, and exposure time effected sensor inhibition. Each inhibition was followed by a ten-minute buffer wash period before acetylcholine measurements were taken again. Inhibition percentage was calculated using *Equation 2*, where *I%* is the inhibition percentage, i_0 is the steady-state current generated by acetylcholine before OP exposure, and i_1 is the steady-state current generated by acetylcholine after OP exposure. The current values used for i_0 and i_1 are averages of the currents generated by five acetylcholine measurements before and after OP exposure.

$$I\% = 100 \times \left(\frac{i_0 - i_1}{i_0}\right) \quad (2)$$

Sensor Regeneration

Sensor regeneration was investigated by using 2-PAM, an antidote for OP poisoning, to counteract the enzymatic inhibition by CPO. After reaching steady state, the current generated by acetylcholine (50 µM) was measured five separate times alternating with buffer to provide a baseline. The sensor was then exposed to CPO (5 µM, 100 µL min^{-1}, 30 minutes) and the response

to acetylcholine was measured as before. The inhibition percentage was again calculated as in *Equation 2*. Sensors were regenerated by 2-PAM (500 µM, in buffer, 30 minutes), followed by another set of acetylcholine measurements. Regeneration percentage was determined using *Equation 3*, where *R%* is the regeneration percentage, i_2 is the steady-state current generated by acetylcholine after 2-PAM treatment, and $i_{0,}$ as before, is the steady-state current generated by acetylcholine before OP exposure.

$$R\% = 100 \times \left(\frac{i_2}{i_0}\right) \tag{3}$$

Analysis of Acetylcholine in NVU Eluate

The µCA electrochemical detection platform was used to determine the acetylcholine levels in NVU eluate samples both with and without CPF treatment. The acetylcholine sensor, with its three enzymatically modified electrodes, was loaded into the µCA housing and the current was monitored by all three to provide technical replicates. Using the microformulator, calibrants were sampled at a flow rate of 100 µL min^{-1} (six calibrants from 0 to 114 µM). After calibration, NVU eluate was sampled with buffer in between each sample to establish a baseline. The sensor was recalibrated before and after each NVU sample set to check for sensor response degradation/inhibition. The acetylcholine concentration in the sample was determined using the current generated by the samples and performing linear regressions on the calibration data. All p-values calculated were determined through a t-test assuming unequal variance.

Effects of PDMS on Chlorpyrifos Concentration

To determine the extent to which CPF absorbs into PDMS, a floating disk experiment was conducted.[75] First, 3 mm thick medical grade PDMS (the same as that used in the NVU fabrication) was cut with a biopsy punch (diameter = 6 mm) to form disks. Using a 20 mM stock solution of CPF made in DMSO, 25, 50 75, and 100 µM CPF solutions were made in 10 mM SDS to aid solubility. Then, each disk was submerged in 2 mL of 100 µM CPF solution inside of a 4 mL glass vial and the absorption of this solution as well as that of calibrants (25, 50, 75, and 100 µM CPF) was measured every hour at 290 nm in a quartz cuvette. From these data, the concentration of CPF still in solution was calculated.

Results and Discussion

The effects of OPs on the human brain are unclear, specifically in regards to the interaction between OPs and the BBB. The electrochemical analysis of acetylcholine in eluate from *in vitro* organotypic models exposed to OPs may provide insight into the effects of these compounds on cellular function and BBB integrity. Here, an acetylcholine sensor is developed and characterized in the presence of CPF and CPO, and the effects of 2-PAM on sensor reusability are presented. The NVU, a model BBB, is then exposed to 10 µM CPF and the eluate from each side of the device is analyzed through amperometric electrochemistry. Following this, the effects of PDMS on the concentration of CPF in solution is explored.

The need to analyze systems directly affected by CPF requires the development of an acetylcholine sensor that can function in the presence of CPF. Consequently, it is essential to understand how CPF effects the response of the sensor. In the past, acetylcholinesterase has been used in colorimetric and nanoparticle-based assays to detect CPF, as the competitive inhibition of

acetylcholinesterase by CPF results in the inactivation of the enzyme.[76,77] One method of exploring the effects of CPF on enzymatic activity is through kinetics measurements like V_{max} and K_m—measurements of maximum enzyme rate and concentration of substrate at half V_{max}, respectively. Occupation of acetylcholinesterase active sites by CPF will result in lower V_{max} and K_m values. Here, both the V_{max} and K_m of the sensor are nearly identical for acetylcholine detection with and without 50 µM CPF. V_{max} values of 4.3 ± 0.2 and 4.1 ± 0.3 pmol s^{-1}, for acetylcholine and CPF solutions respectively, and K_m values of 285 ± 15 and 288 ± 15 µM result in p-values ≤ 0.64 for V_{max} and 0.87 for K_m. This signifies no significant difference in enzyme kinetics with the addition of CPF to solution (**Figure 4.2, top**). These results indicate that the enzymatic active sites are not being populated by CPF but are instead available to cleave acetylcholine. Additionally, the high K_m values compared to the physiological concentration of acetylcholine—single digit to tens of micromolar—indicate that the presented sensor is well suited to the sensitive detection of acetylcholine in eluate from biological systems.[78]

These conclusions are further supported by the sensor response metrics. In the absence of CPF, the acetylcholine sensor's linear range was 1 to 150 µM, with low detection and quantitation limits (0.2 ± 0.1 µM and 0.7 ± 0.1 µM respectively) and a high sensitivity (1.0 ± 0.1 nA μM^{-1} mm^{-2}, **Figure 4.2, bottom**). The sensor also demonstrated good operational stability, retaining 92 ± 7% of its response over 68 hours of continuous use. The current magnitude decreased throughout the experiment, decreasing more substantially after 48 hours of use (**Figure 4.3**). Including 50 µM CPF in the calibrant solutions had minimal effects on detection limits, with comparably low LOD and LOQ values (0.8 ± 0.2 µM and 2.5 ± 0.6 µM respectively, p-values ≤ 0.09 compared to no CPF), along with a sensitivity and linear range equivalent to the CPF-free solutions (1.0 ± 0.1 nA μM^{-1} mm^{-2}, p-value ≤ 0.93, 3 to 150 µM). Over the course of this experiment, the acetylcholine

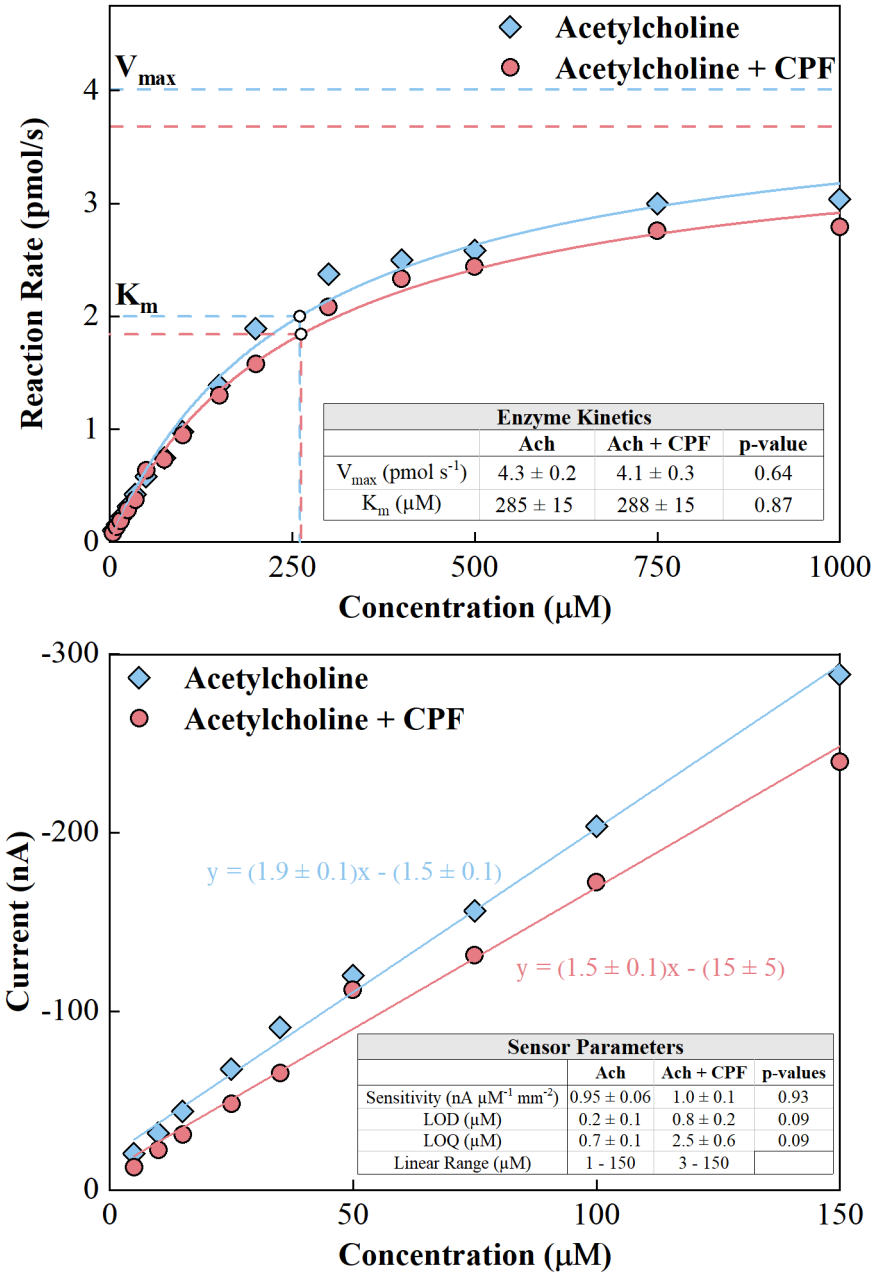

Figure 4.2. Enzyme Kinetics and Sensor Parameters for the Acetylcholine Sensor. Calibrants were sampled through a microformulator (1 µM to 1 mM acetylcholine, 2 minutes) with buffer in between (2 minutes) at 100 µL min^{-1}, 25 °C. Top) Calibration showing enzyme saturation for each solution set. Table: Enzyme kinetics, V_{max} and K_m, for each solution set. Bottom) Scatterplot of the linear range for each solution set. Table: Detection parameters of the sensor including LOD, LOQ, linear range, and sensitivity with and without CPF. For both enzyme kinetics and sensor parameters, significance testing (t-test assuming unequal variance, n = 3) was performed across solution sets.

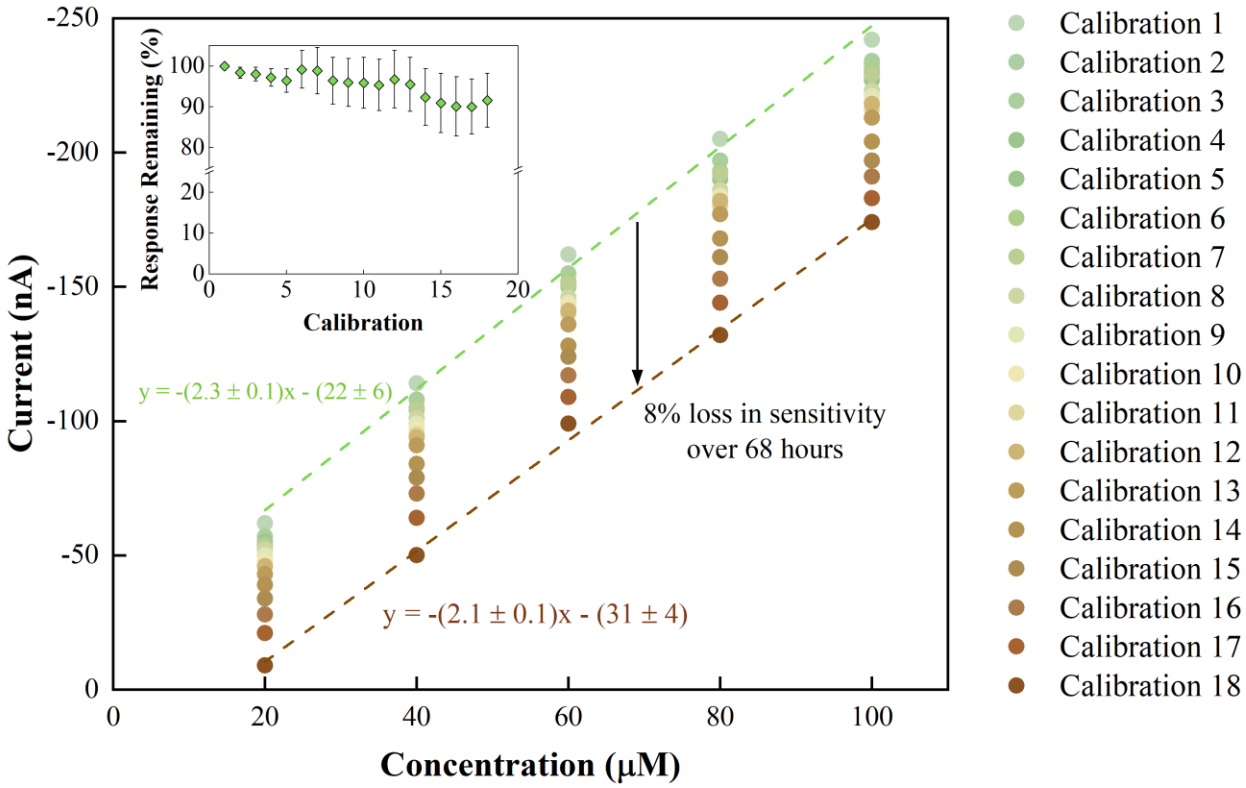

Figure 4.3. Stability of Acetylcholine Sensor Over 68 Hours. The response of the acetylcholine sensor to a set of 5 acetylcholine calibrants was tested every 4 hours for 68 hours. The magnitude of current generated decreased with each calibration, with decreases becoming more substantial in the later calibrations. Nevertheless, the sensor retained 92 ± 7% of its original sensitivity upon conclusion of the experiment. Inset: The sensitivity of each calibration was calculated and reported as a percentage of the first calibration sensitivity.

sensor was treated with 50 µM CPF—175 times higher than the Drinking Water Equivalence Level—for well over 30 minutes, with negligible effects on sensor function.[79] As a result, this sensor could be useful in analyzing changes in acetylcholine concentration in systems containing high levels of CPF.

To further characterize sensor performance, the microformulator pump and valve system was used to adjust OP exposure times and flow rates to establish the effects of these variables on sensor function. At every flow rate and exposure time tested, CPF did not inhibit sensor function, with any losses being comparable to the signal decrease seen in the controls. Conversely, CPO-induced enzyme inhibition consistently followed Michaelis-Menten kinetics (**Figure 4.4, inset**), enabling the creation of linear calibration curves that allow for CPO quantification (**Figure 4.4**). Using 10% as a minimum for sensor inhibition, a flow rate of 100 µL min^{-1} and an exposure time of 10 minutes resulted in a calculated detectable concentration of 3 µM CPO. This minimum inhibition standard of 10% was chosen as it was well above typical signal losses due to time-dependent decreases in enzyme activity. Even with a 10% inhibition minimum, the detection limit was as low as 193 nM when exposure time was increased to 30 minutes. Similarly, increasing the flow rate during CPO exposure from 100 to 500 µL min^{-1} resulted in 10% sensor inhibition concentration of 324 nM CPO. While other studies have described sensors utilizing acetylcholinesterase for OP detection, the microformulator in conjunction with the µCA allows for variation in flow rates and exposure times, enabling increased experimental flexibility and resulting in the biorecognition of CPO by the acetylcholine sensor at concentrations as low as 193 nM.[80–83]

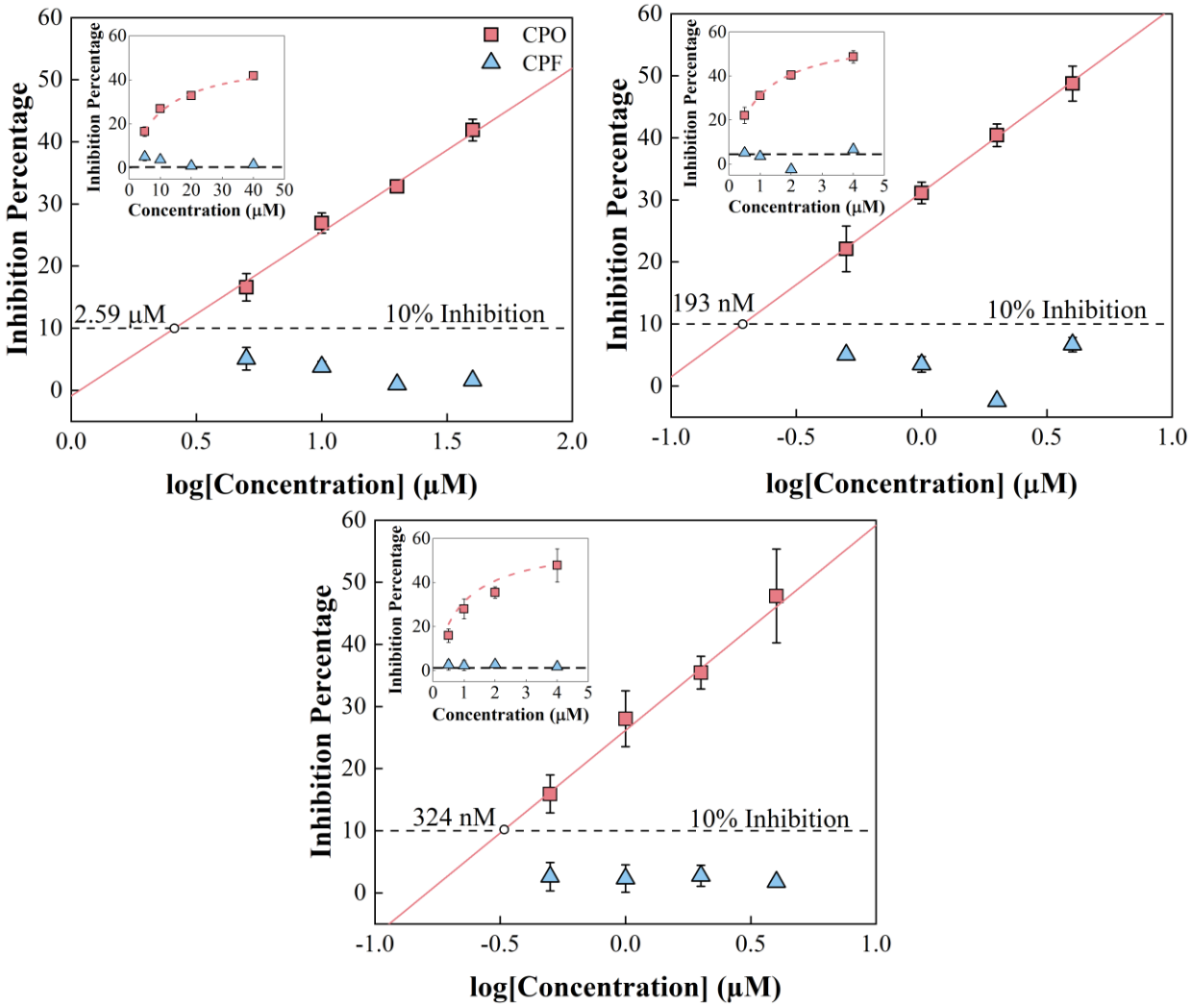

Figure 4.4. Acetylcholine Sensor Response to CPF and CPO. Top, left) 100 µL min^{-1} for 10 minutes Top, right) 100 µL min^{-1} for 30 minutes and Bottom) 500 µL min^{-1} for 10 minutes Insets: Inhibition percentage vs. [CPO or CPF] showing a logarithmic increase in inhibition with increasing CPO concentration, and no substantial inhibition from CPF compared to controls (dashed line). Graphs: Inhibition percentage vs. log[CPO or CPF] resulting in a linear relationship for CPO inhibition as expected for Michaelis-Menten kinetics. The 10% inhibition concentration decreased with increasing flow rate and treatment time, reaching as low as 193 nM at 100 µL min^{-1} for 30 minutes. Experiments were performed in the µCA with acetylcholine (50 µM, 2 minutes, 100 µL min^{-1}) and CPO or CPF (0.5 – 40 µM) with treatments of 10 to 30 minutes at flow rates of 100 to 500 µL min^{-1}. Data represented as mean and SE (n = 3).

The regeneration of a CPO-inhibited acetylcholine sensor by 2-PAM introduces the opportunity for rapid quantification of CPO and other highly toxic OPs.[84] At the sensor surface, acetylcholinesterase inhibition occurs when OP compounds bind to an active site serine, preventing the enzyme from cleaving acetylcholine. This bond between the OP and acetylcholinesterase is reversible for only a short period of time before an aging process occurs that renders it irreversible.[85] To demonstrate this reversibility, the sensor underwent regenerative treatments using 2-PAM, a treatment for OP poisoning, to reactivate the acetylcholinesterase used in sensor creation.[86,87] During these experiments, the microformulator was used to first inhibit the sensor using CPO (5 µM, 30 min.) before regenerating with 2-PAM (500 µM, 30 min.). The response of the sensor to 50 µM acetylcholine was measured after both inhibition and regeneration. Following CPO exposure, the signal decreased to an average of 26 ± 1% of the original signal. Subsequent treatment with 2-PAM resulted in regaining 78 ± 4% of the pre-inhibition signal. Though the regeneration percentage remained consistent, by the fifth regeneration attempt only 29 ± 7% of the original signal remained (**Figure 4.5**). Even so, the ability to regenerate the sensor after OP inhibition can substantially increase sensor reusability, decreasing both the time and cost associated with using this sensor as a quantification method.

As the developed acetylcholine sensor properly functions even in the presence of high concentrations of CPF, it can be used to monitor acetylcholine in the eluate of a CPF-treated NVU. The NVU incorporates all four cell types necessary to model BBB function within a three-dimensional, dual-chambered device.[21,74] The NVU's vascular chamber was seeded with a human endothelial cell line and grown to confluency, before human astrocytes, pericytes, and primary rat neurons were added to the neuronal chamber. Human cell lines were chosen to create the BBB for both ease of use compared to primary human cells and as they more closely replicate the human

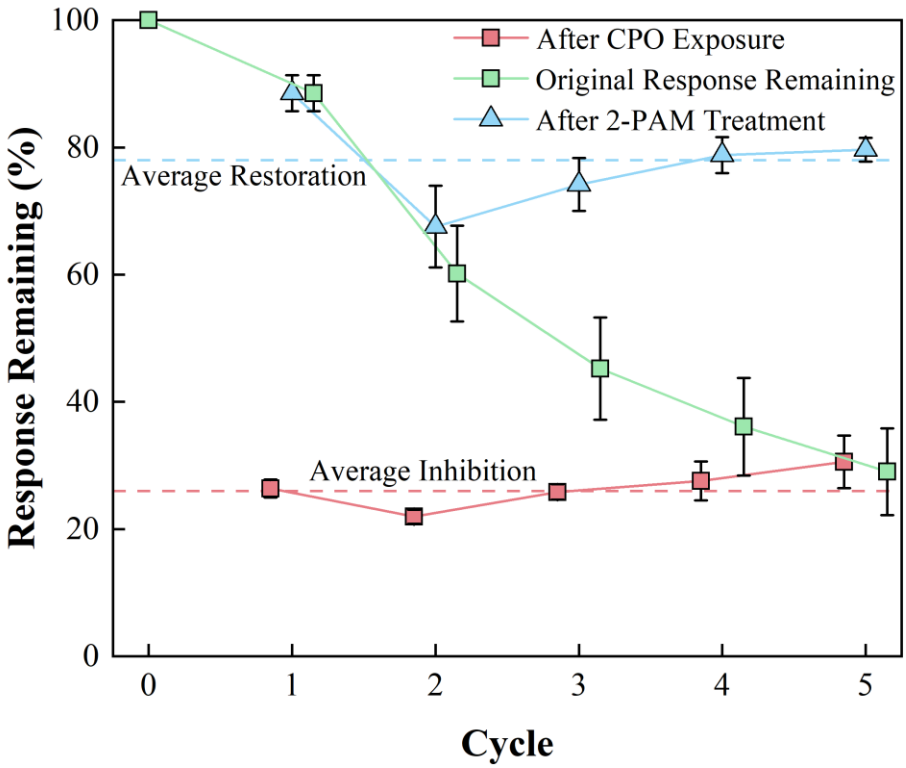

Figure 4.5. Inhibition and Regeneration of an Acetylcholine Sensor. The acetylcholine sensor was inhibited by CPO and regenerated five times to assess sensor consistency in inhibition and regeneration magnitude. After inhibition, an average of 26 ± 1% of the previous signal remained (red dashed line). Following regeneration, an average of 78 ± 4% of the lost signal was regained (blue dashed line). This repetitive regeneration resulted in 29 ± 7% of the original signal remaining after the fifth cycle.

brain environment—as rodents have been shown to have increased BBB permeability compared to humans.[88,89] In selecting neurons, primary neuronal cultures were chosen to ensure that their differentiation is representative of mammalian neurons. Specifically, cholinergic neurons were desired to accurately represent susceptibility to organophosphates. The primary cultures used here were 90% neurons and 10% microglia and determined to be 10% positive for choline acetyltransferase—indicating active cholinergic signaling. With all four cell types in the device, both chambers were equipped with microfluidic perfusion control in preparation for simulating acute environmental exposure to CPF.

To test the effects of an acute dose of CPF on acetylcholine metabolism within the NVU, the vascular sides of the NVUs were dosed with 10 µM CPF for 24 hours and the eluate was periodically collected and analyzed electrochemically. In this work, four NVUs were perfused in parallel, with three experimental devices and one control device. When exposed to 10 µM CPF, the vascular eluate showed a significant increase in acetylcholine concentration (26 ± 3 µM, p-value ≤ 0.006, **Figure 4.6, top**) compared to the control after two hours, which remained elevated through the 24-hour time point (27 ± 3 µM). This acetylcholine buildup is a hallmark of organophosphate poisoning and can interfere with the muscarinic, nicotinic, and central nervous systems—triggering the failure of essential autonomic processes such as respiration and circulation.

In this same experiment, acetylcholine metabolism was also significantly dysregulated within the NVU neuronal chambers, despite not being treated directly with CPF. Across the BBB, acetylcholine levels were again significantly elevated compared to the control device after two hours (95 ± 10 µM, p-value ≤ 0.0006, **Figure 4.6, bottom**) and remained similarly elevated for

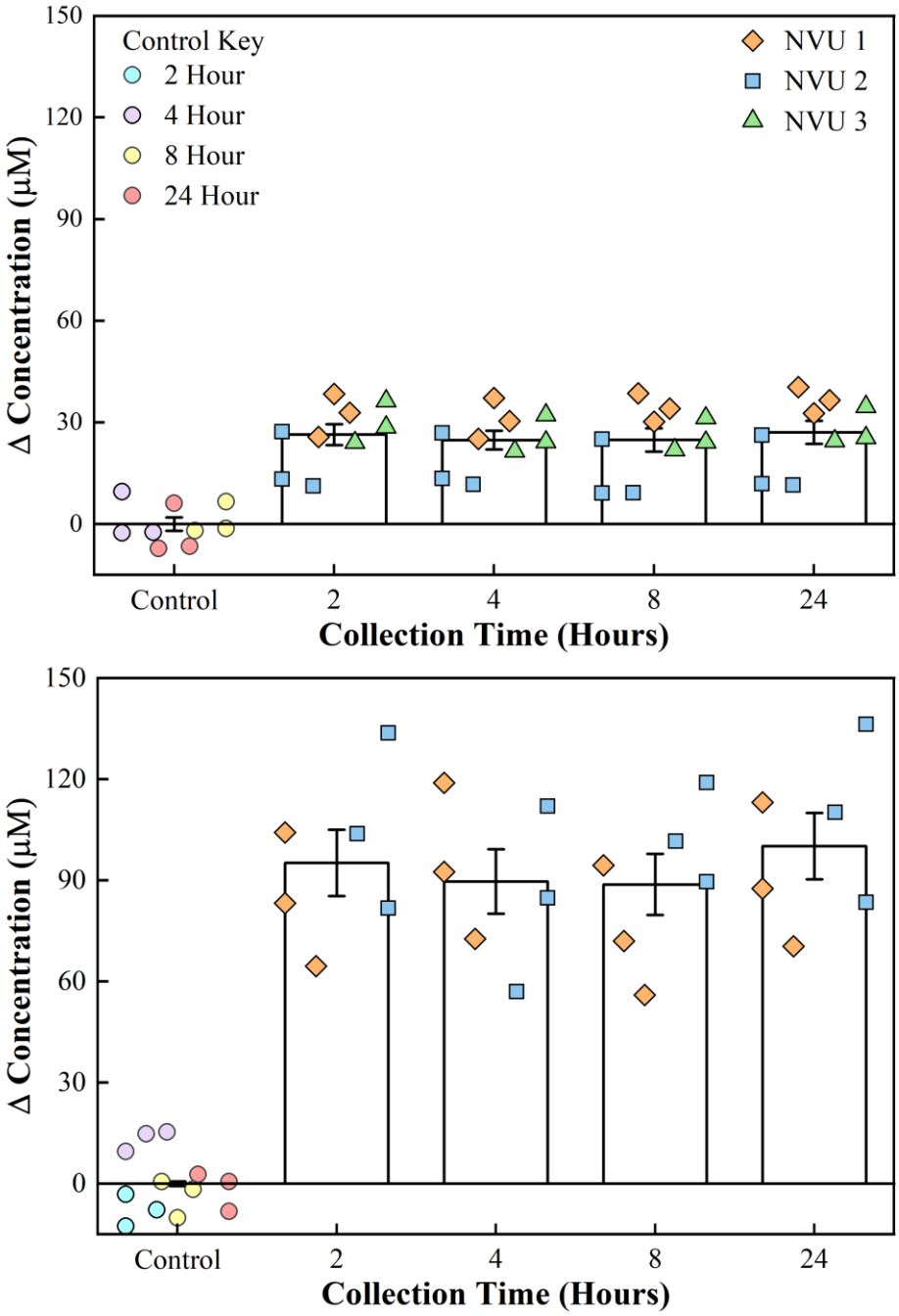

Figure 4.6. Electrochemical Analysis of Acetylcholine Concentration in NVU Eluate. Top) Bar graph indicating the change in acetylcholine concentration from control (DMSO) in vascular-side eluate showing elevated acetylcholine levels (26 ± 3 µM) after two hours of CPF treatment (10 µM CPF, p-value ≤ 0.003). Bottom) Bar graph indicating change in acetylcholine concentration in neuronal-side eluate showing elevated acetylcholine (95 ± 10 µM) two hours after CPF was administered to the vascular side (p-value ≤ 0.04 compared to control). Data are represented as the means and standard errors, symbols represent technical replicates, n = 6 to 9 for samples and n = 9 to 12 for controls. Control samples were collected over 24 hours and their respective collection time is indicated in the control key.

the duration of the 24-hour experiment (100 ± 10 μM). The cholinergic neurons on the neuronal side of the NVU are thought to be primarily responsible for acetylcholine production, perhaps accounting for the greater change in acetylcholine levels compared to the vascular side. This increase also suggests that either CPF, its toxic metabolites, or other soluble factors were able to cross the BBB and interact directly with the neurons.

In addition to the electrochemical analysis of NVU eluate, mass spectrometry was utilized to directly investigate the potential crossover and metabolism of 10 μM CPF on both sides of the BBB. Targeted MS did not detect CPF or CPO in either vascular (**Figure 4.7*, top plots***) or neuronal eluate samples (**Figure 4.7*, bottom plots***). Only one metabolite, TCP, was detected above the limit of quantitation and only on the vascular side. TCP was detected at ~0.05 μM on the vascular side after 2 hours of treatment, with this concentration increasing to ~0.19 μM after 24 hours of CPF treatment. Neither CPF nor any of its metabolites, toxic or otherwise, were detected with mass spectrometry of the neuronal eluate. These data, along with other studies showing TCP to be the primary urinary metabolite of CPF in both humans and rodents, suggest that the biodegradation and/or removal of TCP is the rate-limiting step for CPF detoxification.[90,91]

While the metabolomics agree with what is typically seen in CPF degradation, the substantial decrease in metabolite concentrations compared to what was administered raises questions as to why more CPF or its metabolites were not detected. One possibility is that the PDMS used to fabricate the device absorbed most of the CPF before it could be metabolized. PDMS has been demonstrated to absorb hydrophobic small molecules—an issue as many microfluidic devices, including the NVU, are made of PDMS.[92] To test PDMS absorption of CPF, a floating disk experiment was conducted and revealed that after 2 hours, 14 ± 1 % of the CPF in solution was lost to the PDMS.[75] After 24 hours, this number increased to 67 ± 2 % (**Figure 4.8**).

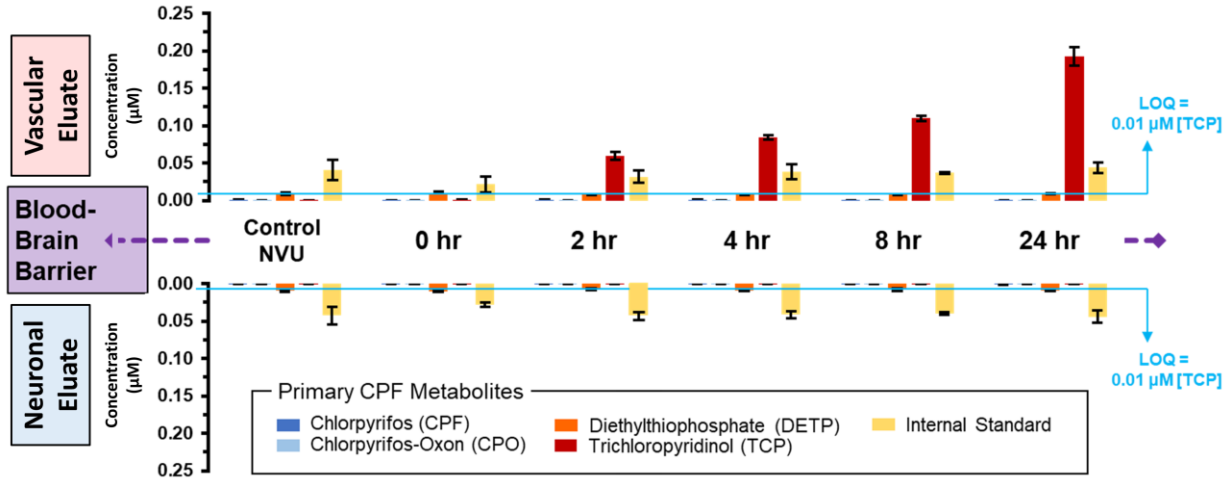

Figure 4.7. Distribution of CPF and its Primary Metabolites Within the NVU. Using targeted mass spectrometry, CPF and its three primary metabolites were quantified in both the vascular (upper plots) and neuronal (lower plots) eluate media samples. These samples were obtained at lengthening durations of exposure to 10 µM CPF within the NVU. Eluate collected from the vascular side showed no CPF above the LOQ. From 2 hours on, only the inactive metabolite TCP was detected. Eluate collected from the neuronal chamber showed no CPF or any metabolites above the LOQ throughout the duration of the experiment.

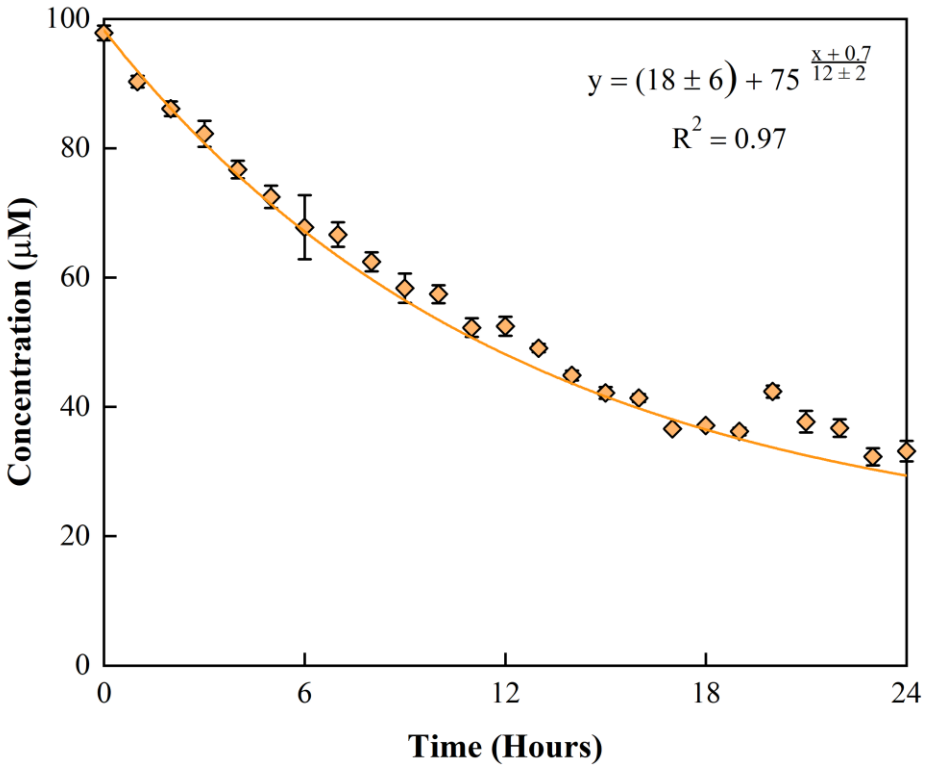

Figure 4.8. PDMS Absorption of CPF. PDMS disks (3 mm x 6 mm) were submerged in 100 µM CPF with 10 mM SDS (2 mL) for 24 hours. CPF remaining in solution was monitored every hour by measuring the absorbance at 290 nm. To determine the concentration of CPF remaining, a calibration curve was made with known concentrations of CPF (25 to 100 µM) and the unknown concentration was determined using the equation of the best fit line. After 24 hours, only 33 ± 2% of the added CPF was detected. All experiments were performed in ambient conditions. Data shown as average and standard error, n = 3.

This absorption of CPF is substantial and must be considered when designing and interpreting experiments. However, considering the flow rate and volume of the NVU, CPF being perfused through the device was in contact with the NVU for less than two hours. PDMS absorption of CPF therefore only accounts for a small percentage of the disappearance in this case, and further work must be done to determine the whereabouts of the remaining CPF and metabolites.

Conclusions

OP exposure, common among those working with agricultural pesticides, directly and irreparably alters neural function if not properly treated. An enzyme sensor was developed and characterized following exposure to the OPs CPF and CPO, and this sensor was used to study the effects of CPF on acetylcholine metabolism within the NVU. The sensor was first shown to have similar response characteristics both with and without CPF, and as such could be used to accurately quantify acetylcholine in the presence of high quantities of CPF (<50 μM). The ability to quantify CPO through inhibition and regenerate the sensor with 2-PAM, allowing for multiple uses, was also shown.

The sensor was then applied to the analysis of eluate from an NVU exposed to 10 μM CPF over a period of 24 hours. Elevated concentrations of acetylcholine were detected on both the vascular and neuronal sides of the device—indicating substantial interaction between CPF or its metabolites, and the cells inside the device. Mass spectrometry of the eluate suggested that, while some of the CPF was metabolized down to TCP, the large majority of the 10 μM CPF was unaccounted for. Further exploration into the effects of PDMS on the CPF concentration in solution indicated that absorption of CPF into the NVU's PDMS may be one possible explanation for the disappearance of some CPF. Regardless, the exposure of NVUs to 10 μM CPF caused

significant disturbance of acetylcholine metabolism on both sides of the BBB, providing chemical evidence of the substantial disruption induced by this widely used agricultural pesticide. These results support previous studies suggesting that organophosphates have significant neurological effects and strengthen the call to better understand the impact of organophosphates on human health and disease. Future work may couple organotypic devices with electrochemical analysis systems to create in-line platforms capable of the real-time detection of multiple analytes at a higher temporal resolution than previously attained. The application of this platform to toxicological testing could be used to further evaluate not only the biological effects of toxicants, but novel therapeutics as well.

Acknowledgments

This work was supported in part by IARPA grant number 2017-17081500003 and used the resources of the Vanderbilt Microfabrication Core operated by the Vanderbilt Institute for Integrative Biosystems Research and Education as well as resources of the Center for Innovative Technology at Vanderbilt University. The authors would like to thank Jacquelyn A. Brown for performing NVU experiments, James N. Dodds and Andrzej Balinski for performing mass spectrometry analysis and interpretation, Jody C. May for mass spectrometry interpretation and graphical support, and Dusty R. Miller for editorial support.

Chapter V

DEVELOPMENT OF A BIOSENSOR FOR THE SIMULATENEOUS DETECTION OF MULTIPLE NEUROTRANSMITTERS

Introduction

Neurotransmitters comprise a group of over 100 signaling molecules involved in a variety of biological functions, encompassing both physical and psychological processes in humans. There are many different categories of neurotransmitters, from amino acids and peptides to monoamines and catecholamines. Depending on their binding location, the function of these neurotransmitters can be excitatory or inhibitory—with both types being essential for proper modulation of synaptic transmission.[1] Excitatory neurotransmitters, like glutamate and dopamine, increase the likelihood of neuronal signaling and are responsible for processes ranging from learning and memory to motor control and emotional regulation.[2,3] In contrast, inhibitory neurotransmitters decrease the probability of synaptic transmission. This group of neurotransmitters includes GABA and adenosine, the latter of which has been found to promote sleep.[93] In addition to these two classifications, some neurotransmitters—like acetylcholine—can also serve as neuromodulators within the brain. Neuromodulators can alter the state of whole groups of neurons at the same time, modifying their response to subsequent stimuli.[6] These varied functions make the ability to detect and quantify neurotransmitters integral to understanding the mechanisms behind many biological processes.

The development of biosensors that can monitor real-time, dynamic changes in multiple neurotransmitters may prove beneficial to understanding neurological disorders and their

treatments. For example, the dysregulation of dopamine and acetylcholine equilibrium is known to be in part responsible for the decreasing motor function present in the progression of Parkinson's Disease.[7] The quantification of neurotransmitters is made challenging due to their quick clearance from the extracellular space, as well as the low concentrations that are generally present.[8,9] The most widely used techniques for detection are microdialysis and fast-scan cyclic voltammetry (FSCV). In microdialysis, analyte present in the brain is perfused through a semi-permeable probe and collected for analysis—generally with high performance liquid chromatography and mass spectrometry.[10] Though sensitive, the temporal resolution of microdialysis can be on the order of minutes. FSCV has a high temporal resolution but is challenged by the presence of many chemical species with similar oxidation potentials, while some neurotransmitters are either not electrochemically active or require high potentials.[11] To measure these species, enzyme-based electrochemical sensors have been developed that provide more sensitive and specific detection.

The development and application of enzymatic biosensors to the study of neurotransmission can provide a low cost but selective method for monitoring multiple neurotransmitters of interest. To this end, enzymatic sensors for the detection of glutamate, acetylcholine, adenosine, and dopamine have previously been demonstrated.[12–15] One of the main drawbacks to enzymatic detection is the generally lower stability these sensors have relative to other detection methods. Some biosensors, like the one presented here, can be used within microfluidic systems—allowing for frequent calibration while also simplifying sample analysis and increasing throughput.[17] Additionally, the use of an SPE with eight working electrodes provides the ability to analyze multiple neurotransmitters simultaneously with replicates if desired. This system can then be used to study the complex interactions between neurotransmitters.

The pesticide chlorpyrifos (CPF) is mainly known for its irreversible inhibition of acetylcholinesterase, with the subsequent buildup in acetylcholine thought to be a factor in the development of neurological disorders following CPF exposure.[62] Some studies, however, have shown that CPF may also dysregulate glutamatergic neurotransmission resulting in an increase in released glutamate.[94,95] An excess of extracellular glutamate triggers excitotoxicity, a process that has been associated with a variety of neurodegenerative diseases—such as Alzheimer's disease.[96] During typical neurotransmission, glutamate released into the neuronal synapse is taken back up by the surrounding glial cells, mainly astrocytes and pericytes, where it is converted into glutamine and transported back into the presynaptic neurons.[97] The dysregulation of this glutamate uptake mechanism could be responsible for the excitotoxic effects seen following neuronal exposure to CPF.

In this work, the development of a sensor for the simultaneous detection of multiple neurotransmitters—glutamate, acetylcholine, adenosine, and dopamine—on the 8-channel electrode (**Figure 5.1**) is presented. Both the adenosine and dopamine enzyme sensors were modified from previous works to function in the μCA system. Additionally, the enzyme ratio for the adenosine sensor was optimized for sensitivity and detection limits. The ability of an m-phenylenediamine (mPD) layer to block interference from ascorbic acid and dopamine was investigated, and the concentration and deposition time was optimized. The detection parameters of each enzyme sensor were determined, along with the stability of each neurotransmitter sensor over time. The capability to detect all four neurotransmitters simultaneously was demonstrated, as well as the ability to adjust the response of the enzyme sensors due to dopamine interference. Lastly, the sensor was used to investigate the effects of CPF and DL-threo-β-benzyloxyaspartic acid on glutamate uptake in human induced pluripotent stem cell-derived astrocytes.

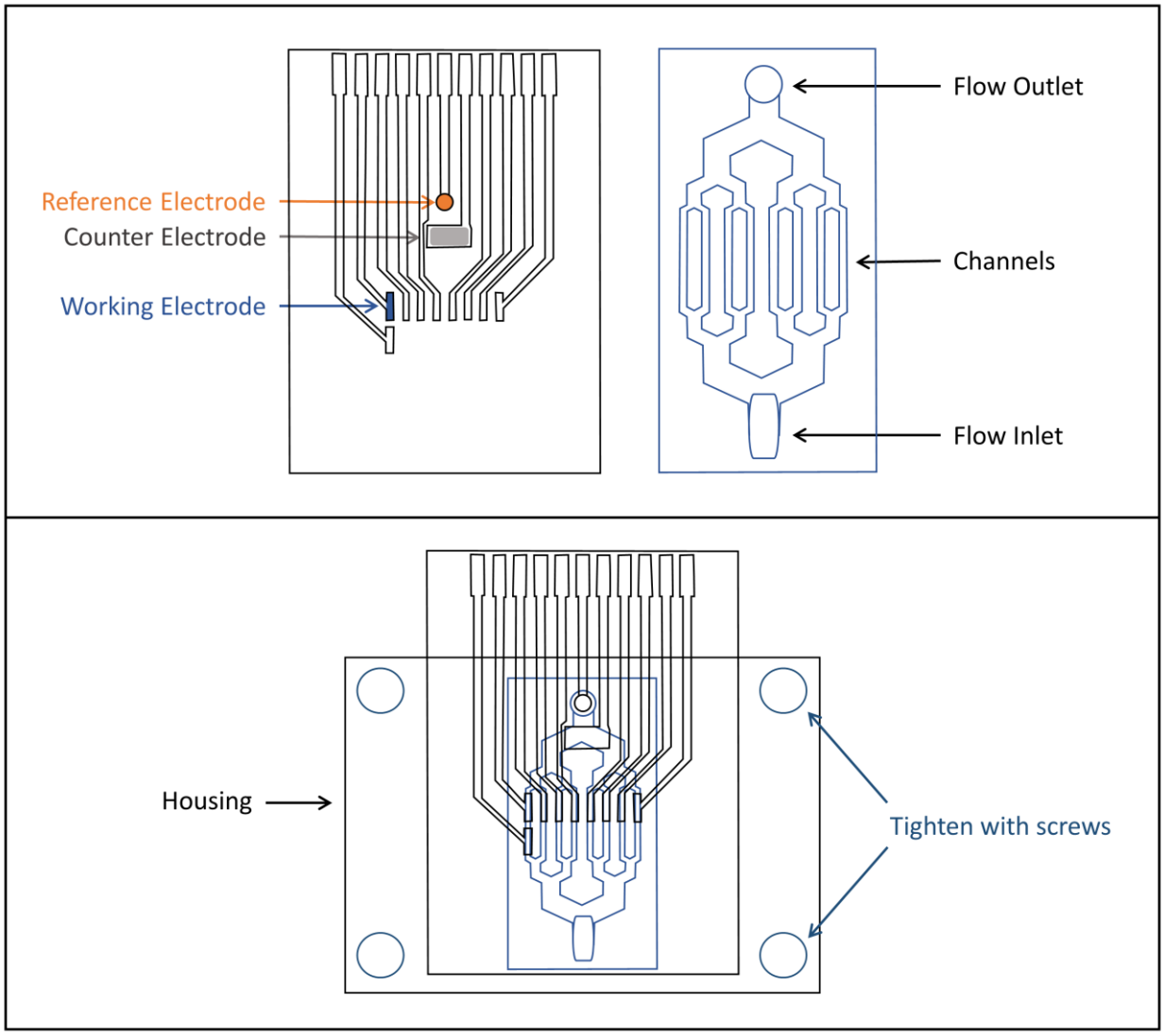

Figure 5.1. Drawings of the 8-Channel Electrode, Microfluidic, and Housing. Top) The 8-channel screen-printed electrode (left) has individual counter and reference electrodes along with eight working electrodes. The microfluidic (right) has an inlet and outlet connected by channels that cover the electrodes. Bottom) The device is assembled by placing the fluidic on top of the electrode and held together with two plates that are tightened with screws.

Experimental

Materials

Tyrosinase from mushroom, adenosine deaminase from calf intestine, nucleoside phosphorylase, xanthine oxidase from bovine milk, glutamate oxidase from *Streptomyces*, choline oxidase from *Alcaligenes*, acetylcholinesterase from *Electrophorus electricus*, adenosine, glutamic acid, acetylcholine chloride, chlorpyrifos, and m-phenylenediamine were purchased from MilliporeSigma (Burlington, MA). Phosphate buffer solution (pH 7), potassium chloride, Hanks' Balanced Salt Solution (with calcium and magnesium, no phenol red), 3-hydroxytyramine, and DL-threo-β-benzyloxyaspartic acid were purchased from Fisher Scientific (Waltham, MA). 24 well plates were purchased from Corning (Corning, NY). SPEs were designed in house and purchased from Pine Research (Durham, NC). Tygon tubing was purchased from Cole Parmer (Vernon Hills, IL). The rotary planar peristaltic micropumps, valves, microclinical analyzers, microcontrollers, and computer software were designed by and purchased from the Vanderbilt Microfabrication Core/Vanderbilt Institute of Integrative Biosystems Research and Education (Nashville, TN). The CHI 1440 potentiostat was purchased from CH Instruments (Austin, TX).

Modifying Sensors with m-Phenylenediamine, Pyrrole, and Nafion

Working electrodes were submerged in an m-phenylenediamine (mPD) solution and a constant potential of 0.745 V vs. a Ag/AgCl reference was applied to deposit the mPD on the electrode surface. Multiple concentrations (5 and 30 mM) and deposition times (15 and 45 minutes) were used to determine the best combination for blocking ascorbic acid and dopamine. Pyrrole was deposited by submerging working electrodes in a 200 mM pyrrole solution and applying a constant potential of 0.8 V vs. Ag/AgCl for 300 seconds. Following this, the sensor was submerged in phosphate buffer solution and held again at 0.8 V vs. Ag/AgCl for 6 hours before

use. Nafion was applied to blank working electrodes by drop casting 0.5 µL and allowed to dry for one hour. To test the ability of each method to mitigate interference, the sensors were calibrated using 10, 20, 30, and 40 µM H_2O_2, ascorbic acid, and dopamine. The slope of each calibration was found, and the selectivity coefficient was calculated for each deposition method for both interferents by dividing the slope of either the ascorbic acid or dopamine calibration by the slope of the H_2O_2 calibration and multiplying by 100.

m-Phenylenediamine Stability

Because the mPD is responsible for mitigating interference from easily oxidized compounds like dopamine and ascorbic acid, it is important to understand how the function of the mPD layer changes over time. This was accomplished using the same protocol as was used for testing the different mPD deposition concentrations and times. Selectivity coefficients were calculated using slopes from calibrations of 10 to 40 µM H_2O_2, ascorbic acid, and dopamine. In the subsequent days, calibrants were run again and the calculated selectivity coefficients were compared to the time zero values to determine how the selectivity of the mPD film to ascorbic acid and dopamine changed. All p-values, unless otherwise specified, were calculated by performing a t-test assuming unequal variances.

Optimization of Adenosine Sensor

Optimization of the adenosine sensor was accomplished by changing the unit ratios of the three enzymes used in sensor creation and performing a calibration to determine how the detection parameters were impacted. Three ratios of ADA:NP:XO were tested: 2:1:1, 1:1:2, and 1:1:1. The amount of glutaraldehyde used to crosslink each solution was adjusted based on the volume of XO

and the total volume of solution. A different crosslinker, polyethylene glycol diglycidyl ether, was also tested with the 1:1:1 enzyme ratio, with 0.525 µL added to the enzyme solution. To test each enzyme ratio, a calibration was run from 1 µM to 200 µM adenosine, and from this the limits of detection and quantitation (LOD and LOQ), sensitivity, and linear range were calculated and compared for each ratio.

Fabrication of Enzyme Sensors

Creation of enzyme sensors was accomplished by depositing enzyme solutions for glutamate, acetylcholine, adenosine, and dopamine onto the 8-channel SPE with two working electrodes per analyte. All enzymes, unless otherwise specified, were dissolved in a 2 mM buffer solution at pH 7 with 800 mg/mL bovine serum albumin (BSA). All enzymes were stored at -18 °C until use, except adenosine deaminase which was stored at 2 °C.

Glutamate and Acetylcholine Sensors

Glutamate and acetylcholine sensors were made as before, with minor alterations.[12,13] Each enzyme was dissolved separately (10 mg/mL) in BSA solution. Glutamate oxidase (5 units/mg) was vortexed with glutaraldehyde (1% by volume) and drop cast onto working electrodes (0.5 µL). Working electrodes were made to be selective for acetylcholine using acetylcholinesterase (137 units/mg) and choline oxidase (15 units/mg). These enzymes were combined equally (v/v) and mixed with glutaraldehyde (2% final concentration, v/v), before being vortexed and drop cast (0.5 µL) onto each working electrode.

Dopamine Sensor

Working electrodes were made to be dopamine sensitive using the tyrosinase enzyme, as has been shown with other electrochemical sensors.[14] Tyrosinase (7164 units/mg) was dissolved

in the BSA solution to a concentration of 10 mg/mL, vortexed with glutaraldehyde (1% by volume), and drop cast (0.5 µL) onto each working electrode.

Adenosine Sensor

Creation of adenosine sensitive electrodes required a solution of 3 enzymes: adenosine deaminase, nucleoside phosphorylase, and xanthine oxidase.[15] Of a number of ratios, a 1:1:1 unit ratio of the three enzymes was found to create the best performing sensor. Both the nucleoside phosphorylase (NP, 0.1 units/µL) and adenosine deaminase (ADA, 1 unit/µL) were used as delivered. Xanthine oxidase (XO) was dissolved in BSA to a concentration of 0.1 units/µL. To create the enzyme solution, 5 µL of NP and XO were mixed with 0.5 µL of ADA. As there is less BSA available for crosslinking than for the other enzyme sensors (5 µL out of 10.5 µL total), slightly more glutaraldehyde (0.22 µL) was added to the 10.5 µL solution before vortexing and drop casting 0.5 µL onto the electrode surface.

Characterization of Enzyme Sensors

The limits of detection (LOD) and quantitation (LOQ), linear range, and sensitivity for all four enzyme sensors were determined using the microformulator pump and valve system. Calibrations were performed by monitoring the current generated by calibrants (5 µM to 1 mM glutamate, 1 µM to 2 mM acetylcholine, 1 µM to 200 µM adenosine, and 1 µM to 400 µM dopamine) in buffer [phosphate buffer solution (50 mM potassium monobasic-sodium buffer, pH 7, Fisher) diluted to 2 mM, plus 120 mM KCl] using a CHI 1440 potentiostat held at 0.6 V vs. Ag/AgCl for glutamate, acetylcholine, and adenosine sensors and -0.2 V vs. Ag/AgCl for the dopamine sensor. For glutamate, acetylcholine, and adenosine, calibrations were performed on enzyme-coated electrodes with mPD deposited on the surface before adding enzymes. Calibrants

were sampled using the microformulator at 100 µL min^{-1} for 2 minutes per calibrant. Linear regressions were performed on the linear ranges of the calibration data. The resulting slopes provided the sensitivity of the electrodes to each analyte. The LODs were calculated by multiplying the error of the blank by three and dividing by the slope. The equation for calculating the LOQ is the same, except the error of the blank is multiplied by ten instead of three. After use, sensors were stored in buffer solution in low light until needed.

Neurotransmitter Sensor Stability

The stability of each sensor was determined by monitoring their sensitivities over a ten-hour period. Calibrants were made for glutamate (25 to 100 µM), acetylcholine (25 to 100 µM), adenosine (5 to 25 µM), and dopamine (10 to 25 µM). The sensitivity of each sensor was calculated every hour and compared to the original sensitivity to determine the change over time. Calibrants were run at 100 µL min^{-1} for two minutes each with buffer solution in between. Following each calibration, buffer solution was run continuously until the next calibration.

Interference Between Neurotransmitter Sensors

Sequential calibrations of the individual neurotransmitters were performed and monitored on all four sensors to investigate the specificity of each sensor. Calibrant solutions were made for glutamate (25 to 100 µM), acetylcholine (25 to 100 µM), adenosine (5 to 20 µM), and dopamine (10 to 40 µM). In preparing the sensor, mPD was electrodeposited onto glutamate, acetylcholine, and adenosine sensors. Calibrants were run at 100 µL min^{-1} for two minutes each with buffer solution in between to set the baseline.

Correction for Dopamine Interference

While high concentrations of dopamine can interfere with the other neurotransmitter sensors, the inclusion of a dopamine sensor allows for the correction of this interference. The 8-channel electrode was calibrated with separate calibrant solutions of glutamate (50 to 250 µM) and dopamine (10 to 30 µM). Three solutions were also made containing known quantities of glutamate and dopamine: Sample 1 (125 µM glutamate and 30 µM dopamine), Sample 2 (175 µM glutamate and 20 µM dopamine), and Sample 3 (225 µM glutamate and 10 µM dopamine). The electrode was calibrated, and the samples were analyzed. The response that the dopamine calibrants generated on the glutamate sensor were used to quantify how much of the sample current was due to dopamine interference. The current determined to be due to dopamine for each sample was then subtracted from the total sample currents. Following this subtraction, the corrected currents were used with the glutamate calibration to calculate the glutamate concentrations. These concentrations were the compared to the known concentrations to determine the viability of current subtraction as a method for correcting dopamine interference.

CPF Treatment of Astrocytes

For this study, astrocytes were differentiated from human induced pluripotent stem cell lines derived from one patient, CE3, similar to previously published works.[44] Following differentiation, astrocytes were harvested and replated onto 24 well plates and grown to confluency before testing. Stock solutions of 1 mM CPF in DMSO, 15 mM glutamate in HBSS, and 50 mM DL-threo-β-benzyloxyaspartic acid (TBOA) were prepared and used to treat the cells. Before beginning treatment, astrocytes were washed with HBSS following the removal of astrocyte medium. After washing, cells were incubated in 0.5 mL of either HBSS (9 wells), HBSS + 10 CPF

(9 wells), or HBSS + 100 µM TBOA (3 wells) for 90 minutes at 37 °C. Following this incubation, an additional 250 µL was added to each well to perform the glutamate uptake portion of the experiment. Three HBSS only wells received an additional 250 µL of HBSS. The other 6 HBSS only wells received 250 µL of HBSS + 600 µM glutamate, resulting in a final concentration of 200 µM glutamate. Similarly, 3 HBSS + CPF wells received 250 µL of HBSS + CPF, while the other 6 were treated with 250 µL of HBSS + CPF + 600 µM glutamate. The 3 wells incubated with TBOA received and addition 250 µL of HBSS + TBOA + 600 µM glutamate. Following an additional 30 minutes of incubation, 650 µL was collected from each well and stored at -2 °C before analysis of glutamate uptake. This procedure was repeated in a 24 well plate without cells, to serve as a control for any interactions that may take place between the treatments and the plate.

Analysis of Glutamate Uptake

The 8-channel SPE along with the microformulator pump and valve system were used to analyze the collected samples for glutamate. Two working electrodes on the 8-channel SPE were coated with a BSA solution for interference analysis, with glutamate oxidase deposited on the other 6. The 30 total samples were run in two sets: 9 control samples with 6 cell samples, followed by the other 15 samples from the cell-coated well plate. Calibrants (25, 50, 100, and 200 µM in HBSS) were run before each sample set. Both calibrants and samples were run by the microformulator for two minutes each, with two minutes of HBSS in between to set a baseline. Calibrants and samples were analyzed amperometrically, with all 8 working electrodes held at 0.6 V vs. Ag/AgCl. Calibration curves were created from the collected data for each electrode, and from these the concentration of glutamate present in the samples was determined. All uptake values were calculated based on the treatment concentrations determined from the controls.

Results and Discussion

One of the main challenges in developing an electrode array to detect multiple neurotransmitters simultaneously is making each electrode specific for the analyte of interest. Having one electrode sensitive to multiple analytes can lead to challenges in quantification. The electrode array presented here functions through the oxidation of H_2O_2 for the detection of glutamate, acetylcholine, and adenosine—occurring at 0.6 V vs. Ag/AgCl. These three sensors utilize oxidase enzymes to generate H_2O_2, which can be oxidized and is proportional to analyte concentration. The other neurotransmitter of interest, dopamine, is easily oxidized at 0.6 V and its presence can cause substantial current response on the electrodes that have been modified to detect the other neurotransmitters.

To mitigate this interference, a layer of m-phenylenediamine (mPD) was deposited on the other neurotransmitter (glutamate, acetylcholine, and adenosine) electrodes to block larger compounds like dopamine and ascorbic acid while still allowing the passage of the smaller H_2O_2. Previous studies have investigated the use of permselective films like mPD to mitigate interference from compounds like dopamine and ascorbic acid, though not in microfluidic systems.[47,98,99] Here, multiple mPD deposition protocols were used with varying deposition times and concentrations. An overoxidized polypyrrole deposition was also investigated, as it has been shown previously to successfully mitigate dopamine interference.[99] For comparison, Nafion—a polymer sometimes used to block ascorbic acid interference—and a blank electrode were also tested. Selectivity coefficients were calculated by dividing the sensors sensitivity to either dopamine or ascorbic acid by the sensitivity to H_2O_2 and multiplying by 100. A smaller number is therefore indicative of selectivity towards H_2O_2 and a mitigation of interference. Sensitivities for each analyte and calculated selectivity coefficients are presented in **Table 5.1**.

Deposition	Sensitivity (nA μM^{-1} mm^{-2})			Selectivity Coefficients	
	H_2O_2	Ascorbic Acid	Dopamine	Ascorbic Acid	Dopamine
30 mM mPD 45 minutes	1.2 ± 0.1	0.09 ± 0.01	0.12 ± 0.01	7 ± 1	10 ± 1
30 mM mPD 15 minutes	0.84 ± 0.04	0.09 ± 0.03	0.22 ± 0.02	11 ± 2	26 ± 1
5 mM mPD 45 minutes	1.7 ± 0.5	0.09 ± 0.03	0.17 ± 0.03	7 ± 1	12 ± 2
5 mM mPD 15 minutes	4.2 ± 0.1	0.34 ± 0.08	0.43 ± 0.08	8 ± 2	9 ± 1
Pyrrole	0.4 ± 0.1	0.08 ± 0.02	0.5 ± 0.2	18 ± 2	123 ± 23
Nafion	2.9 ± 0.9	0.3 ± 0.2	3.5 ± 0.8	15 ± 9	121 ± 7
Blank	4.4 ± 0.1	3.1 ± 0.1	3.9 ± 0.1	71 ± 2	89 ± 2

Table 5.1. Testing mPD Deposition Times and Concentrations. The effectiveness of mPD, deposited with different concentrations and deposition times, and pyrrole layers were studied and compared to Nafion-coated and blank electrodes. The sensitivities of each electrode to H_2O_2, ascorbic acid, and dopamine were found, and these values were used to determine the selectivity coefficients for each deposition method. Overall, the 5mM mPD, 15-minute deposition was chosen as it maintained H_2O_2 sensitivity most similar to the blank electrode, while still blocking ascorbic acid and dopamine as well as higher mPD concentrations and deposition times.

While the Nafion film successfully blocked some ascorbic acid interference, it was not useful in mitigating dopamine interference. The pyrrole coating did decrease interference from ascorbic acid and dopamine compared to the blank, but also blocked H_2O_2 from reaching the electrode surface, diminishing the effectiveness of the sensor. All four mPD deposition protocols significantly decreased the selectivity coefficients of ascorbic acid and dopamine compared to the blank electrode. Increasing deposition time and mPD concentration had minimal effect on the selectivity coefficients of ascorbic acid or dopamine. There was, however, a substantial decrease in the sensitivity of the electrode to H_2O_2 with increasing deposition time and concentration, decreasing from 4.2 ± 0.1 nA μM^{-1} mm^{-2} at 5 mM mPD for 15 minutes, to 1.2 ± 0.1 nA μM^{-1} mm^{-2} at 30 mM mPD for 45 minutes. Because the glutamate, acetylcholine, and adenosine sensors

function through oxidation of H_2O_2, it is important to retain as much sensitivity to H_2O_2 as possible while still blocking interferents. Due to this, the deposition protocol of 5 mM mPD for 15 minutes was chosen as the optimal procedure and was used for all experiments with mPD.

To further characterize the usefulness of the mPD-modified sensor, the longevity of the mPD layer was analyzed to determine for how long the sensor was able to maintain its ability to mitigate interference from ascorbic acid and dopamine. Following mPD deposition, selectivity coefficients calculated for ascorbic acid and dopamine were low—5 ± 1 and 10 ± 1, respectively (**Figure 5.2**). The sensor was tested again 24 hours after mPD deposition, and though the ascorbic acid selectivity coefficient did not change significantly ($p \leq 0.53$), the selectivity coefficient for dopamine increased from 10 ± 1 to 39 ± 3 ($p \leq 0.0002$). From there, the selectivity coefficients for both ascorbic acid and dopamine increased each day—reaching 76 ± 2 and 143 ± 4, respectively, after a week. Using the calibrations to calculate LODs provides another way to quantify how well the mPD film is blocking the interferents. Immediately following mPD deposition the LOD of dopamine was calculated to be 6 ± 1 µM, significantly greater than the 0.7 ± 0.2 µM LOD of the blank ($p \leq 0.008$). As concentrations of dopamine as high a 6 µM are rare within biological samples, the mPD film blocked most if not all the interference that could be expected from dopamine on the other enzyme sensors. The LOD dropped every day following, and at day 7 was 0.6 ± 0.1 µM—no different from the blank ($p \leq 0.57$). A similar pattern was seen for ascorbic acid, with the LOD falling from 11 ± 2 µM to 1.1 ± 0.3 µM after a week. Due to the decreasing performance of the mPD layer over time, experiments utilizing mPD for dopamine mitigation were done as soon after deposition as possible.

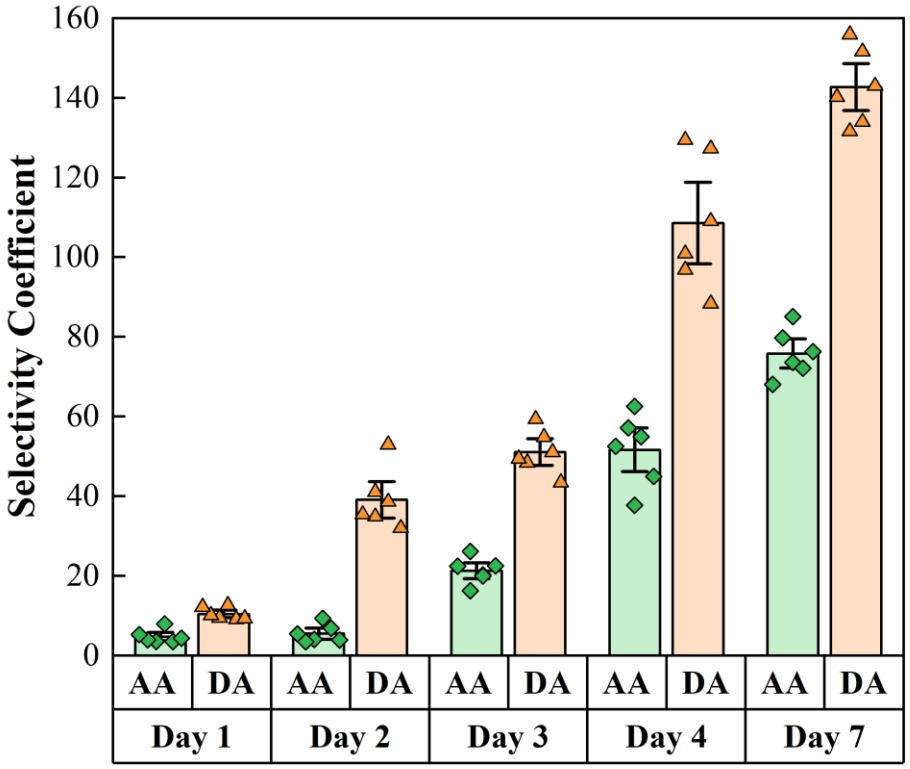

Figure 5.2. Stability of mPD Layer Over One Week. The ability of the mPD layer to exclude ascorbic acid and dopamine was tested immediately after deposition and for the following week. Calibrations of the sensor with H_2O_2, ascorbic acid, and dopamine were done, and the ratio of the slopes was used to calculate the selectivity coefficients. After 24 hours, there was no significant difference in the selectivity coefficients for ascorbic acid ($p \leq 0.15$). The selectivity coefficient for dopamine increased significantly after 24 hours, indicating the mPD layer was no longer effectively blocking dopamine from the sensor surface ($p \leq 0.003$). After 24 hours, both dopamine and ascorbic acid selectivity coefficients substantially increased each day. Due to this, any experiments utilizing mPD were performed soon after deposition.

Following mPD characterization, each individual neurotransmitter sensor was studied for sensitivity, limit of detection and quantitation (LOD and LOQ), linear range, V_{max}, and K_m to assist in determining the biological relevance of each sensor (**Figure 5.3**). Sensor parameters are reported for the four neurotransmitter sensors in **Table 5.2.** All four sensors had LODs between one and two micromolar, with LOQs ranging from 3.7 ± 0.3 µM in the case of glutamate to 6 ± 1 µM for dopamine. The relevance of these values is dependent upon the neurotransmitter in question. Biological concentrations of glutamate can range from the low single digit micromolar to hundreds of micromolar under conditions of stress. The linear range of the glutamate sensor, 4 to 300 µM, is well suited to studying this range of concentrations and can therefore be used to investigate many of the biological processes that alter glutamate concentration. The linear range for the acetylcholine sensor was similarly wide (4 to 100 µM) and may be used to quantify large increases in acetylcholine concentration such as those seen following exposure to acetylcholinesterase inhibitors like CPF. Though resting concentrations of extracellular adenosine range from 30 to 300 nM, concentrations can reach as high 50 µM following ischemia.[100] While the adenosine sensor cannot monitor basal adenosine levels in its present form, the sensor could prove useful for monitoring the mechanisms of an ischemic event. Similarly, cellular release of dopamine generally only results in nanomolar concentrations of extracellular dopamine, though dopamine has been used clinically to treat conditions of shock and as a blood pressure regulator.[101,102] The enzymatic dopamine sensor presented here, with a linear range of 6 to 30 µM, is directly applicable to analyzing systems treated with higher concentrations of dopamine.

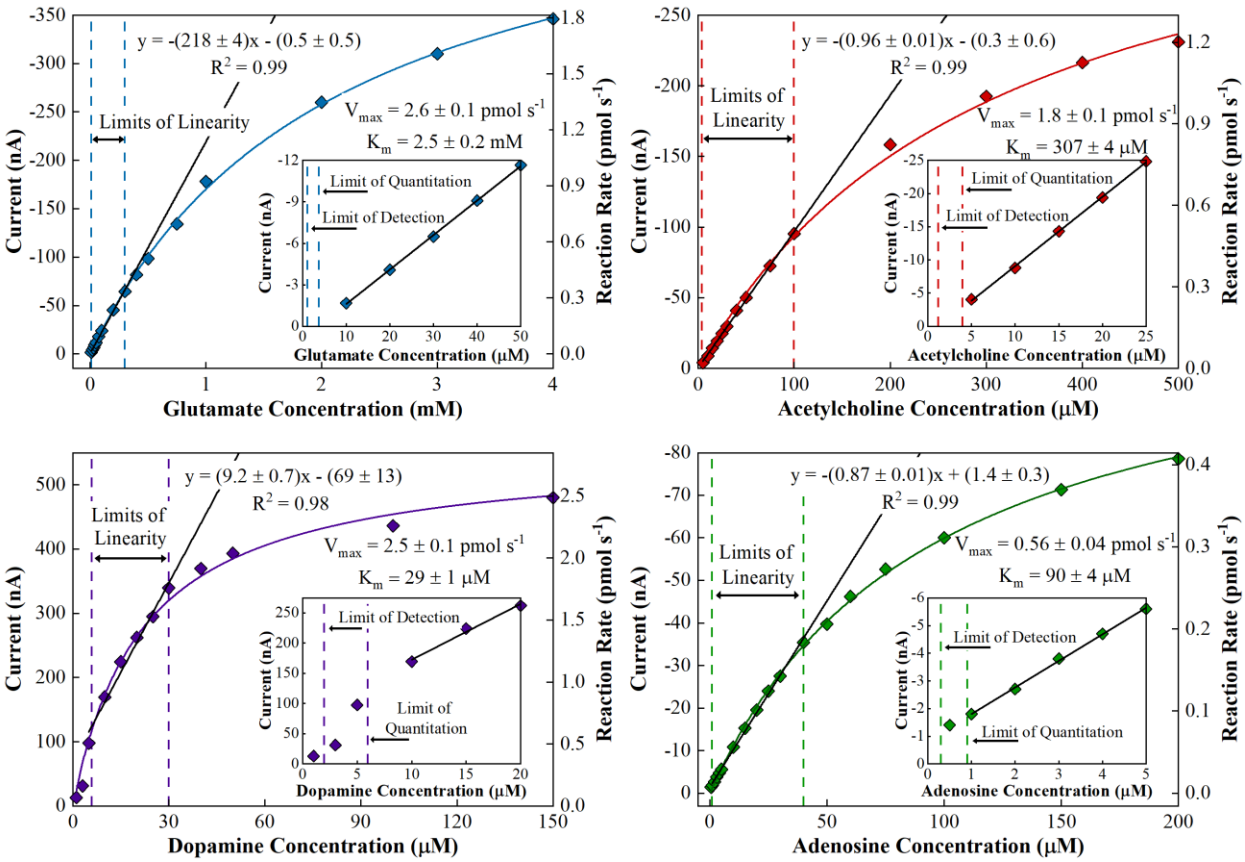

Figure 5.3. Representative Calibrations of Neurotransmitter Sensors on the 8-Channel Electrode. Following mPD and enzyme deposition, the neurotransmitter sensor was calibrated individually with all four analytes for the determination of characteristics including linear range, LOD and LOQ, sensitivity, V_{max}, and K_m.

Sensor	Glutamate	Acetylcholine	Adenosine	Dopamine
Sensitivity ($nA\ \mu M^{-1}\ mm^2$)	0.13 ± 0.01	0.5 ± 0.1	0.64 ± 0.03	8 ± 1
LOD (µM)	1.1 ± 0.1	1.2 ± 0.3	0.3 ± 0.1	1.9 ± 0.3
LOQ (µM)	3.7 ± 0.3	4 ± 1	0.9 ± 0.2	6 ± 1
Linear Range (µM)	4 - 300	4 - 100	1 - 40	6 - 30
V_{max} ($pmol\ s^{-1}$)	2.6 ± 0.1	1.8 ± 0.1	0.56 ± 0.04	2.5 ± 0.1
K_m	2.5 ± 0.2 mM	307 ± 4 µM	90 ± 4 µM	29 ± 1 µM

Table 5.2. Characteristics of Neurotransmitter Enzyme Sensors. Calibrations were performed individually for all four neurotransmitter sensors, with the glutamate, acetylcholine, and adenosine electrodes having been coated with mPD first. From these calibrations the sensitivity, LOD, LOQ, linear range, V_{max}, and K_m were found for each neurotransmitter sensor.

In characterizing the adenosine sensor, the ratios of the three different enzymes were adjusted to determine which ratio provides the best sensor performance. The enzymatic mechanism of the adenosine sensor begins with ADA deaminating adenosine to make inosine. Inosine is then cleaved by nucleoside phosphorylase, and the resulting hypoxanthine can be oxidized by xanthine oxidase—resulting in the production of H_2O_2. This H_2O_2 can then be oxidized at 0.6 V vs. Ag/AgCl. Three different enzyme ratios were tested, and the detection parameters for each ratio were calculated (**Table 5.3**). Doubling the unit concentration of ADA relative to the other enzymes resulted in a lower sensitivity and linear range than the other two ratios, with the sensor losing over 70% of its response over 10 hours. While the other two ratios tested provided similar sensitivities, LODs, and LOQs, the 1:1:1 enzyme ratio provided a linear range larger than the 1:1:2 ratio while also retaining 86% of its response over a 10-hour period. Because of this, the 1:1:1 enzyme ratio was used in all experiments where the adenosine sensor was used.

Enzyme Ratio (ADA:NP:XO)	**2:1:1 (n = 1)**	**1:1:1 (n = 2)**	**1:1:2 (n = 1)**
Sensitivity (nA μM^{-1} mm^{-2})	0.29	0.64 ± 0.03	0.65
LOD (µM)	0.2	0.3 ± 0.1	0.3
LOQ (µM)	0.7	0.9 ± 0.2	1.0
Linear Range (µM)	1 - 25	1 - 40	1 - 30
Signal After 10 Hours (%)	29%	86%	61%
Volume of XO [(Total Volume), µL]	5 (12)	5 (10.5)	10 (15.5)
Glutaraldehyde Added (µL)	0.24	0.21	0.16

Table 5.3. Optimization of Adenosine Detection Parameters. Multiple ratios of the three enzymes making up the adenosine sensor were tested to determine which ratio provided the most effective sensor. Calibrations were run from 1 to 200 µM adenosine and from these the LOD, LOQ, sensitivity, stability, and linear range were found for each ratio. Overall, the 1:1:1 ratio provided the best detection parameters while also retaining most of its sensitivity over 10 hours.

Following sensor characterization, the stability of each enzyme sensor was studied over a period of 10 hours. One drawback to enzymatic sensors is their tendency to lose responsiveness over relatively short periods of time, necessitating frequent calibration and complicating quantitative measurements. The enzyme sensors remained relatively stable over 10 hours, with the best performing sensor—glutamate—retaining 97% of its response (**Figure 5.4**). The dopamine sensor lost the most sensitivity, measuring at 68% of the original response at the end of the experiment. The acetylcholine and adenosine sensors maintained 90 ± 1% and 86 ± 1% of their signal, respectively. While methods other than enzymatic detection may provide greater stability, the relatively low cost and ease-of-use make enzyme sensors an attractive technique for many experiments. These sensors, incorporated with the microformulator pump and valve system, constitute a system that can be automated to calibrate and analyze biological samples.

While the mPD layer utilized here can block up to 6 µM dopamine under optimal conditions, high concentrations of dopamine may still generate a current response on the glutamate, acetylcholine, and adenosine sensors. To assess the response of high dopamine

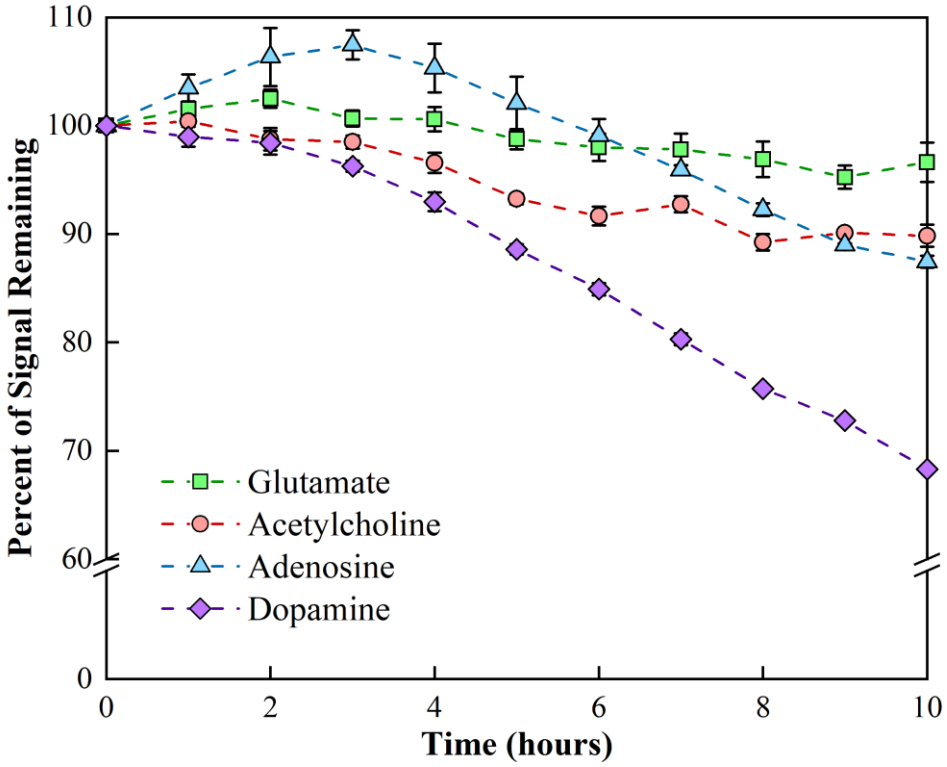

Figure 5.4. Stability of Neurotransmitter Sensors. The stability of all four neurotransmitter sensors was tested over a period of 10 hours. Calibrations were performed every hour, with the sensitivity of each sensor compared to its sensitivity at time 0 to determine how sensor performance was affected. The glutamate sensor performed the best, retaining 97 ± 2% of its sensitivity after 10 hours. The dopamine sensor performed the worst, with 68 ± 1% of the original sensitivity remaining. Acetylcholine and adenosine maintained 90 ± 1% and 86 ± 1% of their signal, respectively.

concentrations on the other sensors, individual calibrant sets containing only one neurotransmitter were run consecutively over an SPE modified to detect all four neurotransmitters. All four sensors were specific for their analytes of interest, except for the dopamine calibrants (**Figure 5.5**). The dopamine calibrants generated a significant current response on all four sensors, as even with the mPD layer, some dopamine reached the electrode surface and oxidized at 0.6 V vs. Ag/AgCl. If dopamine is present in high concentrations with other neurotransmitters of interest, quantification based on current response could become an issue as the current generated by dopamine would lead to an overestimation of the other neurotransmitter concentrations.

The inclusion of a dopamine sensor on the SPE provides a way not only to monitor the concentration of dopamine, but also to correct the other neurotransmitter sensors if high concentrations of dopamine are present. To demonstrate this, the multi-neurotransmitter sensor was calibrated with both glutamate and dopamine calibrants **(Figure 5.6)**. Separate solutions were made containing known concentrations of both glutamate and dopamine, simulating samples that could be collected and analyzed from a biological experiment. The dopamine calibration was used to determine the amount of current that the dopamine in the samples generated on the glutamate electrode. The current determined to be generated by dopamine can then be subtracted from the overall current generated on the glutamate electrode, leaving only the current generated by glutamate. For example, after correcting for the dopamine current in Sample 2, the sample current response was only 1 nA different than what the glutamate calibration indicated as 175 µM glutamate. This not only demonstrates the use of the dopamine sensor as a method for quantifying high quantities of dopamine, but also its use in providing more accurate analysis of biological samples containing dopamine.

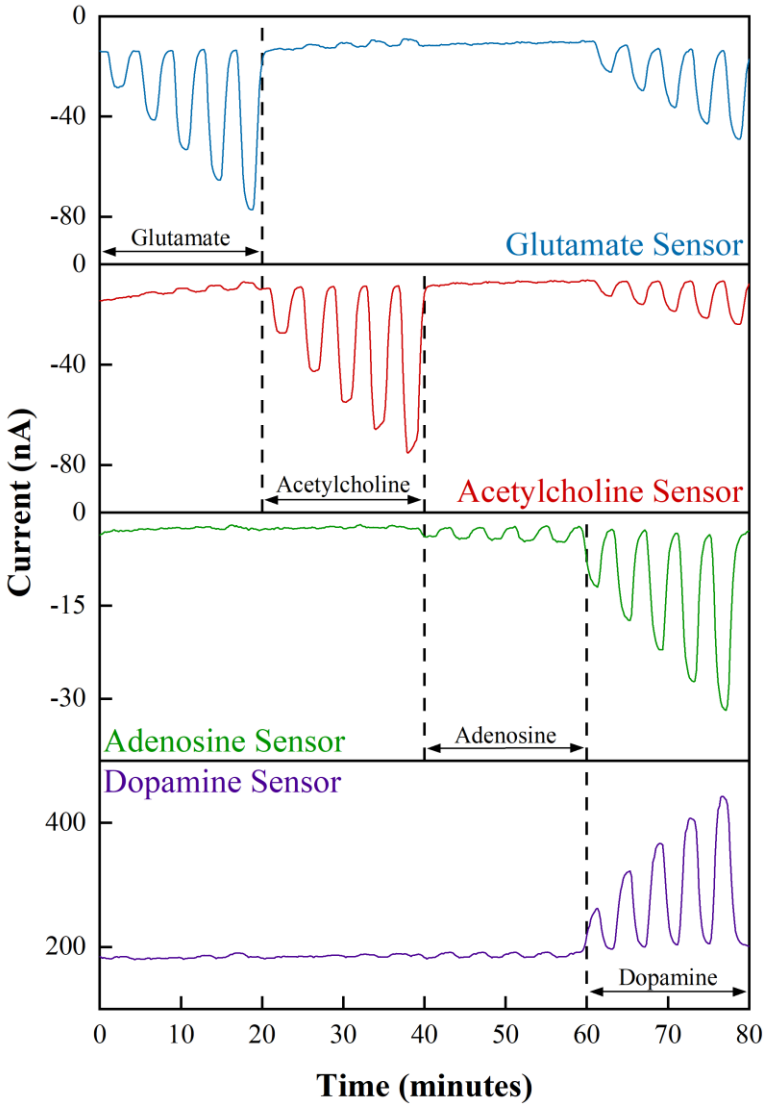

Figure 5.5. Individual Calibrations of the Neurotransmitter Sensors. An 8-channel electrode with all four neurotransmitter enzyme films deposited was calibrated with each analyte individually. Glutamate, acetylcholine, and adenosine calibrants produced little response on electrodes that were not their specific enzyme electrode. Dopamine however produced a response on all 4 electrodes, including those with an mPD layer.

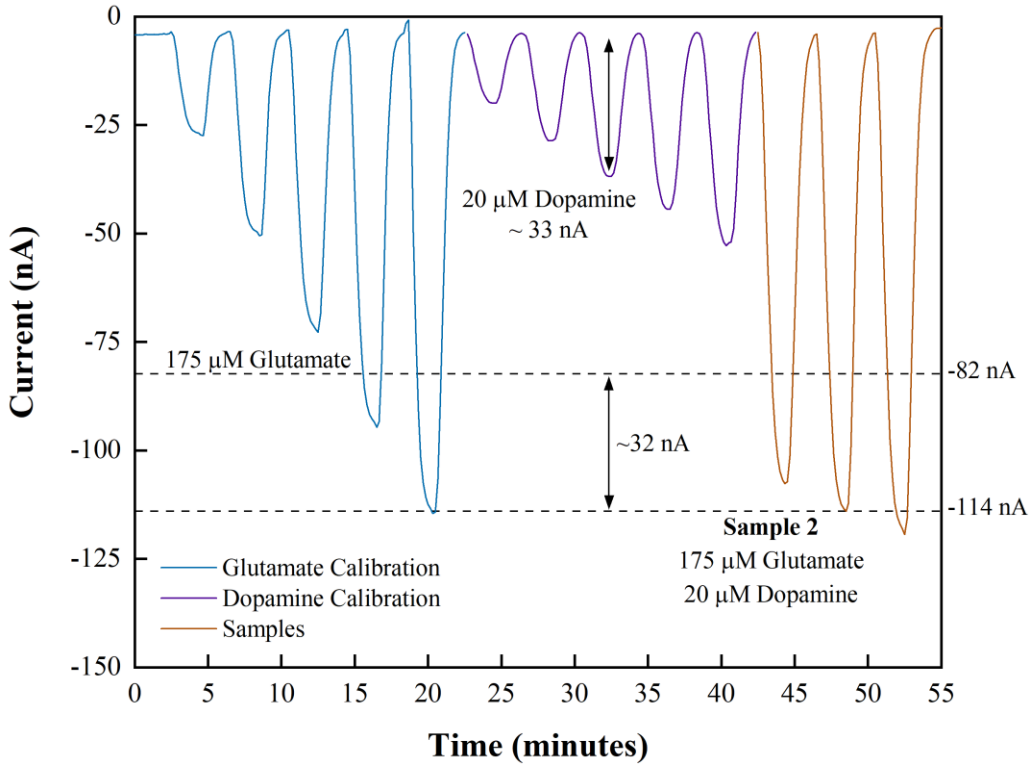

Figure 5.6. Dopamine Interference and Correction. Though mPD blocks much of the interference from dopamine, it does not block 100%. Here, samples were run over a glutamate sensor in which the concentrations of glutamate and dopamine were known. After calibrating with glutamate and dopamine it was shown that the sample current values can be corrected by subtracting the current generated by the dopamine to give accurate values for the analyte of interest.

Chlorpyrifos is a widely used organophosphate pesticide, well known for its ability to inhibit acetylcholinesterase in the brain. In addition to acetylcholinesterase inhibition, CPF has also been demonstrated to dysregulate the release of glutamate from glutamatergic neurons, which under that right circumstances may lead to excitotoxic quantities of glutamate in the brain.[94,95] Astrocytes are a type of glial cell that take up substantial amounts of glutamate from the extracellular space through their excitatory amino acid transporters. Uncovering the effects CPF on glutamate uptake in astrocytes is essential in understanding the overall impact that CPF may have on neuronal glutamate metabolism. Here, astrocytes were treated for 90 minutes with CPF or TBOA, a glutamate uptake inhibitor, followed by a 30 minute 200 µM glutamate treatment to assess the effects of CPF and TBOA on the ability of astrocytes to take up glutamate compared to the control treatment (HBSS only). Samples collected from wells not treated with CPF measured at 69 ± 1 µM, as cells took up 98 ± 1 nmoles (65 ± 1%, **Figure 5.7**). Uptake increased significantly ($p \leq 0.004$) for those treated with CPF for 90 minutes, as these samples measured at 62 µM with a total uptake of 103 ± 1 nmoles (69 ± 1%). TBOA treatment—previously demonstrated to inhibit glutamate uptake—significantly decreased glutamate uptake ($p \leq 1e\text{-}6$) with collected samples measuring at 98 µM with a total uptake of 76 ± 1 nmoles (51 ± 1%).[103] These data indicate that CPF may have a substantial impact on glutamate metabolism within the brain. Future work in this area could include dose or time response experiments, as well as testing the effects of the more toxic metabolite CPO. The study of CPF/CPO effects on human neuronal glutamate release or neuron/astrocyte co-cultures could further increase understanding of OP impacts on overall glutamate metabolism.

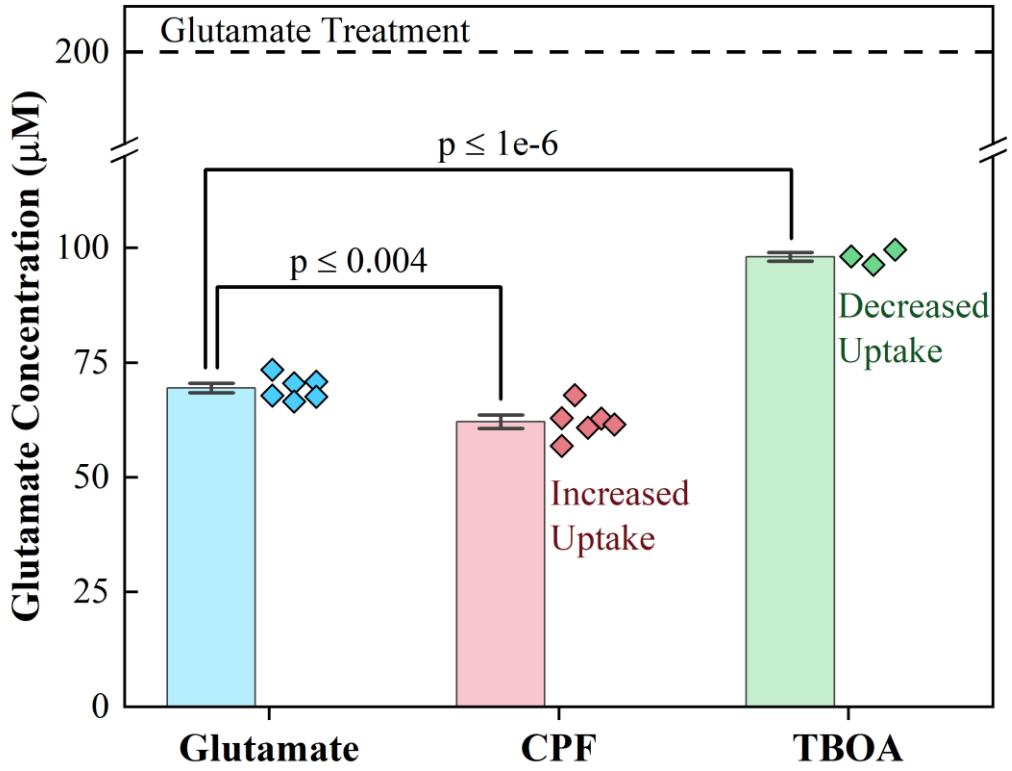

Figure 5.7. Glutamate Uptake by CE3 Astrocytes Treated with CPF or TBOA. The uptake of 200 µM glutamate was investigated in astrocytes that had been exposed to CPF or TBOA for 90 minutes and compared to those that had not. Astrocytes not treated with CPF measured at 69 ± 1 µM glutamate, as cells took up 98 ± 1 nmoles (65 ± 1%). Uptake increased significantly ($p \leq 0.004$) for astrocytes treated with CPF for 90 minutes, as these samples measured at 62 µM ± 1 glutamate with a total uptake of 103 ± 1 nmoles (69 ± 1%). Astrocytes treated with TBOA, a glutamate uptake inhibitor, took up significantly less glutamate ($p \leq 1e\text{-}6$) than the control astrocytes. Samples from TBOA-treated astrocytes measured at 98 ± 1 µM, an uptake of only 76 ± 1 nmoles (51 ± 1%). All uptake values were calculated based on the control samples for that treatment. All p-values were calculated by performing a t-test assuming unequal variance.

Conclusions

In this work, an 8-channel SPE was modified with four different enzyme solutions and used to simultaneously detect glutamate, acetylcholine, adenosine, and dopamine. Each enzyme sensor was individually characterized, with all sensors displaying low limits of detection and linear ranges wide enough for application to a variety of biological systems. Layers of mPD deposited on the enzyme sensors, excluding dopamine, showed a significant mitigation of interference from both dopamine and ascorbic acid—with its efficacy decreasing in subsequent days. Despite this, subtraction of currents generated by dopamine on other sensors was shown to be a feasible method for correcting currents from biological samples containing high dopamine concentrations. Lastly, the ability of CE3 astrocytes to uptake glutamate was investigated. Following exposure to 10 μM CPF, uptake increased significantly compared to those not treated with CPF. In contrast, TBOA—an EAAT inhibitor known to disrupt glutamate uptake—significantly decreased the amount of glutamate taken up by astrocytes following exposure. This multi-neurotransmitter SPE, coupled with the microformulator system, may in the future be used to simultaneously monitor the complex interactions between neurotransmitters within a biological system.

Acknowledgments

This work was supported in part by EPA grant number 83950401-0 and used the resources of the Vanderbilt Microfabrication Core operated by the Vanderbilt Institute for Integrative Biosystems Research and Education. The authors would like to thank Kaixuan Xu for assistance in designing, performing, and interpreting experiments, Dusty R. Miller for assistance in designing and performing experiments, and M. Diana Neely for providing the astrocytes.

Chapter VI

MODELING DOWNSTREAM ELECTROCHEMICAL ANALYSIS OF AN ORGAN-ON-A-CHIP SYSTEM

Introduction

An organ-on-a-chip (OoC) is a microfluidic, *in vitro* cell culture system that aims to reproduce the dynamic physical and functional features of entire organs and tissues. OoCs have been developed for a variety of human organs including the lung, heart, liver, and kidney—with some models even comprised of multiple organs.[20,39,104–106] These systems play an important role in the development of novel drugs and the assessment of drug and chemical toxicity. While animal models can capture many complex processes related to drug and toxicant exposure, differences between species means that sometimes these models are not fully representative of human physiology.[107] A variety of cells can be cultured within an OoC, from primary cells to differentiated stem cells, providing a tissue specific microenvironment that may more accurately represent human response than many animal models.[108] As OoCs are microfluidic, they are well suited to the application of *in situ* or in-line analysis techniques that can provide high resolution data on changes occurring within the OoC microenvironment.[109] As such, a significant effort has been put towards developing chemical sensors and analytical methods that can be integrated within and downstream of OoCs.

The integration of analysis systems that can provide a high temporal resolution for an extended period is essential to reaching the full potential of OoCs. Two main methods of analysis will be discussed in this work: *in situ* and in line. *In situ* analysis is performed directly within the

area of interest. One early example of an instrument performing *in situ* detection is the multianalyte microphysiometer (MAMP). The MAMP achieved real-time electrochemical analysis through the enzymatic modification of a sensor head that could be placed within a microfluidic chamber containing a cell-coated transwell.[110,111] More recently, techniques for implementing *in situ* electrodes within OoCs have been developed. One platform, for example, was designed with the ability to plug in enzymatically modified electrodes along the microfluidic culture chamber—allowing for flexibility in analyte detection.[27] While platforms utilizing *in situ* detection provide a high spatial and temporal resolution, their designs can be both complex and specific. The development of analysis systems compatible with a variety of OoCs could provide a consistency in analysis across platforms while also decreasing cost compared to designing *in situ* detections systems.

In-line analysis refers to the downstream, real-time analysis of an OoC through the direct connection of the OoC to the detection method. Methods of downstream detection can range from mass spectrometry to electrochemical sensors.[112,113] Some in-line detection platforms, such as the microclinical analyzer (μCA), are designed in a way that allows for integration with a variety of OoC devices.[17] Here, the downstream screen-printed electrode (SPE) can be easily accessed for enzymatic modification, providing flexibility in analyte detection. The use of tubing to perfuse the SPE within the μCA means that the platform can be coupled to any microfluidic OoC device. Analysis of metabolite concentration downstream of the organ system in this manner does present some challenges, as eluate may be affected by diffusion and liquid mixing—lowering the resolution of the collected data.

In this work, the μCA was used to investigate the challenges of downstream electrochemical analysis of OoC systems. A two-μCA setup was used to study the effects of

mixing and diffusion on downstream analysis, with the upstream μCA simulating an OoC device and the downstream μCA used for quantification. The redox couple of ferricyanide/ferrocyanide was used to simulate consumption/production of metabolites within the upstream system, with the changes then measured at the downstream μCA (**Figure 6.1**). The impact of flow rate, flow path, and electrode orientation on crosstalk between enzyme-coated electrodes was investigated. Lastly, the effects of flow rate and pore size on the permeability of the NVU model blood-brain barrier were studied.

Experimental

Materials

Potassium hexacyanoferrate (II) trihydrate, luciferin, and 10 kDa FITC dextran were purchased from MilliporeSigma (Burlington, MA). Phosphate buffer solution (pH 7), potassium chloride, and potassium ferricyanide were purchased from Fisher Scientific (Waltham, MA). Tygon tubing was purchased from Cole Parmer (Vernon Hills, IL). Syringe pumps were purchased from New Era Pump Systems (Farmingdale, NY). SPEs were designed in house and purchased from Pine Research (Durham, NC). The rotary planar peristaltic micropumps, valves, microclinical analyzers, microcontrollers, neurovascular units, and computer software were designed by and purchased from the Vanderbilt Microfabrication Core/Vanderbilt Institute of Integrative Biosystems Research and Education (Nashville, TN). The CHI 1440 potentiostat was purchased from CH Instruments (Austin, TX).

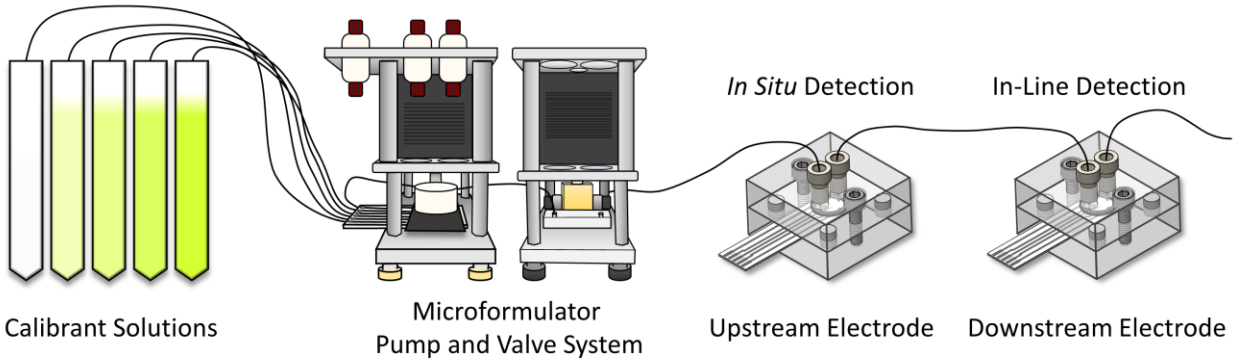

Figure 6.1. Experimental Setup for Monitoring Analyte Consumption and Production. A two-µCA setup and the redox couple of ferri/ferrocyanide was used to quantify the effects of upstream analyte production and consumption on the accurate quantification of analytes downstream. The upstream µCA was used to simulate an OoC device with *in situ* detection, while the downstream µCA used to simulate in-line detection.

Measuring Analyte Consumption Downstream

The effects of upstream analyte consumption on the quantification of analyte downstream were investigated using flow rates of 2, 20, and 200 µL min^{-1}. Two µCAs connected by 15 cm of tygon tubing were used for these experiments. To begin, the downstream SPE was calibrated with 250, 500, 750, and 1000 µM potassium ferricyanide. Following calibration of the downstream SPE, the µCAs were connected and 500 µM potassium ferricyanide was run through with both measuring current response at -0.2 V vs. Ag/AgCl. The amount of time ferricyanide was run varied with flow rate: 2 minutes for 200 µL min^{-1}, 5 minutes for 20 µL min^{-1}, and 30 minutes for 2 µL min^{-1}. To determine how much ferricyanide was consumed by the upstream SPE, the flux was calculated using *Equation 4*, where *i* is the current generated by 500 µM potassium ferricyanide, *n* is the number of electrons in the reaction (1), *F* is Faraday's Constant, *A* is the area of the working electrode (1.8 mm^2), and *J* is the flux.

$$J = \frac{i}{nFA} \tag{4}$$

Flux is equal to mass transfer times concentration, so after finding the flux the mass transfer values at each flow rate were also calculated. The flux values, originally in mol s^{-1} cm^{-2}, were converted to nmoles s^{-1} and the concentration of analyte flowing to the downstream µCA was determined. The current measured at the downstream SPE was then used to calculate the concentration within the µCA, and thus the effects of consumption by the upstream SPE on substrate concentration downstream. Following this, the upstream µCA was disconnected from electrochemical detection and 500 µM potassium ferricyanide was again run through both µCAs. The concentration measured at the downstream µCA was again found and used to determine how diffusion contributed to changes in analyte quantification.

Measuring Analyte Production Downstream

The effects of diffusion on downstream electrochemical analysis of analyte production were investigated using similar methods to the consumption experiments. The reduction of potassium ferricyanide to potassium ferrocyanide was used to simulate cellular metabolite production. To begin, the downstream SPE was calibrated with potassium ferrocyanide using 250, 500, 750, and 1000 µM calibrants. After connecting the two µCAs together as before, 500 µM potassium ferricyanide was run through both µCAs with the upstream SPE held at -0.2 V vs Ag/AgCl to produce potassium ferrocyanide, and the downstream SPE held at 0.6 V vs. Ag/AgCl to detect the ferrocyanide through oxidation. The flux at the upstream SPE was calculated again according to *Equation 4* to determine how much ferrocyanide was produced. The calibration curve, along with the current generated downstream, was used to quantify the concentration of ferrocyanide at the downstream SPE. These values were compared with the flux at the upstream SPE to determine how much ferrocyanide was lost to diffusion.

Measuring Crosstalk Between Electrodes

Crosstalk between electrodes was measured with two different flow profiles: normal and inverted. For normal flow, the flow inlet was attached to the port closest to the electrode connections with the outlet at the bottom of the electrode. With electrode connections at the top, working electrodes are numbered from 1 to 3, left to right. Glucose oxidase was deposited on the middle electrode (E2) with lactate oxidase on the two outer electrodes (E1 and E3). A single solution of 5 mM glucose and 500 µM lactate was used for all crosstalk experiments. In the normal flow configuration, E2 has the greatest potential to generate crosstalk as it is the farthest upstream. The responses of E1 and E3 to lactate were first measured individually. E2 was then turned on,

and lactate was again separately measured at E1 and E3, with E2 measuring glucose. The changes in current at E1 and E3 with E2 on/off were then compared. This experiment was performed at three different flow rates: 100, 20, and 10 µL min^{-1}.

To measure crosstalk in the inverted flow configuration, the flow inlets and outlets were switched. The flow inlet was connected to the port closest to the bottom of the electrode, with the outlet at the port closest to the electrode connections. In this flow direction, E1 and E3 have the greatest potential for generating crosstalk at the downstream E2. Glucose oxidase was deposited on E1 and E3, with lactate oxidase on E2. The same 5 mM glucose, 500 µM lactate solution was used as before. The current generated by E2 with E1/E3 off, E2 and E1 on, and E2 and E3 on was measured and compared at 100, 20, and 10 µL min^{-1}.

NVU Permeability

The effects of pore size and flow rate on the permeability of a model blood-brain barrier, the neurovascular unit (NVU), were investigated for pore sizes of 0.4 µm polycarbonate, and 1.0 and 3.0 µm PET membranes at flow rates of 2, 10, and 20 µL min^{-1}. The permeability experiments were performed with both FITC-dextran (10 µM, MW 10 kDA) and luciferin (20 µM, MW 280 Da) delivered by syringe pumps. Either the luciferin or FITC was delivered to the vascular side of the device, with water flowing through the neuronal chamber, and the eluate was collected from both chambers. Analysis of the samples was done by fluorescence using a low volume (1 mL) quartz cuvette. Collected samples were diluted by 10 times with water to allow enough volume for fluorescent analysis. Solutions of 0, 78, 156, 313, 625, and 1250 µM FITC and 0, 250, 500, 1000, and 2000 µM luciferin were used to create calibration curves. Fluorescence values were recorded at 520 nm for FITC and 530 nm for luciferin, after exciting at 490 and 327 nm, respectively. The

permeability was then calculated according to *Equation 5*, where V_r is the volume collected from the neuronal chamber, C_f is the final concentration measured from the collected solution, C_i is the initial concentration flowed in, A is area of the membrane (0.2945 cm^2), and t is the time of the experiment.

$$P = \frac{V_r \times C_f}{C_i \times A \times t} \tag{5}$$

Results and Discussion

The development of organotypic models—devices that can simulate one or more organ systems—has revolutionized the study of drug and toxicant exposures. Just as important as the system itself, are the techniques that are used to analyze the output. Here, the effects of downstream electrochemical analysis on quantification of metabolite consumption and production were experimentally determined. The impact of flow rate on the accurate analysis of metabolite concentration was studied. Lastly, changes in the permeability of membranes used within organotypic devices due to differing flow rates and pore sizes were investigated.

The ability to accurately measure cellular uptake within an OoC is essential in identifying changes in cellular metabolism through measurements like glucose and oxygen consumption. Though typically easier to implement, downstream measurement of consumption may result in substantial losses of measured substrate due to diffusion and liquid mixing. To test this, ferricyanide was reduced at -0.2 V vs. Ag/AgCl within an upstream µCA—to simulate consumption with an organ device—with what was left detected downstream at a second µCA. The flux was calculated at the upstream SPE to determine how much ferricyanide was reduced, and from this the amount progressing to the downstream µCA was determined. While the flux in nmol s^{-1} decreased with flow rate, the overall consumption by the SPE increased as the flow rate

decreased—due to the variable treatment times used to reach a steady state (**Table 6.1**). At this point, the concentration losses downstream were from a combination of consumption by the upstream SPE and diffusion of the sample. To separate these variables, the same experiment was performed without the upstream µCA actively consuming ferricyanide. The resulting concentration losses downstream were then only due to diffusion, allowing for a comparison of losses from consumption and diffusion at different flow rates (**Figure 6.2**). As flow rate decreased, concentration losses attributed to consumption and diffusion increased, though not at the same rate. At 200 µL min^{-1}, 35 µM of loss was due to diffusion with only 16 µM consumed by the upstream SPE—an over 2:1 ratio of diffusion to consumption. This ratio improves to 1:1 at 20 µL min^{-1}, with approximately 70 µM lost each to consumption and diffusion. At 2 µL min^{-1}, consumption accounted for a loss of 193 µM while diffusion was only responsible for 92 µM —a ratio of approximately 1:2. Due to this, measurement of cellular consumption is best performed at lower flow rates. Even so, diffusion is responsible for substantial concentration losses at every flow rate. In some cases, the integration of sensors within organotypic devices for *in situ* analysis may be necessary to mitigate the effects of diffusion on the measurement of cellular consumption.

Flow Rate	**200 µL min^{-1}**	**20 µL min^{-1}**	**2 µL min^{-1}**
Mass Transfer (cm s^{-1})	0.0019 ± 0.0001	0.0009 ± 0.0001	0.0003 ± 0.0001
Flux (nmol s^{-1})	0.05 ± 0.01	0.020 ± 0.003	0.008 ± 0.002
Consumption %	3.1 ± 0.2	14 ± 2	51 ± 14
Conc. to Downstream µCA (µM)	485 ± 1	429 ± 10	247 ± 72

Table 6.1. Consumption of Ferricyanide by Upstream SPE. The upstream µCA was used to simulate cellular uptake within an organotypic device through the reduction of ferricyanide. To determine how much was reduced, the mass transfer values for each flow rate were calculated and used to determine the flux in nmol s^{-1}. The flux decreased with decreasing flow rate, though the percentage of ferricyanide consumed increased—from 3% at 200 µL min^{-1} to 51% at 2 µL min^{-1}. The flux values were then used to calculate the concentration of ferricyanide remaining to be measured at the downstream µCA.

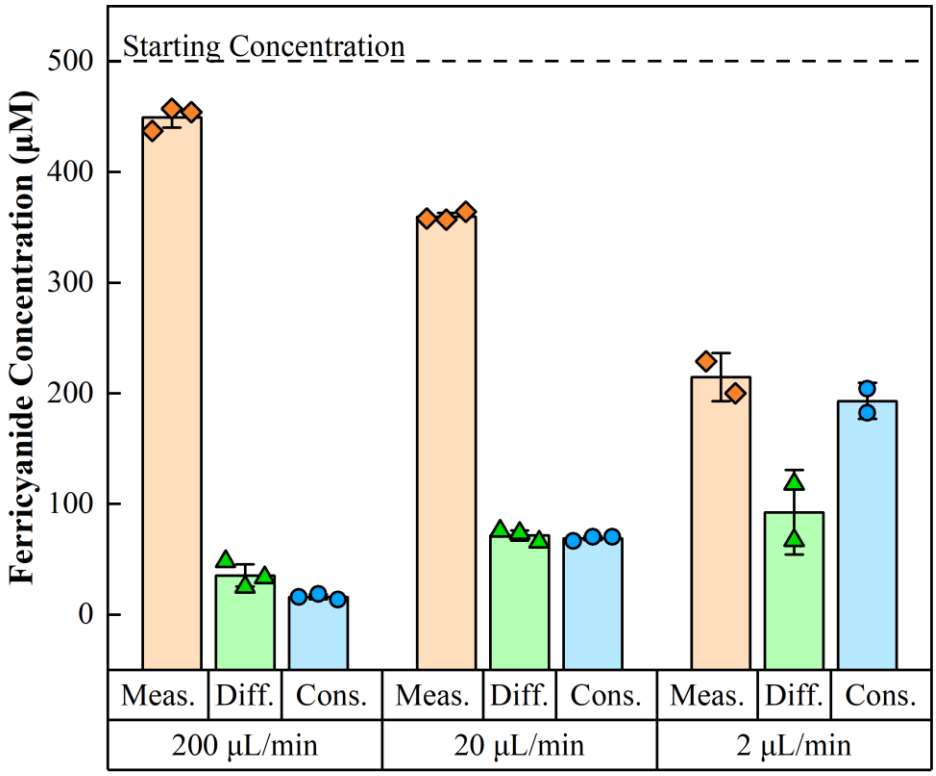

Figure 6.2. Downstream Measurement of the Consumption of Ferricyanide. Consumption of ferricyanide by an upstream SPE was measured downstream at different flow rates to simulate cellular consumption within an organotypic device. When the upstream SPE was disconnected, the loss in concentration downstream was attributed to diffusion. Both consumption and diffusion increased with decreasing flow rates, with consumption increasing at a greater rate. At all flow rates there is a substantial loss in measured concentration due to diffusion. Lower flows rates are best suited for measurement of consumption, and the integration of sensors within the system being studied may mitigate losses due to diffusion.

To simulate metabolite production, the upstream µCA was held at a potential of -0.2 V vs. Ag/AgCl to reduce ferricyanide to ferrocyanide, while the downstream µCA was held at 0.6 V to oxidize the ferrocyanide. The flux from the upstream SPE was calculated to determine the amount of ferrocyanide produced, and therefore the amount to be measured at the downstream µCA (**Table 6.2**). As expected, based on the consumption experiment, the amount of ferrocyanide produced increased as flow rate decreased. The amount of ferrocyanide measured by the downstream µCA also increased with decreasing flow rate (**Figure 6.3**). The difference between the amount produced and the amount measured was attributed as diffusion loss within the system. The concentration difference due to diffusion increased with a decreasing flow rate, from 4 µM being lost at 200 µL min^{-1} to 67 µM at 2 µL min^{-1}. These values can be used to find the ratio between the measured amount and the amount lost to diffusion. At 200 µL min^{-1} this ratio is 2.5:1, followed by 2.1:1 at 2 µL min^{-1}. Because the higher flow rate does not allow the opportunity for high concentrations of metabolites to be produced, a lower flow rate is likely better suited for measuring metabolite production. As with the consumption experiment, diffusion is responsible for a substantial loss in the measured concentration and may be mitigated using *in situ* sensors.

Flow Rate	**200 µL min^{-1}**	**20 µL min^{-1}**	**2 µL min^{-1}**
Mass Transfer (cm s^{-1})	1.6e-3 ± 1e-5	1.1e-3 ± 3e-5	2.5e-4 ± 3e-5
Flux (nmol s^{-1})	4e-2 ± 2e-3	3e-2 ± 7e-4	6.8e-3 ± 9e-5
Total Amount Produced (nmol)	5.17 ± 0.02	8.7 ± 0.2	12.2 ± 0.2
Conc. to Downstream µCA (µM)	12.9 ± 0.1	87 ± 2	203 ± 3

Table 6.2. Production of Ferrocyanide by Upstream SPE. The upstream µCA was used to simulate metabolite production within an organotypic device through the production of ferrocyanide. To determine how much was produced, the mass transfer values for each flow rate were calculated and used to determine the flux in nmol s^{-1}. The flux decreased with decreasing flow rate, though the total amount of ferrocyanide produced increased—from 5 nmoles at 200 µL min^{-1} to 12 nmoles at 2 µL min^{-1}. The flux values were then used to calculate the concentration of ferrocyanide to be measured at the downstream µCA.

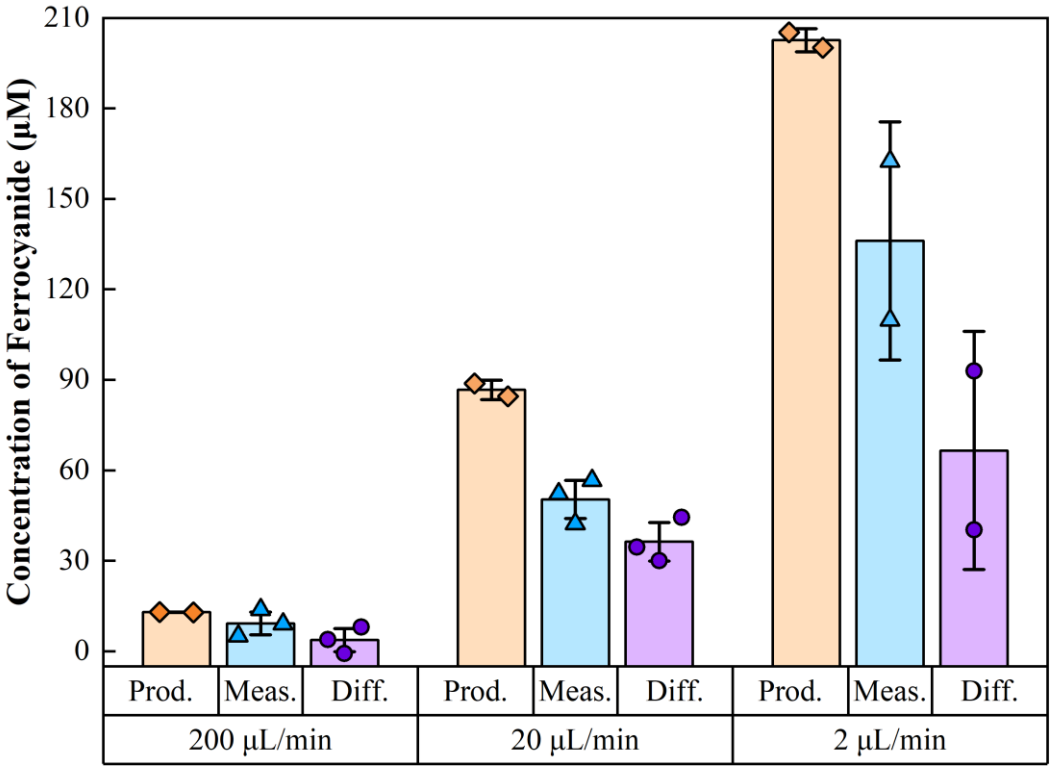

Figure 6.3. Downstream Measurement of the Production of Ferrocyanide. The electrochemical reduction of ferricyanide to ferrocyanide by an upstream SPE was used to simulate metabolite production by cells in an organotypic device. Ferrocyanide was measured by a downstream SPE, with the loss in concentration attributed to diffusion. The production of ferricyanide increased with decreasing flow rate. The amount of ferrocyanide measured, as well how much was lost to diffusion, also increased as flow rate decreased. Lower flow rates allow for greater production of metabolite, though diffusion still substantially effects the measured concentration.

In addition to diffusion and mixing, the open chamber design of the μCA allows for the electrons generated by one electrode to sometimes flow downstream and be detected by another electrode. This can cause issues in analysis and quantification, especially when two electrodes are measuring different analytes. To investigate this, glucose and lactate oxidase enzymes were deposited on specific electrodes, and these electrodes were turned on and off in different configurations to determine the significance of crosstalk between electrodes. These experiments were performed using two different flow profiles (normal and inverted) and at three different flow rates (100, 20, and 10 μL min^{-1}). In the normal flow configuration, crosstalk is most likely to occur from E2 to E1/E3 as E2 is the electrode farthest upstream. To test this, glucose oxidase was deposited onto E2 with lactate oxidase on both E1 and E3. A solution of 5 mM glucose and 500 μM lactate was flowed over the SPE, and the currents measured with different electrode combinations on/off were compared. Overall, E2 had a negligible effect on the current response at E1 regardless of the flow rate, with an increase of only 1.4 ± 0.7% at 10 μL min^{-1} when compared to the response of E1 with E2 off (**Figure 6.4**). Current response at E3, however, was substantially affected by glucose measurement at E2. This effect increased as flow rate decreased, with a 6.8 ± 0.2% increase in signal response at the lowest flow rate of 10 μL min^{-1}. This is likely because E3 is more in line with the flow path of E2 than E1.

In the inverted flow configuration, crosstalk is most likely from E1/E3 to E2—due to E2 being farthest downstream. Here, glucose oxidase was deposited on E1 and E3, while lactate oxidase was deposited on E2. This allowed for the determination of crosstalk from each glucose electrode to the lactate electrode. Overall, E1 had a negligible effect on the current response at E2, with increases of 1 to 2% at every flow rate tested (**Figure 6.5**). Glucose being measured at E3, on the other hand, had a substantial effect on the response measured at E2. Compared to E2 alone, the

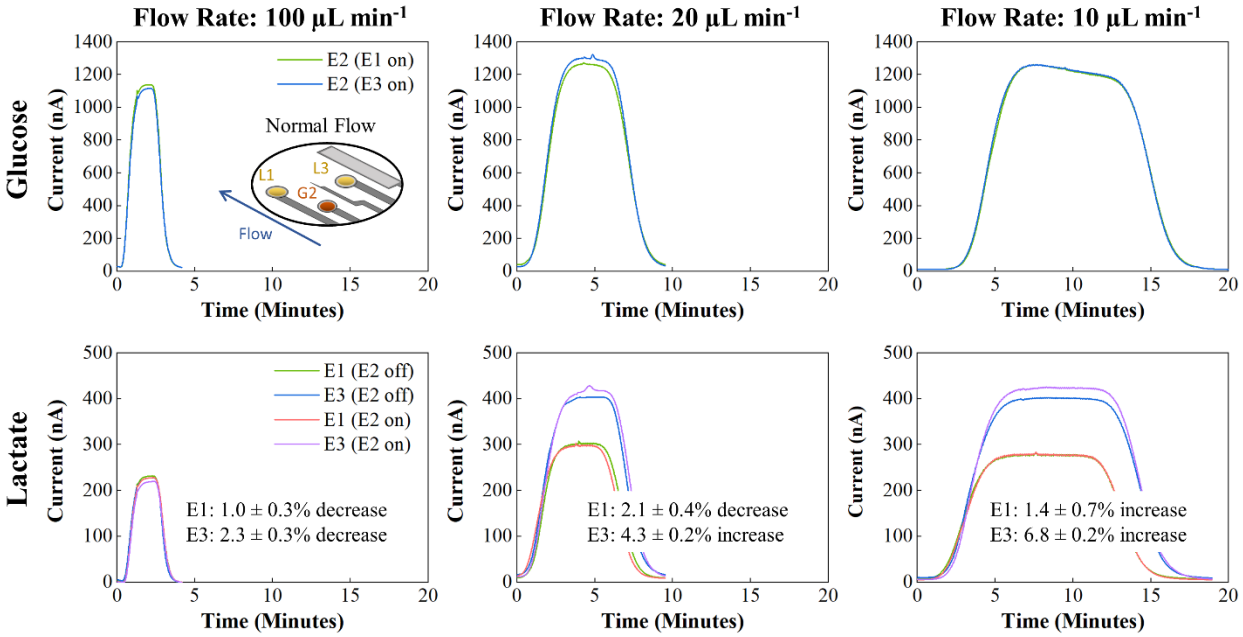

Figure 6.4. Crosstalk Between Electrodes with Normal Flow Configuration. In this configuration, crosstalk is most likely to occur from E2 to the other electrodes. To test this, glucose oxidase was deposited on E2, with lactate oxidase on E1 and E3. The effect of measuring 5 mM glucose at E2 on the current response of E1/E3 measuring 500 µM lactate was then investigated. Overall, glucose measurement at E2 had a negligible effect on E1 current at every flow rate tested. Response at E3, however, was substantially impacted by glucose measurement at E2, especially at lower flow rates—with a 6.8 ± 0.2% increase in current at a flow rate of 10 µL min^{-1}.

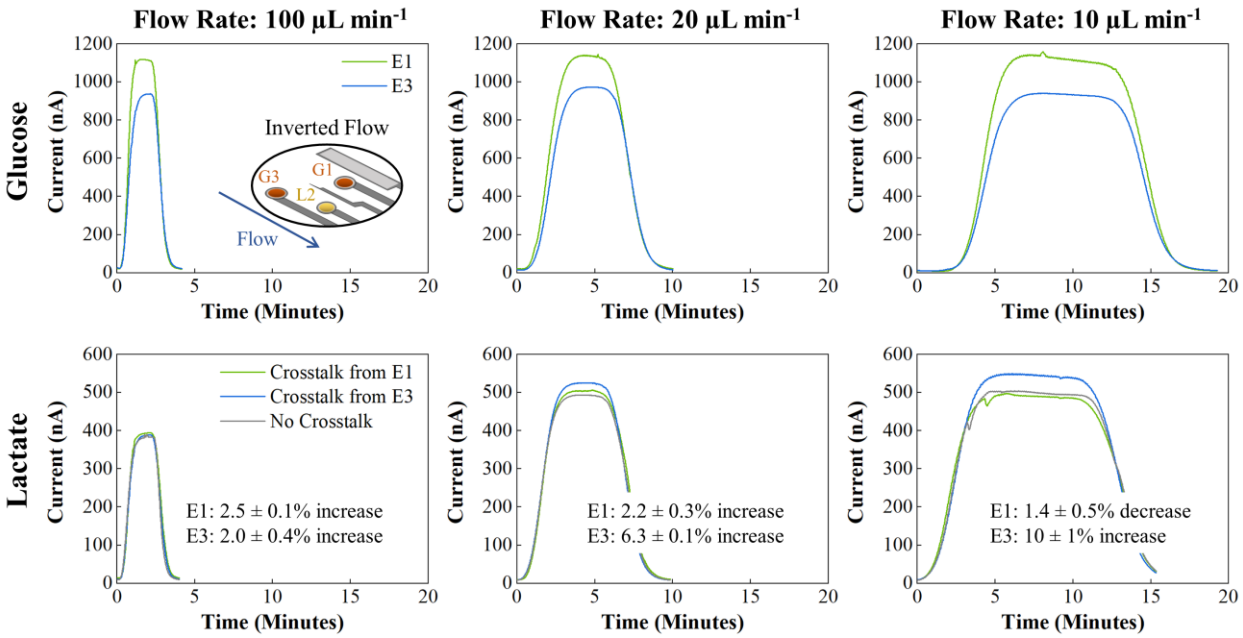

Figure 6.5. Crosstalk Between Electrodes with Inverted Flow Configuration. The flow inlet and outlet were switched from the normal flow configuration. Glucose oxidase was deposited on E1 and E3, with lactate oxidase on E2. The effect of measuring 5 mM glucose at E1/E3 on the current response of E2 measuring 500 µM lactate was then investigated. Overall, glucose measurement at E1 had a negligible effect on E2 current, and no significant change with flow rate. E3, on the other hand, contributed to substantial increases in E2 measured current, especially at lower flow rates—up to a 10 ± 1% increase in current at a flow rate of 10 µL min^{-1}.

current increased 6.3 ± 0.1% at 20 µL min^{-1} and 10 ± 1% at 10 µL min^{-1} when 5 mM glucose was being monitored at E3. Overall, each flow configuration suffers from crosstalk under some circumstances—especially at lower flow rates. These results emphasize the importance of considering enzyme placement during experimental development, especially when monitoring multiple analytes on the same SPE at lower flow rates.

Some OoC devices, like models of the blood-brain barrier and fetal membrane, utilize a semipermeable membrane to mimic the biological structure of their organ.[21,22] Proper function of these devices relies on being able to accurately determine the permeability of the device following cellular exposure to a drug or toxin. Permeability within these devices is affected not only by the pore size of the semipermeable membrane being used, but also by the flow rate of the system. Membranes within organotypic systems can have a range of pore sizes, while the flow rates of the devices can span from submicroliter to milliliters per minute.[20] Two compounds of different sizes—luciferin (300 Da) and FITC-dextran (10 kDa)—were used to investigate the permeability of a Neurovascular Unit, a blood-brain barrier model, with three membrane pore sizes and at three flow rates.[21] Permeability of the membranes generally increased with flow rate and pore size (**Figure 6.6**). With a few exceptions, such as 0.4 µm at 20 µL min^{-1}, there was no substantial differences between permeability with luciferin and FITC-dextran for the given flow rates and pore sizes. Between the two smaller membranes and the 3.0 µm membrane, there was a large increase in the permeability of both compounds. In the case of the NVU, cells are seeded on the membrane and allowed to grow and form a barrier to replicate the blood-brain barrier and its restriction on permeability. If the permeability of the membrane with no cells is too low, breakdown of the created blood-brain barrier will not be reflected in the measured permeability. Therefore, a high permeability—like that seen in the 3.0 µm membrane—is preferred when

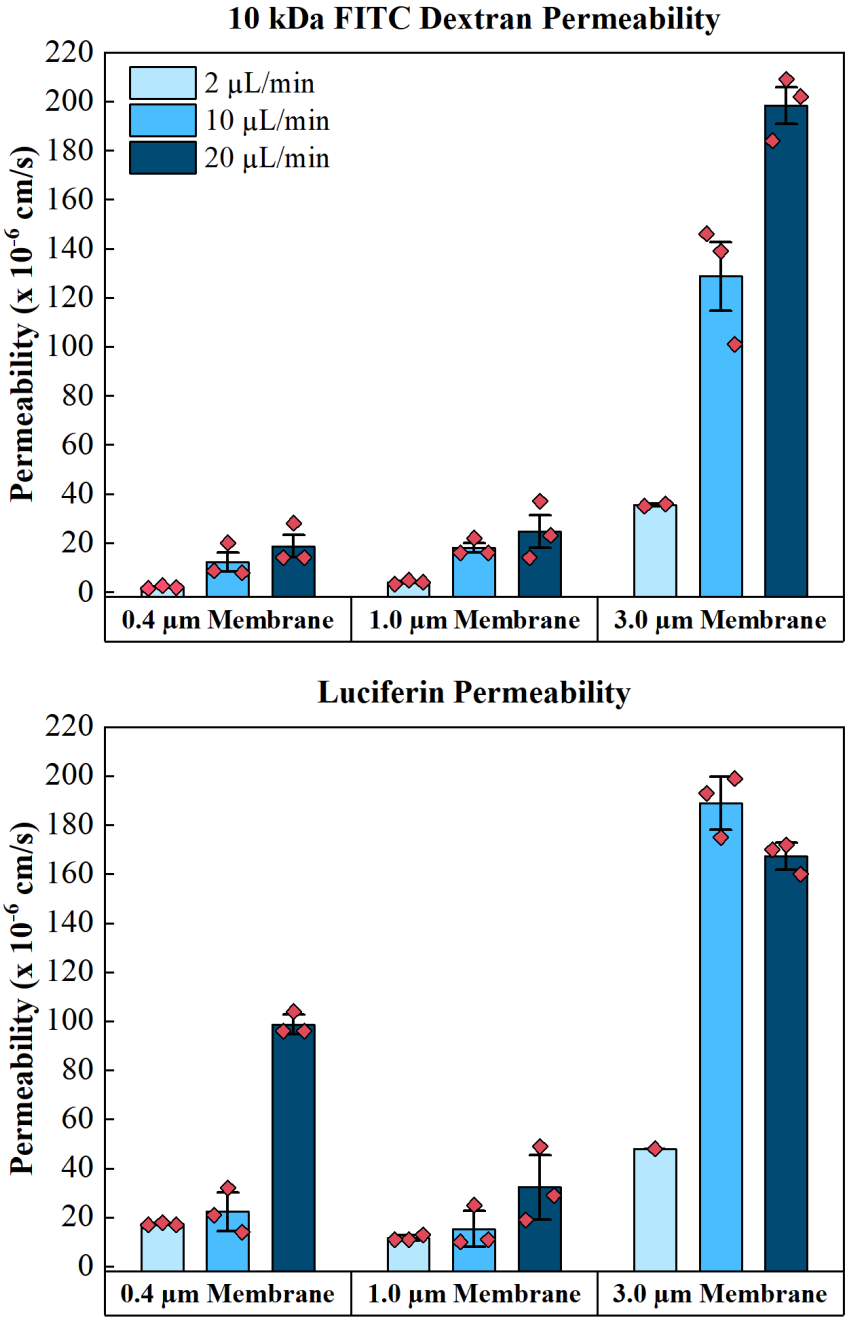

Figure 6.6. Effects of Membrane Pore Size and Flow Rate on NVU Permeability. The permeability of three NVUs with varying pore sizes (0.4, 1.0, and 3.0 µM) were tested at various flow rates (2, 10, and 20 µL min^{-1}) with FITC dextran (MW 10 kDa) and luciferin (MW 280 Da). Except for a few exceptions, such as 0.4 µm at 20 µL min^{-1}, there was no significant difference in permeability between FITC and luciferin. Permeability for both compounds generally increased with increasing flow rate and pore size, though there was a large increase in permeability for all flow rates with the 3.0 um membranes.

performing experiments reliant on permeability measurements. Similarly, as permeability increased with flow rate, higher flow rates are better suited for experiments where permeability plays a role. Overall, a balance should be found between flow rate and permeability. The flow rate must be slow enough to achieve the desired consumption or production of metabolites, while still maintaining an acceptable permeability within the cell-free device.

Conclusions

The ability to accurately identify and quantify changes within OoCs is integral to further understanding the effects of drugs and toxicants on organ systems. While *in situ* detection provides the highest spatial and temporal resolution, downstream analysis of OoCs may provide greater flexibility and consistency in analysis across a variety of OoCs. Downstream quantification of consumption by the upstream µCA was best performed at 2 µL min^{-1} as the concentration consumed was two times greater than the concentration lost to diffusion. Similarly, a flow rate of 2 µL min^{-1} was found to be the optimal rate out of those tested in the analysis of metabolite production. Overall, downstream quantification suffers from inaccuracies due to diffusion when measuring both consumption and production—and depending on the experiment *in situ* sensors may be better suited. In addition, analyte detection at upstream electrodes can have a significant impact on the currents measured downstream—especially at lower flow rates. Crosstalk is greatest between electrodes two and three, with the direction of crosstalk depending on the flow configuration of the µCA. Enzyme placement must therefore be carefully considered when monitoring multiple analytes at flow rates of 20 µL min^{-1} and below. Understanding how membrane permeability changes with flow rate and pore size is essential to proper OoC and experimental design. Finally, the permeability of the NVU was found to increase with flow rate

and pore size, and a large increase in permeability was seen going from 1.0 µm to 3.0 µm membranes. OoC devices with higher flow rates (10 µL min^{-1} and above) and membranes of 3.0 µm pore size may be ideal when studying drugs or toxicants known to affect permeability.

Acknowledgments

This work was supported in part by EPA grant number 83950401-0 and used the resources of the Vanderbilt Microfabrication Core operated by the Vanderbilt Institute for Integrative Biosystems Research and Education. The authors would like to thank Dusty R. Miller and Sara L. Melow for their assistance in measuring NVU permeability.

Chapter VII

CONCLUSIONS AND OUTLOOK

Summary

In this dissertation, the development of enzymatic neurotransmitter sensors and their application towards the investigation of cellular processes and chemical toxicity has been addressed. Previous studies have detailed the development of enzymatic neurotransmitter sensors for glutamate, acetylcholine, adenosine, and dopamine. However, the sensors were limited in their ability to integrate with microfluidic systems, decreasing their suitability for monitoring organ-on-a-chip (OoC) systems. The studies presented here seek to demonstrate the effectiveness of electrochemical biosensors in the analysis of complex biological processes, while also laying the foundation for future work further integrating electrochemical biosensors with OoC systems.

In Chapter III, a glutamate biosensor was characterized and used *in situ* to measure the real-time uptake of glutamate by cells within the microclinical analyzer (μCA). The biosensor demonstrated a quick response time, wide linear range, and long-term stability making it well suited to monitoring glutamate in a variety of biological systems. Using the μCA as a bioreactor, depolarized and glucose-starved PC12 cells were shown to uptake glutamate when exposed to excitotoxic quantities. This platform was then used to study the mechanisms of glutamate uptake in astrocytes with and without Tuberous Sclerosis Complex (TSC)—a disease causing the development of non-cancerous tumors on the brain and other organs. Astrocytes from patients with TSC were shown to uptake less glutamate than the control astrocytes, a possible explanation for

the seizures experienced by many TSC patients. This study demonstrated the use of the μCA and integrated biosensors in the *in-situ* investigation of cellular response.

The use of an enzymatic acetylcholine sensor to analyze the eluate of a chlorpyrifos (CPF) exposed neurovascular unit (NVU) further proved the versatility of electrochemical sensors and the μCA as an analysis platform. The pesticide CPF is known to inhibit acetylcholine breakdown and may alter the integrity of the blood-brain barrier. In Chapter IV, an enzymatic acetylcholine biosensor was characterized in the presence of CPF and used to monitor eluate collected from NVUs exposed to CPF. The biosensor was determined to function properly in up to 50 μM CPF and could be used as a detection method for the toxic metabolite chlorpyrifos oxon (CPO) based upon inhibition of the response—with regeneration of the enzyme demonstrated using 2-pyridine aldoxime methyl chloride. Application of the sensor to the offline analysis of NVU eluate gave insight into the effects of CPF on acetylcholine concentrations of both sides of the BBB. Elevated acetylcholine was detected on both sides of the device, indicating some interaction between CPF and the cells within device. Mass spectrometry of the eluate showed no signs of CPF or its metabolites, suggesting either quick metabolism of the compounds or some alternate pathway of elimination. A substantial amount of CPF was shown to absorb into PDMS over 24 hours—a possible explanation for the lack of some CPF in NVU eluate.

The development of an SPE with 8 working electrodes that could be used with the microformulator pump and valve system provided the opportunity to quantify more analytes than previously possible. A sensor capable of monitoring multiple neurotransmitters could assist in unraveling the complex interaction between neurotransmitters and the investigation of drug and toxicant effects on the brain environment. Chapter V details the development of a neurotransmitter sensor for the simultaneous detection of glutamate, acetylcholine, adenosine, and dopamine.

Because many compounds in the brain—like dopamine and ascorbic acid—are redox active, a permselective mPD layer was applied and its ability to mitigate electrochemical interference was characterized. Even with this mPD layer, high concentrations of dopamine generated significant response on the other electrodes. Correction of this interference was demonstrated through current subtraction based on calibration data. This sensor was then used to quantify the effect of CPF and TBOA on glutamate uptake in astrocytes. TBOA, a glutamate uptake inhibitor, significantly decreased the amount of glutamate taken up by the astrocytes. Treatment with 10 µM CPF, on the other hand, significantly increased the amount of glutamate taken up by the astrocytes—indicating that CPF may have a substantial impact on glutamate metabolism within the brain.

To this point, electrochemical biosensors integrated into the µCA have been used for *in situ* detection in Chapter III, and offline detection in Chapters IV and V. While the biosensors presented here are not well suited to *in situ* detection within an OoC like the NVU, they can be coupled downstream of OoCs for the in-line, real-time analysis of eluate. In Chapter VI, a combination of experimental work and computational modeling was used to determine how downstream analysis affects the accurate quantification of changes within an OoC. The ferricyanide/ferrocyanide redox couple was used to simulate the consumption and production of metabolites, and the effects of diffusion within the microfluidic on downstream analysis were determined. Both consumption and production of metabolites increased with decreasing flow rate—supporting the use of low flow rates when analyzing OoCs downstream. Analyte detection with the µCA was demonstrated to be impacted by crosstalk between certain electrodes—especially at lower flow rates. Crosstalk was greatest between electrodes two and three of the 3-electrode SPE, with the direction of crosstalk depending on the flow configuration of the µCA. Proper placement of enzyme is essential to mitigating crosstalk when monitoring multiple analytes

at flow rates of 20 µL min^{-1} and below. In investigating the permeability of membranes used in OoCs like the NVU, permeability was found to increase with membrane pore size and flow rate. Overall, experimental flow rates must be sufficiently high to obtain adequate membrane permeability within an OoC, but low enough that cells are able to measurably interact with eluate.

Outlook

Neurotransmitters are essential to the proper function of the brain and central nervous system, playing important roles in many biological processes—including behavior and cognition, cardiovascular regulation, and memory. The dysregulation of neurotransmitter signaling has been correlated with the development of neurodegenerative diseases like Alzheimer's and Parkinson's, as well as physical illnesses such as glaucoma and arrythmias.[114] As such, the ability to quantify neurotransmitters is of great importance in identifying mechanisms of disease, monitoring disease progression, and developing therapeutics.

While many methods have been developed for the identification and quantification of neurotransmitters, electrochemical methods provide the opportunity for low cost but rapid detection—making them an attractive option for incorporation into devices used in clinical settings. Enzyme sensors, like those presented within this work, are specific in their detection and relatively low cost compared to other methods of similar specificity. One of the main drawbacks to enzyme sensors is the degradation of the enzyme, resulting in a lower sensitivity and decreasing the lifetime of the sensor. Glutaraldehyde is a common crosslinker used to adsorb enzymes onto electrode surfaces, though its mechanism of crosslinking is not conducive to enzyme stability. More recently, new methods of adsorption have been developed—including sol-gels and covalent binding—that are able to retain a higher level of enzyme activity.[47] Further research into these

methods, as well as the development of new methods that preserve enzyme activity, is essential to improving the effectiveness of enzyme sensors in biological applications.

Additionally, electrochemical detection of neurotransmitters from biological systems—through enzymatic analysis or otherwise—is complicated by interference from prominent electroactive species like ascorbic acid. Many enzyme sensors utilize oxidase enzymes that produce hydrogen peroxide, which is oxidized at a voltage that also oxidizes ascorbic acid and other common interferents. The incorporation of conductive polymers and nanomaterials into enzyme biosensors can lower the potential at which the sensors function, or in some cases change the way the sensors function completely.[115] Biosensors fabricated with these polymers and nanomaterials have been demonstrated to improve the sensitivity and selectivity of the sensors while also effectively mitigating interference. The development of enzymatic sensors with low interference that can maintain response for longer periods of time is necessary before these sensors can be successfully incorporated into *in vitro* microfluidics like OoCs.

The integration of electrochemical sensors either within or downstream of OoC platforms opens the door to investigating biological processes and disease mechanisms in a more controlled and specific way than *in vivo* animal studies. The recapitulation of the full structure and function of the brain has not yet been accomplished, as current technique is too limited to recreate its complex structure. Instead, OoC systems have been developed for individual regions of the brain, including the unidirectional neural network, blood-brain barrier, and spinal cord structure.[116] As OoC systems become more widely available, it is important to consider the methods with which we analyze these devices. As discussed within this work, electrochemical sensors have been integrated both within and downstream of OoC systems. Analysis of eluate from OoC devices is made difficult not just due to interferents like ascorbic acid, but also by the matrices used to

promote proper cell function. Fetal bovine serum is a common additive to cell media, used to promote cell growth. Unfortunately, the high concentrations of proteins in fetal bovine serum complicate analysis by many methods—including electrochemical. While some progress has been made toward the development of alternatives to fetal bovine serum, there are still some unknowns as to how these alternatives alter cellular response within OoCs. The integration of OoCs with electrochemical analysis methods holds much potential, and biosensors should continue to be optimized for use in analyzing OoC systems.

Neurotransmitters are essential to the proper function of the brain and central nervous system. Electrochemical sensors designed to detect these neurotransmitters can provide new knowledge about biological processes and disease mechanisms. Enzyme-based sensors are a low cost but specific analysis method that can be used to detect and quantify multiple neurotransmitters both *in vivo* and *in vitro*. While the stability and sensor response of enzyme sensors can still be improved, the future is bright for the integration of electrochemical sensors with OoCs for the study of neurotransmitters and their functions.

Appendix A

FIBROUS ENCAPSULATION AND THE DELAY OF CONTINUOUS GLUCOSE MONITOR READINGS[3]

Introduction

Readings from continuous glucose monitors (CGMs) have been found to lag blood glucose levels by as much as 20 minutes, with this delay limiting their use as stand-alone glucose monitoring technology.[117] CGMs utilize glucose oxidase, an enzyme that has been demonstrated to turnover glucose on the millisecond time scale, to measure glucose concentration—raising the question as to why CGM readings are so delayed.[118] Substantial efforts have already been made to identify the source of this delay, with the general conclusion being that the physiological latency of interstitial glucose is a major contributor, followed by the smoothing algorithms used by the CGM to filter out noise.[119] This is further supported by microdialysis and lymphatic measurements that indicate significant delay between blood and interstitial glucose concentrations.[120,121]

In contrast to these data, integrative physiology studies suggest that glucose rapidly disperses into the interstitium. The arteriovenous concentration difference of glucose is sizable, with a capillary transit time of 1 to 3 seconds.[122,123] This suggests that blood and interstitial glucose must equilibrate within seconds. Direct measurements of glucose diffusion in human tissues suggest *in vivo* diffusion rates of 100 $\mu m^2\ s^{-1}$, while capillary densities in human adipose tissue and muscle are generally ~200 to 300 capillaries mm^{-2}, corresponding to a diffusion radius of ~70

[3]This appendix contains portions from the published research article McClatchey, P.M.; McClain, E. S.; Williams, I. M.; Malabanan, C. M.; James, F. D.; Lord, P. C.; Gregory, J. M.; Cliffel, D. E.; Wasserman, D. H. *Diabetes* **2019**, *68* (10), 1892–1901.

μm.[124,125] These data then support the equilibration of glucose on the order of seconds rather than minutes.

The results from CGM studies and integrative physiology can be reconciled by considering that CGMs experience a significant foreign body response.[126,127] While this response is generally only considered as a limitation over long-term implantation times, fibrosis and gene expression consistent with hypoxia have been observed within three days of implantation.[128] Foreign body capsules have been shown to slow the diffusion of interstitial solutes, and this has been suggested as an explanation for delaying the arrival of glucose to the CGM microenvironment.[129,130] Even still, the effects of this response during the time frame of typical CGM use is unknown, and it is possible that the high rate of glucose diffusion *in vivo* may render foreign body response negligible in comparison to those caused by smoothing algorithms. Additionally, it is unclear whether these effects take place early enough to influence results from CGMs, which are typically only implanted for two weeks.

In this work, electrochemical and fluorescent detection techniques are used, along with histological analysis, to determine what effects fibrous encapsulation and smoothing algorithms have on CGM readings. Disassembled CGMs are connected to a potentiostat and tested both *in vitro* and *in vivo* to assess the effects of smoothing algorithms on CGM response. A fluorescent glucose analog, 2-NBDG, was used to visualize the dispersion of glucose in the CGM microenvironment, adipose tissue, and skeletal muscle to determine whether the foreign body response plays any role in CGM latency.[131] These experiments will assist in identifying the sources of latency in CGM measurements along with what barriers exist to making CGMs a stand-alone system for monitoring blood glucose.

Experimental

In Vitro Sensor Testing

Disassembled Dexcom G4 CGMs were connected to the CHI 1440 potentiostat (CH Instruments, Austin TX) to monitor sensor response to increasing concentrations of glucose. The disassembly of the CGMs exposed reference and working electrodes that were then connected to the potentiostat using working and reference cables. The potential was held at 0.6 V vs. the reference, and current measurements were recorded once per second. To begin, an electrochemical baseline was set by incubating the CGM in 2 mM PBS (pH 7, Fisher Scientific, Waltham, MA) and 120 mM KCl for five minutes. Following this, the CGM was successively moved to increasing concentrations of glucose, from 5 to 25mM, for five minutes each to reach a steady state. The data was then be analyzed to assess the response of the CGM to increasing concentrations of glucose.

Analysis of CGM Response

A calibration curve was created from the collected electrochemical data by averaging a 30 second portion of the current response at steady state and plotting the averaged currents versus concentration. To further understand sensor response, the approach from one steady-state value to the next was fit to a single exponential decay. The rate of sensor response was calculated by taking the natural logarithm of the difference between steady-state and transient current and plotting it versus time to create a linear response curve. The slope was used in *Equation 6*, where k is the slope, to determine the time that it takes to reach half of the steady-state current, T_{50}. These values could then be compared to those found *in vivo*.

$$T_{50} = \frac{\ln(0.5)}{k} \tag{6}$$

Results and Discussion

Readings from CGMs can lag blood glucose by as much as 20 minutes. In this work, both *in vivo* and *in vitro* experiments were performed to determine the cause of this delayed response. A CGM was disassembled and connected to a potentiostat to monitor the response of the CGM to glucose *in vitro*. The time that it took for the current to reach half of its maximum value, T_{50}, for each glucose concentration was calculated and compared to the response times for *in vivo* CGM and blood glucose readings. A fluorescent glucose analog, 2-NBDG, was also used to assess dispersion within the sensor microenvironment, non-CGM-implanted subcutaneous adipose tissue, and skeletal muscle.

To fully understand the effects of *in vivo* implantation of the response of the CGM, the baseline response of the sensor was tested *in vitro*. Disassembled CGMs were connected to a potentiostat to record the generated current, and the sensors were incubated in increasing concentrations of glucose. The magnitude of current generated increased with increasing glucose concentration up to 25 mM (**Figure A.1, top**), and this response was found to be linear (**Figure A.1, bottom**). Both the linear response and wide working range is expected of a commercial CGM, as the range of 0 to 25 mM glucose covers both physiological and pathophysiological concentrations in humans. This data can also be used to calculate how quickly the sensor reaches a steady-state equilibrium after being introduced to a new concentration of glucose. Upon transitioning the CGM from one concentration to the next, the equilibration of sensor current is well described by a single exponential fit. Taking the natural log of the difference between steady-state and transient current provides a linear curve of which the slope can be used to find the time

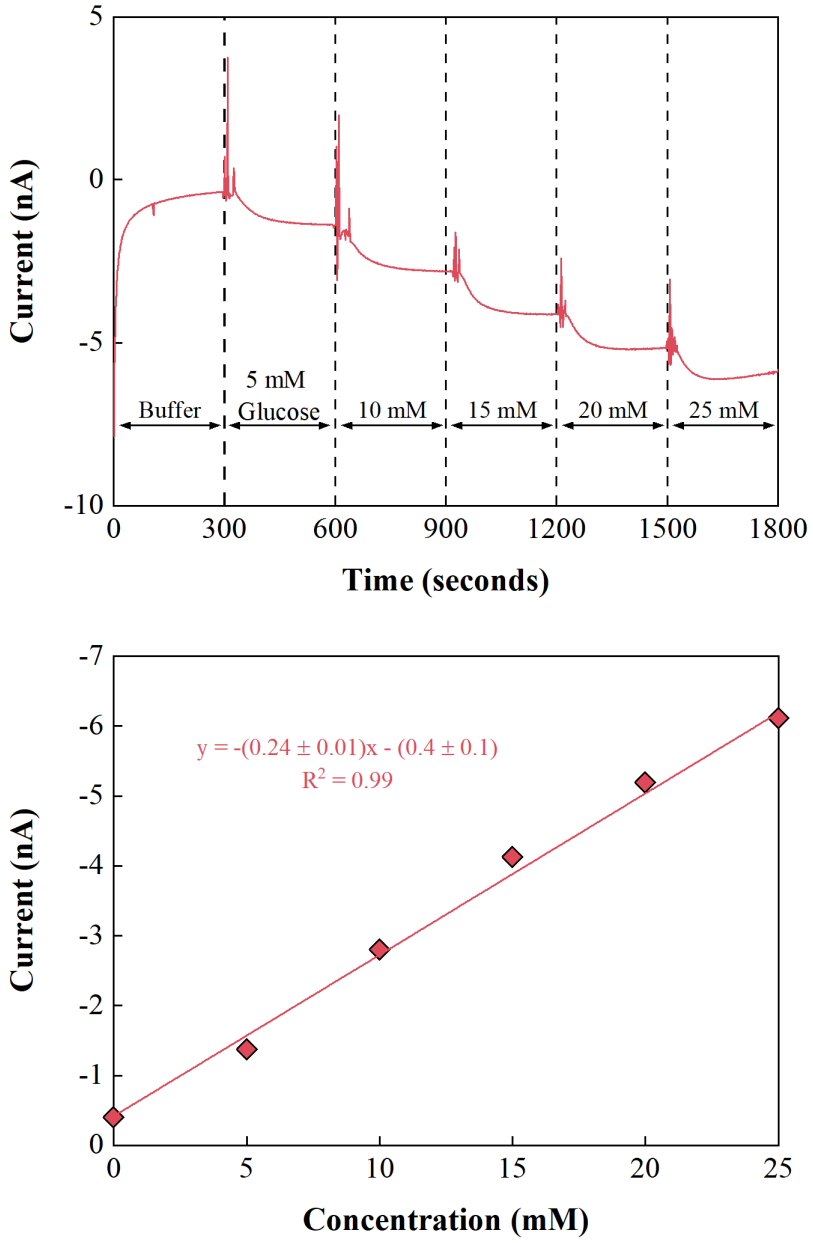

Figure A.1. Electrochemical Data Collected Using Continuous Glucose Monitor. Top) A CGM was incubated in increasing concentrations of glucose for five minutes each, monitored by a potentiostat held at 0.6 V vs. the reference. Current magnitude increased as expected with increasing glucose concentration. Bottom) The CGM was found to have a working range from 0 to 25 mM glucose, spanning the physiological and pathophysiological range of glucose concentration in humans.

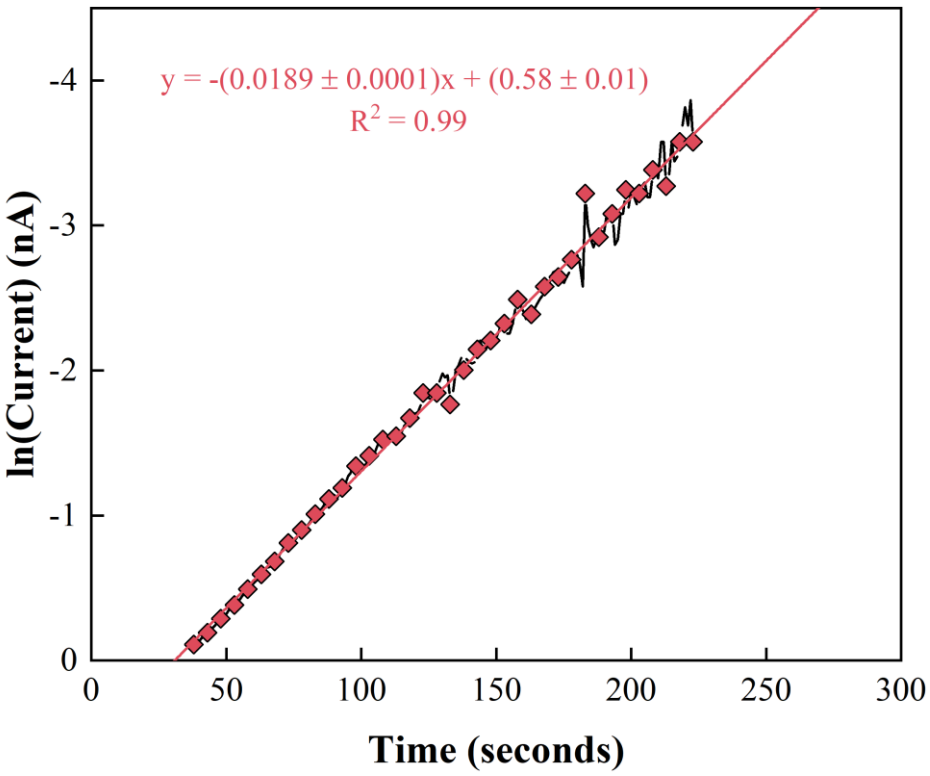

Figure A.2. Natural Logarithm Versus Time Used for T_{50} Calculation. Response of the CGM following incubation in glucose was well suited to a single exponential decay fit. Plotting the logarithm of the difference between steady-state and transient current versus time resulted in a linear curve the slope of which could be used to calculate the T_{50}, or time to half max current. This was done for all glucose concentrations tested.

to half max current, T_{50} (**Figure A.2**). The values for T_{50} decreased with increasing concentration, indicating that the current reached a steady state faster with higher concentrations of glucose (**Table A.1**). The average T_{50} values across all measurements was 29 ± 4 seconds. These T_{50} values indicate that the effects of smoothing algorithms on CGM latency are negligible. *In vitro* T_{50} values can be compared to *in vivo* T_{50} values to assess the effects of implantation on CGM function.

Concentration (mM)	Slope	T_{50}
5	-0.0189	37
10	-0.0193	36
15	-0.0229	30
20	-0.0291	24
25	-0.0382	18

Table A.1. T_{50} Measurements of a Continuous Glucose Monitor *In Vitro*. Plotting the natural logarithm of the difference between steady-state and transient current versus time provided a slope with which the T_{50} could be calculated for each glucose concentration. This value was found to decrease with increasing glucose concentration, meaning that the current reached equilibrium faster as glucose concentration increased.

Following *in vitro* sensor testing, CGMs were implanted in mice and the time to reach maximum current was tested. The time to reach maximum current *in vivo* was found to be 24 ± 7 minutes—much longer than the 2 ± 1 minutes that it took to reach maximum blood glucose levels. A fluorescent blood glucose analog, 2-NBDG, was also used to assess the penetration of glucose within the tissue. The T_{50} of 2-NBDG in the sensor microenvironment was 4 ± 2 minutes, compared to 1 ± 1 minutes in the subcutaneous adipose tissue, and 1.9 ± 0.5 seconds in the skeletal muscle. Histological analysis of the tissue deposited on the CGMs and adipose tissue found that collagen content was closely correlated with the latency in 2-NBDG measurements. Taken together, these

data indicate that fibrous encapsulation of the CGM following implantation is responsible for the slow response time of the sensor as it is more difficult for glucose to penetrate the fibrous tissue.

Conclusions

A CGM was tested both *in vitro* and *in vivo* to determine why CGM readings can be delayed up to 20 minutes relative to blood glucose. *In vitro* testing indicated that the sensor responded relatively quickly upon incubation in glucose, with a time to half max current of 29 ± 4 seconds. With a baseline set, the sensor was implanted in mice and found to take 24 ± 7 minutes to reach maximum current versus 2 ± 1 minutes to maximum blood glucose. Maximum fluorescence of the sensor microenvironment using 2-NBDG was found to significantly lag that of the adipose tissue, with histology of the tissues finding that collagen content was closely correlated with 2-NBDG latency. As evidenced by the *in vitro* measurements, smoothing algorithms have negligible effects on CGM function. The delays in CGM readings following implantation are mostly due to fibrous encapsulation, hindering diffusion of glucose into the sensor region. A CGM that resists this encapsulation would better approximate real-time deviations in blood glucose.

Acknowledgments

The authors would like to thank P. Mason McClatchey for performing, analyzing, and interpreting *in vivo* experiments.

Appendix B

DATA ANALYSIS WITH MATLAB

Below are the five MATLAB files needed to run the data analysis program. Each file can be copied and pasted into MATLAB and saved as its own file. For ease of use, the files can be kept within the same folder. To successfully run the program, only the *data_application.m* file needs to be open within MATLAB.

data_application.m

```
%This script performs data analysis in a variety of ways

menuTitle = 'Choose an option';
menuList = {'Read File', 'Average', 'Standard Deviation', 'Exit Program'};

%Call a function to display a menu and choose data test
choice = datatest(menuTitle, menuList);

%The last menu option is to Exit Program
while choice ~= length (menuList)
   switch choice

      case 1
         %Read in data file
         Data = read_file;
      case 2
         %Find averages of data
         Averages = avg_data (Data);
      case 3
         %Find standard deviations
         Stdevs = stdev_data (Data);
   end
   %Display menu to get next choice from user
   choice = datatest(menuTitle, menuList);
end
```

read_file.m

```
function [ Data ] = read_file

defFilename = 'Enter File Name';
defSheet = '1';
defRange = '';

prompt = {'What is the name of the file you want to load?', ...
        'Which sheet do you want to load?', ...
        'Which columns do you want to load?'};
title = 'Input Data File';
numlines = 1;
defAns = {defFilename, defSheet, defRange};

answer=inputdlg(prompt, title, numlines, defAns);

if (isempty(answer{1}))
   Filename = defFilename;
else
   Filename = answer{1};
end

if (isempty(answer{2}))
   Sheet= defSheet;
else
   Sheet = str2double(answer{2});
   Sheet = floor(Sheet);
   if (Sheet < 0)
      Sheet = defSheet;
   end
end

if (isempty(answer{3}))
   Range= defRange;
else
   Range = answer{3};
end

if (isempty(Range))
   Data = xlsread(Filename, Sheet);
else
   Data = xlsread(Filename, Sheet, Range);
end
end
```

datatest.m

```
function choice = datatest(menuTitle, menuList)
```

```
%datatest prints the menu of options
choice = menu(menuTitle, menuList);

%If user closes menu without selecting option, choice is equal to 0
while choice == 0
   disp('Error - please choose an option')
   choice = menu(menuTitle, menuList);
end
end
```

avg_data.m

```
function [ Averages ] = avg_data ( Data )

% Find size of array
[row, col] = size(Data);

%Determine how often to average

defTime = '120';
prompt = {'How many data points would you like to average?'};
title = 'Average';
numlines = 1;
defAns = {defTime};
answer = inputdlg(prompt, title, numlines, defAns);

if (isempty(answer(1)))
   Time = defTime;
else
   Time = str2double(answer(1));
   Time = floor(Time);
   if (Time < 0)
      Time = defTime;
   end
end

%Number of times to loop through the array
n = floor(row/Time);

%Create array of averaged values
Averages = zeros(n, col);

for iCol = 1:col
   j = 1;
   for iRow = 1:n
      Avg = mean(Data(j:iRow*Time,iCol));
      Averages(iRow,iCol) = Avg;
      j = j+Time;
```

```
    end
end
end
```

stdev_data.m

```
function [ Stdevs ] = stdev_data ( Data )

% Find size of array
[row, col] = size(Data);

%Determine how often to find standard deviation

defTime = '120';
prompt = {'How many data points would you like to find the standard deviation of?'};
title = 'Standard Deviation';
numlines = 1;
defAns = {defTime};
answer = inputdlg(prompt, title, numlines, defAns);

if (isempty(answer(1)))
    Time = defTime;
else
    Time = str2double(answer(1));
    Time = floor(Time);
    if (Time < 0)
        Time = defTime;
    end;
end

%Number of times to loop through the array
n = floor(row/Time);

%Create array of values
Stdevs = zeros(n, col);

for iCol = 1:col
    j = 1;
    for iRow = 1:n
        Stdev = std(Data(j:iRow*Time,iCol));
        Stdevs(iRow,iCol) = Stdev;
        j = j+Time;
    end
end
```

REFERENCES

(1) Takesian, A. E.; Hensch, T. K. Balancing Plasticity/Stability across Brain Development. *Prog. Brain Res.* **2013**, *207*, 3–34.

(2) Zhou, Y.; Danbolt, N. C. Glutamate as a Neurotransmitter in the Healthy Brain. *J. Neural Transm.* **2014**, *121* (8), 799–817.

(3) Ko, J. H.; Strafella, A. P. Dopaminergic Neurotransmission in the Human Brain: New Lessons from Perturbation and Imaging. *Neuroscientist* **2012**, *18* (2), 149–168.

(4) Gottesmann, C. GABA Mechanisms and Sleep. *Neuroscience* **2002**, *111* (2), 231–239.

(5) Stevens, B.; Porta, S.; Haak, L. L.; Gallo, V.; Fields, R. D. Adenosine: A Neuron-Glial Transmitter Promoting Myelination in the CNS in Response to Action Potentials. *Neuron* **2002**, *36* (5), 855–868.

(6) Picciotto, M. R.; Higley, M. J.; Mineur, Y. S. Acetylcholine as a Neuromodulator: Cholinergic Signaling Shapes Nervous System Function and Behavior. *Neuron* **2012**, *76* (1), 116–129.

(7) Calabresi, P.; Picconi, B.; Parnetti, L.; Di Filippo, M. A Convergent Model for Cognitive Dysfunctions in Parkinson's Disease: The Critical Dopamine-Acetylcholine Synaptic Balance. *Lancet Neurol.* **2006**, *5* (11), 974–983.

(8) Venton, B. J.; Wightman, R. M. Psychoanalytical Electrochemistry: Dopamine and Behavior. *Anal. Chem.* **2003**, *75* (19).

(9) Si, B.; Song, E. Recent Advances in the Detection of Neurotransmitters. *Chemosensors* **2018**, *6* (1), 1.

(10) Kennedy, R. T.; Watson, C. J.; Haskins, W. E.; Powell, D. H.; Strecker, R. E. In Vivo Neurochemical Monitoring by Microdialysis and Capillary Separations. *Curr. Opin. Chem.*

Biol. **2002**, *6* (5), 659–665.

(11) Nguyen, M. D.; Venton, B. J. Fast-Scan Cyclic Voltammetry for the Characterization of Rapid Adenosine Release. *Comput. Struct. Biotechnol. J.* **2015**, *13*, 47–54.

(12) Miller, D. R.; McClain, E. S.; Cliffel, D. E. Electrochemical Microphysiometry Detects Cellular Glutamate Uptake. *J. Electrochem. Soc.* **2018**, *165* (12), G3120–G3124.

(13) McClain, E. S.; Miller, D. R.; Cliffel, D. E. Communication—Microfluidic Electrochemical Acetylcholine Detection in the Presence of Chlorpyrifos. *J. Electrochem. Soc.* **2019**, *166* (16), G178–G181.

(14) Florescu, M.; David, M. Tyrosinase-Based Biosensors for Selective Dopamine Detection. *Sensors (Switzerland)* **2017**, *17* (6).

(15) Hinzman, J. M.; Gibson, J. L.; Tackla, R. D.; Costello, M. S.; Burmeister, J. J.; Quintero, J. E.; Gerhardt, G. A.; Hartings, J. A. Real-Time Monitoring of Extracellular Adenosine Using Enzyme-Linked Microelectrode Arrays. *Biosens. Bioelectron.* **2015**, *74*, 512–517.

(16) Lin, Y.; Yu, P.; Mao, L. A Multi-Enzyme Microreactor-Based Online Electrochemical System for Selective and Continuous Monitoring of Acetylcholine. *Analyst* **2015**, *140* (11), 3781–3787.

(17) Mckenzie, J. R.; Cognata, A. C.; Davis, A. N.; Wikswo, J. P.; Cliffel, D. E. Real-Time Monitoring of Cellular Bioenergetics with a Multianalyte Screen-Printed Electrode. *Anal. Chem.* **2015**, *87* (15), 7857–7864.

(18) Benam, K. H.; Mazur, M.; Choe, Y.; Ferrante, T. C.; Novak, R.; Ingber, D. E. Human Lung Small Airway-on-a-Chip Protocol. In *Methods in Molecular Biology*; Humana Press Inc., 2017; Vol. 1612, pp 345–365.

(19) Agarwal, A.; Goss, J. A.; Cho, A.; McCain, M. L.; Parker, K. K. Microfluidic Heart on a

Chip for Higher Throughput Pharmacological Studies. *Lab Chip* **2013**, *13* (18), 3599.

(20) Beckwitt, C. H.; Clark, A. M.; Wheeler, S.; Taylor, D. L.; Stolz, D. B.; Griffith, L.; Wells, A. Liver 'Organ on a Chip.' *Exp. Cell Res.* **2018**, *363* (1), 15–25.

(21) Brown, J. A.; Pensabene, V.; Markov, D. A.; Allwardt, V.; Neely, M. D.; Shi, M.; Britt, C. M.; Hoilett, O. S.; Yang, Q.; Brewer, B. M.; Samson, P. C.; McCawley, L. J.; May, J. M.; Webb, D. J.; Li, D.; Bowman, A. B.; Reiserer, R. S.; Wikswo, J. P. Recreating Blood-Brain Barrier Physiology and Structure on Chip: A Novel Neurovascular Microfluidic Bioreactor. *Biomicrofluidics* **2015**, *9* (5), 054124.

(22) Gnecco, J. S.; Anders, A. P.; Cliffel, D.; Pensabene, V.; Rogers, L. M.; Osteen, K.; Aronoff, D. M. Instrumenting a Fetal Membrane on a Chip as Emerging Technology for Preterm Birth Research. *Curr. Pharm. Des.* **2017**, *23* (40), 6115–6124.

(23) Sosa-Hernández, J. E.; Villalba-Rodríguez, A. M.; Romero-Castillo, K. D.; Aguilar-Aguila-Isaías, M. A.; García-Reyes, I. E.; Hernández-Antonio, A.; Ahmed, I.; Sharma, A.; Parra-Saldívar, R.; Iqbal, H. M. N. Organs-on-a-Chip Module: A Review from the Development and Applications Perspective. *Micromachines* **2018**, *9* (10).

(24) Daneman, R. The Blood-Brain Barrier in Health and Disease. *Ann. Neurol.* **2012**, *72* (5), 648–672.

(25) Liu, S.; Agalliu, D.; Yu, C.; Fisher, M. The Role of Pericytes in Blood-Brain Barrier Function and Stroke. *Curr. Pharm. Des.* **2012**, *18* (25), 3653–3662.

(26) Booth, R.; Kim, H. Characterization of a Microfluidic in Vitro Model of the Blood-Brain Barrier (MBBB). *Lab Chip* **2012**, *12* (10), 1784–1792.

(27) Misun, P. M.; Rothe, J.; Schmid, Y. R. F.; Hierlemann, A.; Frey, O. Multi-Analyte Biosensor Interface for Real-Time Monitoring of 3D Microtissue Spheroids in Hanging-

Drop Networks. *Microsystems Nanoeng.* **2016**, *2* (1), 1–9.

(28) Bavli, D.; Prill, S.; Ezra, E.; Levy, G.; Cohen, M.; Vinken, M.; Vanfleteren, J.; Jaeger, M.; Nahmias, Y. Real-Time Monitoring of Metabolic Function in Liver-Onchip Microdevices Tracks the Dynamics of Mitochondrial Dysfunction. *Proc. Natl. Acad. Sci. U. S. A.* **2016**, *113* (16), E2231–E2240.

(29) DiMario, F. J. Brain Abnormalities in Tuberous Sclerosis Complex. *J. Child Neurol.* **2004**, *19* (9), 650–657.

(30) Pajarillo, E.; Rizor, A.; Lee, J.; Aschner, M.; Lee, E. The Role of Astrocytic Glutamate Transporters GLT-1 and GLAST in Neurological Disorders: Potential Targets for Neurotherapeutics. *Neuropharmacology* **2019**.

(31) Wong, M.; Ess, K. C.; Uhlmann, E. J.; Jansen, L. A.; Li, W.; Crino, P. B.; Mennerick, S.; Yamada, K. A.; Gutmann, D. H. Impaired Glial Glutamate Transport in a Mouse Tuberous Sclerosis Epilepsy Model. *Ann. Neurol.* **2003**, *54* (2), 251–256.

(32) Karanth, S.; Liu, J.; Mirajkar, N.; Pope, C. Effects of Acute Chlorpyrifos Exposure on in Vivo Acetylcholine Accumulation in Rat Striatum. *Toxicol. Appl. Pharmacol.* **2006**, *216* (1), 150–156.

(33) Mileson, B.; Chambers, J. E.; Chen, W. L.; Dettbarn, W.; Ehrich, M.; Eldefrawi, A. T.; Gaylor, D. W.; Hamernik, K.; Hodgson, E.; Karczmar, A. G.; Padilla, S.; Pope, C. N.; Richardson, R. J.; Saunders, D. R.; Sheets, L. P.; Sultatos, L. G.; Wallace, K. B. Common Mechanism of Toxicity: A Case Study of Organophosphorus Pesticides,. *Toxicol. Sci.* **1998**, *41* (1), 8–20.

(34) Picciotto, M. R.; Higley, M. J.; Mineur, Y. S. Acetylcholine as a Neuromodulator: Cholinergic Signaling Shapes Nervous System Function and Behavior. *Neuron* **2012**, *76*

(1), 116–129.

(35) Lewerenz, J.; Maher, P. Chronic Glutamate Toxicity in Neurodegenerative Diseases-What Is the Evidence? *Front. Neurosci.* **2015**, *9* (DEC).

(36) Yu, X.; Kelley, T. J.; Chiel, H. J.; Burgess, J. D. Communication—Microelectrode Detection of Cholesterol Efflux from the Human Buccel Mucosa. *J. Electrochem. Soc.* **2016**, *163* (8), B453–B455.

(37) Defaix, C.; Solgadi, A.; Pham, T. H.; Gardier, A. M.; Chaminade, P.; Tritschler, L. Rapid Analysis of Glutamate, Glutamine and GABA in Mice Frontal Cortex Microdialysis Samples Using HPLC Coupled to Electrospray Tandem Mass Spectrometry. *J. Pharm. Biomed. Anal.* **2018**, *152*, 31–38.

(38) Gray, M.; Meehan, J.; Ward, C.; Langdon, S. P.; Kunkler, I. H.; Murray, A.; Argyle, D. Implantable Biosensors and Their Contribution to the Future of Precision Medicine. *Vet. J.* **2018**, *239*, 21–29.

(39) Theobald, J.; Ghanem, A.; Wallisch, P.; Banaeiyan, A. A.; Andrade-Navarro, M. A.; Taškova, K.; Haltmeier, M.; Kurtz, A.; Becker, H.; Reuter, S.; Mrowka, R.; Cheng, X.; Wölfl, S. Liver-Kidney-on-Chip To Study Toxicity of Drug Metabolites. *ACS Biomater. Sci. Eng.* **2018**, *4* (1), 78–89.

(40) Vernetti, L.; Gough, A.; Baetz, N.; Blutt, S.; Broughman, J. R.; Brown, J. A.; Foulke-Abel, J.; Hasan, N.; In, J.; Kelly, E.; Kovbasnjuk, O.; Repper, J.; Senutovitch, N.; Stabb, J.; Yeung, C.; Zachos, N. C.; Donowitz, M.; Estes, M.; Himmelfarb, J.; Truskey, G.; Wikswo, J. P.; Taylor, D. L. Functional Coupling of Human Microphysiology Systems: Intestine, Liver, Kidney Proximal Tubule, Blood-Brain Barrier and Skeletal Muscle. *Sci. Rep.* **2017**, *7*, 42296.

(41) Gnecco, J. S.; Anders, A. P.; Cliffel, D.; Pensabene, V.; Rogers, L. M.; Osteen, K.; Aronoff, D. M. Instrumenting a Fetal Membrane on a Chip as Emerging Technology for Preterm Birth Research. *Curr. Pharm. Des.* **2018**, *23* (40), 6115–6124.

(42) Curatolo, P.; Verdecchia, M.; Bombardieri, R. Tuberous Sclerosis Complex: A Review of Neurological Aspects. *Eur. J. Paediatr. Neurol.* **2002**, *6* (1), 15–23.

(43) Pajarillo, E.; Rizor, A.; Lee, J.; Aschner, M.; Lee, E. The Role of Astrocytic Glutamate Transporters GLT-1 and GLAST in Neurological Disorders: Potential Targets for Neurotherapeutics. *Neuropharmacology* **2019**, *161*.

(44) Neely, M. D.; Davison, C. A.; Aschner, M.; Bowman, A. B. From the Cover: Manganese and Rotenone-Induced Oxidative Stress Signatures Differ in IPSC-Derived Human Dopamine Neurons. *Toxicol. Sci.* **2017**, *159* (2), 366–379.

(45) Hinzman, J. M.; Thomas, T. C.; Burmeister, J. J.; Quintero, J. E.; Huettl, P.; Pomerleau, F.; Gerhardt, G. A.; Lifshitz, J. Diffuse Brain Injury Elevates Tonic Glutamate Levels and Potassium-Evoked Glutamate Release in Discrete Brain Regions at Two Days Post-Injury: An Enzyme-Based Microelectrode Array Study. *J. Neurotrauma* **2010**, *27* (5), 889–899.

(46) Jamal, M.; Chakrabarty, S.; Yousuf, M. A.; Khosla, A.; Razeeb, K. M. Micro and Nanostructure Based Electrochemical Sensor Platform for Glutamate Detection. *Microsyst. Technol.* **2018**, 1–14.

(47) Rocchitta, G.; Spanu, A.; Babudieri, S.; Latte, G.; Madeddu, G.; Galleri, G.; Nuvoli, S.; Bagella, P.; Demartis, M.; Fiore, V.; Manetti, R.; Serra, P. Enzyme Biosensors for Biomedical Applications: Strategies for Safeguarding Analytical Performances in Biological Fluids. *Sensors* **2016**, *16* (6), 780.

(48) Warr, O.; Takahashi, M.; Attwell, D. Modulation of Extracellular Glutamate Concentration

in Rat Brain Slices by Cystine-Glutamate Exchange. *J. Physiol.* **1999**, *514 (Pt 3* (Pt 3), 783–793.

(49) Meldrum, B. S. Glutamate as a Neurotransmitter in the Brain: Review of Physiology and Pathology. *J. Nutr.* **2000**, *130* (4), 1007S-1015S.

(50) Bäcker, M.; Rakowski, D.; Poghossian, A.; Biselli, M.; Wagner, P.; Schöning, M. J. Chip-Based Amperometric Enzyme Sensor System for Monitoring of Bioprocesses by Flow-Injection Analysis. *J. Biotechnol.* **2013**, *163* (4), 371–376.

(51) Wikswo, J. P.; Block, F. E.; Cliffel, D. E.; Goodwin, C. R.; Marasco, C. C.; Markov, D. A.; McLean, D. L.; McLean, J. A.; McKenzie, J. R.; Reiserer, R. S.; Samson, P. C.; Schaffer, D. K.; Seale, K. T.; Sherrod, S. D. Engineering Challenges for Instrumenting and Controlling Integrated Organ-on-Chip Systems. *IEEE Trans. Biomed. Eng.* **2013**, *60* (3), 682–690.

(52) Garcia-Polite, F.; Martorell, J.; Del Rey-Puech, P.; Melgar-Lesmes, P.; O'Brien, C. C.; Roquer, J.; Ois, A.; Principe, A.; Edelman, E. R.; Balcells, M. Pulsatility and High Shear Stress Deteriorate Barrier Phenotype in Brain Microvascular Endothelium. *J. Cereb. Blood Flow Metab.* **2017**, *37* (7), 2614–2625.

(53) Bellocchio, E. E.; Reimer, R. J.; Fremeau, R. T.; Edwards, R. H. Uptake of Glutamate into Synaptic Vesicles by an Inorganic Phosphate Transporter. *Science* **2000**, *289* (5481), 957–960.

(54) Swanson, R. A.; Liu, J.; Miller, J. W.; Rothstein, J. D.; Farrell, K.; Stein, B. A.; Longuemare, M. C. Neuronal Regulation of Glutamate Transporter Subtype Expression in Astrocytes. *J. Neurosci.* **1997**, *17* (3), 932–940.

(55) Ragnarsdottir, K. V. Environmental Fate and Toxicology of Organophosphate Pesticides.

J. Geol. Soc. London. **2000**, *157* (4), 859–876.

(56) Atwood, D.; Paisley-Jones, C. *Pesticides Industry Sales and Usage*; 2017.

(57) Rauh, V.; Arunajadai, S.; Horton, M.; Perera, F.; Hoepner, L.; Barr, D. B.; Whyatt, R. Seven-Year Neurodevelopmental Scores and Prenatal Exposure to Chlorpyrifos, a Common Agricultural Pesticide. *Environ. Health Perspect.* **2011**, *119* (8), 1196–1201.

(58) Rauh, V. A.; Perera, F. P.; Horton, M. K.; Whyatt, R. M.; Bansal, R.; Hao, X.; Liu, J.; Barr, D. B.; Slotkin, T. A.; Peterson, B. S. Brain Anomalies in Children Exposed Prenatally to a Common Organophosphate Pesticide. *Proc. Natl. Acad. Sci.* **2012**, *109* (20), 7871–7876.

(59) Prendergast, M. A.; Terry, A. V; Buccafusco, J. J. Effects of Chronic, Low-Level Organophosphate Exposure on Delayed Recall, Discrimination, and Spatial Learning in Monkeys and Rats. *Neurotoxicol. Teratol.* **1998**, *20* (2), 115–122.

(60) Taylor, P.; Brown, J. H. *Synthesis, Storage and Release of Acetylcholine*; Lippincott-Raven, 1999.

(61) Sánchez-Santed, F.; Colomina, M. T.; Herrero Hernández, E. Organophosphate Pesticide Exposure and Neurodegeneration. *Cortex* **2016**, *74*, 417–426.

(62) Eaton, D. L.; Daroff, R. B.; Autrup, H.; Bridges, J.; Buffler, P.; Costa, L. G.; Coyle, J.; McKhann, G.; Mobley, W. C.; Nadel, L.; Neubert, D.; Schulte-Hermann, R.; Spencer, P. S. Review of the Toxicology of Chlorpyrifos With an Emphasis on Human Exposure and Neurodevelopment. *Crit. Rev. Toxicol.* **2008**, *38* (sup2), 1–125.

(63) Garabrant, D. H.; Aylward, L. L.; Berent, S.; Chen, Q.; Timchalk, C.; Burns, C. J.; Hays, S. M.; Albers, J. W. Cholinesterase Inhibition in Chlorpyrifos Workers: Characterization of Biomarkers of Exposure and Response in Relation to Urinary TCPy. *J. Expo. Sci. Environ. Epidemiol.* **2009**, *19* (7), 634–642.

(64) Akhtar, M. H.; Hussain, K. K.; Gurudatt, N. G.; Shim, Y.-B. Detection of Ca2+-Induced Acetylcholine Released from Leukemic T-Cells Using an Amperometric Microfluidic Sensor. *Biosens. Bioelectron.* **2017**, *98*, 364–370.

(65) Keighron, J. D.; Wigström, J.; Kurczy, M. E.; Bergman, J.; Wang, Y.; Cans, A.-S. Amperometric Detection of Single Vesicle Acetylcholine Release Events from an Artificial Cell. *ACS Chem. Neurosci.* **2015**, *6* (1), 181–188.

(66) Pohanka, M. Electrochemical Biosensors Based on Acetylcholinesterase and Butyrylcholinesterase. A Review. *Int. J. Electrochem. Sci* **2016**, *11*, 7440–7452.

(67) Hutson, M. S.; Alexander, P. G.; Allwardt, V.; Aronoff, D. M.; Bruner-Tran, K. L.; Cliffel, D. E.; Davidson, J. M.; Gough, A.; Markov, D. A.; McCawley, L. J.; McKenzie, J. R.; McLean, J. A.; Osteen, K. G.; Pensabene, V.; Samson, P. C.; Senutovitch, N. K.; Sherrod, S. D.; Shotwell, M. S.; Taylor, D. L.; Tetz, L. M.; Tuan, R. S.; Vernetti, L. A.; Wikswo, J. P. Organs-on-Chips as Bridges for Predictive Toxicology. *Appl. Vitr. Toxicol.* **2016**, *2* (2), 97–102.

(68) Helms, H. C.; Abbott, N. J.; Burek, M.; Cecchelli, R.; Couraud, P.-O.; Deli, M. A.; Förster, C.; Galla, H. J.; Romero, I. A.; Shusta, E. V; Stebbins, M. J.; Vandenhaute, E.; Weksler, B.; Brodin, B. In Vitro Models of the Blood–Brain Barrier: An Overview of Commonly Used Brain Endothelial Cell Culture Models and Guidelines for Their Use. *J. Cereb. Blood Flow Metab.* **2016**, *36* (5), 862–890.

(69) Parran, D. K.; Magnin, G.; Li, W.; Jortner, B. S.; Ehrich, M. Chlorpyrifos Alters Functional Integrity and Structure of an In Vitro BBB Model: Co-Cultures of Bovine Endothelial Cells and Neonatal Rat Astrocytes. *Neurotoxicology* **2005**, *26* (1), 77–88.

(70) Voorhees, J. R.; Rohlman, D. S.; Lein, P. J.; Pieper, A. A. Neurotoxicity in Preclinical

Models of Occupational Exposure to Organophosphorus Compounds. *Front. Neurosci.* **2017**, *10* (Jan).

(71) Prabhakarpandian, B.; Shen, M.-C.; Nichols, J. B.; Mills, I. R.; Sidoryk-Wegrzynowicz, M.; Aschner, M.; Pant, K. SyM-BBB: A Microfluidic Blood Brain Barrier Model. *Lab Chip* **2013**, *13* (6), 1093.

(72) Griep, L. M.; Wolbers, F.; de Wagenaar, B.; ter Braak, P. M.; Weksler, B. B.; Romero, I. A.; Couraud, P. O.; Vermes, I.; van der Meer, A. D.; van den Berg, A. BBB ON CHIP: Microfluidic Platform to Mechanically and Biochemically Modulate Blood-Brain Barrier Function. *Biomed. Microdevices* **2013**, *15* (1), 145–150.

(73) Balbuena, P.; Li, W.; Magnin-Bissel, G.; Meldrum, J. B.; Ehrich, M. Comparison of Two Blood-Brain Barrier in Vitro Systems: Cytotoxicity and Transfer Assessments of Malathion/Oxon and Lead Acetate. *Toxicol. Sci.* **2010**, *114* (2), 260–271.

(74) Brown, J. A.; Codreanu, S. G.; Shi, M.; Sherrod, S. D.; Markov, D. A.; Neely, M. D.; Britt, C. M.; Hoilett, O. S.; Reiserer, R. S.; Samson, P. C.; McCawley, L. J.; Webb, D. J.; Bowman, A. B.; McLean, J. A.; Wikswo, J. P. Metabolic Consequences of Inflammatory Disruption of the Blood-Brain Barrier in an Organ-on-Chip Model of the Human Neurovascular Unit. *J. Neuroinflammation* **2016**, *13* (1), 306.

(75) Auner, A. W.; Tasneem, K. M.; Markov, D. A.; McCawley, L. J.; Hutson, M. S. Chemical-PDMS Binding Kinetics and Implications for Bioavailability in Microfluidic Devices. *Lab Chip* **2019**, *19* (5), 864–874.

(76) Chen, D.; Jiao, Y.; Jia, H.; Guo, Y.; Sun, X.; Wang, X.; Xu, J. Acetylcholinesterase Biosensor for Chlorpyrifos Detection Based on Multi-Walled Carbon Nanotubes-SnO2-Chitosan Nanocomposite Modified Screen-Printed Electrode. *Int. J. Electrochem. Sci.*

2015, *10* (12), 10491–10501.

(77) Pohanka, M.; Karasova, J. Z.; Kuca, K.; Pikula, J.; Holas, O.; Korabecny, J.; Cabal, J. Colorimetric Dipstick for Assay of Organophosphate Pesticides and Nerve Agents Represented by Paraoxon, Sarin and VX. *Talanta* **2010**, *81* (1–2), 621–624.

(78) Buxton, D. A.; Brimlecombe, R. W.; French, M. C.; Redfern, P. H. Brain Acetylcholine Concentration and Acetylcholinesterase Activity in Selectively-Bred Strains of Rats. *Psychopharmacology (Berl).* **1976**, *47* (1), 97–99.

(79) Environmental Protection Agency. *2018 Edition of the Drinking Water Standards and Health Advisories Tables (EPA 822-F-18-001)*; 2018.

(80) Lee, H. S.; Kim, Y. A.; Cho, Y. A.; Lee, Y. T. Oxidation of Organophosphorus Pesticides for the Sensitive Detection by a Cholinesterase-Based Biosensor. *Chemosphere* **2002**, *46* (4), 571–576.

(81) Mulchandani, P.; Wilfred, C.; Mulchandani, A. Flow Injection Amperometric Enzyme Biosensor for Direct Determination of Organophosphate Nerve Agents. *Environ. Sci. Technol.* **2001**, *35* (12), 2562–2565.

(82) Kaur, N.; Thakur, H.; Kumar, R.; Prabhakar, N. An Electrochemical Sensor Modified with Poly(3,4-Ethylenedioxythiophene)-Wrapped Multi-Walled Carbon Nanotubes for Enzyme Inhibition-Based Determination of Organophosphates. *Microchim. Acta* **2016**, *183* (7), 2307–2315.

(83) Arduini, F.; Cinti, S.; Scognamiglio, V.; Moscone, D. Nanomaterials in Electrochemical Biosensors for Pesticide Detection: Advances and Challenges in Food Analysis. *Microchim. Acta* **2016**, *183* (7), 2063–2083.

(84) Eddleston, M.; Eyer, P.; Worek, F.; Juszczak, E.; Alder, N.; Mohamed, F.; Senarathna, L.;

Hittarage, A.; Azher, S.; Jeganathan, K.; Jayamanne, S.; von Meyer, L.; Dawson, A. H.; Sheriff, M. H. R.; Buckley, N. A. Pralidoxime in Acute Organophosphorus Insecticide Poisoning—A Randomised Controlled Trial. *PLoS Med.* **2009**, *6* (6), e1000104.

(85) Luo, C.; Tong, M.; Maxwell, D. M.; Saxena, A. Comparison of Oxime Reactivation and Aging of Nerve Agent-Inhibited Monkey and Human Acetylcholinesterases. *Chem. Biol. Interact.* **2008**, *175* (1–3), 261–266.

(86) Jokanović, M.; Prostran, M. Pyridinium Oximes as Cholinesterase Reactivators. Structure-Activity Relationship and Efficacy in the Treatment of Poisoning with Organophosphorus Compounds. *Curr. Med. Chem.* **2009**, *16* (17), 2177–2188.

(87) Childs, A. F.; Davies, D. R.; Green, A. L.; Rutland, J. P. The Reactivation by Oximes and Hydroxamic Acids of Cholinesterase Inhibited by Organo-Phosphorus Compounds. *Br. J. Pharmacol. Chemother.* **1955**, *10* (4), 462–465.

(88) Li, W.; Ehrich, M. Transient Alterations of the Blood-Brain Barrier Tight Junction and Receptor Potential Channel Gene Expression by Chlorpyrifos. *J. Appl. Toxicol.* **2013**, *33* (10), 1187–1191.

(89) Levin, E. D.; Addy, N.; Nakajima, A.; Christopher, N. C.; Seidler, F. J.; Slotkin, T. A. Persistent Behavioral Consequences of Neonatal Chlorpyrifos Exposure in Rats. *Dev. Brain Res.* **2001**, *130* (1), 83–89.

(90) Timchalk, C.; Poet, T. S.; Hinman, M. N.; Busby, A. L.; Kousba, A. A. Pharmacokinetic and Pharmacodynamic Interaction for a Binary Mixture of Chlorpyrifos and Diazinon in the Rat. *Toxicol. Appl. Pharmacol.* **2005**, *205* (1), 31–42.

(91) Atabila, A.; Phung, D. T.; Sadler, R.; Connell, D.; Chu, C. Comparative Evaluation of Chlorpyrifos Exposure Estimates from Whole-Body Dermal Dosimetry and Urinary

Trichloro-2-Pyridinol (TCP) Methods. *Ecotoxicol. Environ. Saf.* **2019**, *172*, 439–443.

(92) Toepke, M. W.; Beebe, D. J. PDMS Absorption of Small Molecules and Consequences in Microfluidic Applications. *Lab Chip* **2006**, *6* (12), 1484–1486.

(93) Bjorness, T.; Greene, R. Adenosine and Sleep. *Curr. Neuropharmacol.* **2009**, *7* (3), 238–245.

(94) Torres-Altoro, M. I.; Mathur, B. N.; Drerup, J. M.; Thomas, R.; Lovinger, D. M.; O'Callaghan, J. P.; Bibb, J. A. Organophosphates Dysregulate Dopamine Signaling, Glutamatergic Neurotransmission, and Induce Neuronal Injury Markers in Striatum. *J. Neurochem.* **2011**, *119* (2), 303–313.

(95) Rush, T.; Liu, X. Q.; Hjelmhaug, J.; Lobner, D. Mechanisms of Chlorpyrifos and Diazinon Induced Neurotoxicity in Cortical Culture. *Neuroscience* **2010**, *166* (3), 899–906.

(96) Dong, X. X.; Wang, Y.; Qin, Z. H. Molecular Mechanisms of Excitotoxicity and Their Relevance to Pathogenesis of Neurodegenerative Diseases. *Acta Pharmacol. Sin.* **2009**, *30* (4), 379–387.

(97) Rose, C. R.; Felix, L.; Zeug, A.; Dietrich, D.; Reiner, A.; Henneberger, C. Astroglial Glutamate Signaling and Uptake in the Hippocampus. *Front. Mol. Neurosci.* **2018**, *10*, 451.

(98) Soldatkina, O. V.; Kucherenko, I. S.; Pyeshkova, V. M.; Alekseev, S. A.; Soldatkin, O. O.; Dzyadevych, S. V. Improvement of Amperometric Transducer Selectivity Using Nanosized Phenylenediamine Films. *Nanoscale Res. Lett.* **2017**, *12*.

(99) Hamdi, N.; Wang, J.; Monbouquette, H. G. Polymer Films as Permselective Coatings for H2O 2-Sensing Electrodes. *J. Electroanal. Chem.* **2005**, *581* (2), 258–264.

(100) Haskó, G.; Pacher, P.; Vizi, E. S.; Illes, P. Adenosine Receptor Signaling in the Brain Immune System. *Trends Pharmacol. Sci.* **2005**, *26* (10), 511–516.

(101) Owesson-White, C. A.; Roitman, M. F.; Sombers, L. A.; Belle, A. M.; Keithley, R. B.; Peele, J. L.; Carelli, R. M.; Wightman, R. M. Sources Contributing to the Average Extracellular Concentration of Dopamine in the Nucleus Accumbens. *J. Neurochem.* **2012**, *121* (2), 252–262.

(102) Zeng, C.; Jose, P. A. Dopamine Receptors: Important Antihypertensive Counterbalance against Hypertensive Factors. *Hypertension* **2011**, *57* (1), 11–17.

(103) Anderson, C. M.; Bridges, R. J.; Chamberlin, A. R.; Shimamoto, K.; Yasuda-Kamatani, Y.; Swanson, R. A. Differing Effects of Substrate and Non-Substrate Transport Inhibitors on Glutamate Uptake Reversal. *J. Neurochem.* **2002**, *79* (6), 1207–1216.

(104) Huh, D.; Matthews, B. D.; Mammoto, A.; Montoya-Zavala, M.; Yuan Hsin, H.; Ingber, D. E. Reconstituting Organ-Level Lung Functions on a Chip. *Science (80-.).* **2010**, *328* (5986), 1662–1668.

(105) Grosberg, A.; Alford, P. W.; McCain, M. L.; Parker, K. K. Ensembles of Engineered Cardiac Tissues for Physiological and Pharmacological Study: Heart on a Chip. *Lab Chip* **2011**, *11* (24), 4165–4173.

(106) Zhao, Y.; Kankala, R. K.; Wang, S. Bin; Chen, A. Z. Multi-Organs-on-Chips: Towards Long-Term Biomedical Investigations. *Molecules* **2019**, *24* (4).

(107) Shanks, N.; Greek, R.; Greek, J. Are Animal Models Predictive for Humans? *Philos. Ethics, Humanit. Med.* **2009**, *4* (1), 2.

(108) Ramme, A. P.; Koenig, L.; Hasenberg, T.; Schwenk, C.; Magauer, C.; Faust, D.; Lorenz, A. K.; Krebs, A. C.; Drewell, C.; Schirrmann, K.; Vladetic, A.; Lin, G. C.; Pabinger, S.; Neuhaus, W.; Bois, F.; Lauster, R.; Marx, U.; Dehne, E. M. Autologous Induced Pluripotent Stem Cell-Derived Four-Organ-Chip. *Futur. Sci. OA* **2019**, *5* (8).

(109) Santbergen, M. J. C.; van der Zande, M.; Bouwmeester, H.; Nielen, M. W. F. Online and in Situ Analysis of Organs-on-a-Chip. *TrAC - Trends Anal. Chem.* **2019**, *115*, 138–146.

(110) Eklund, S. E.; Snider, R. M.; Wikswo, J.; Baudenbacher, F.; Prokop, A.; Cliffel, D. E. Multianalyte Microphysiometry as a Tool in Metabolomics and Systems Biology. *J. Electroanal. Chem.* **2006**, *587* (2), 333–339.

(111) McKenzie, J. R.; Palubinsky, A. M.; Brown, J. E.; McLaughlin, B.; Cliffel, D. E. Metabolic Multianalyte Microphysiometry Reveals Extracellular Acidosis Is an Essential Mediator of Neuronal Preconditioning. *ACS Chem. Neurosci.* **2012**, *3* (7), 510–518.

(112) Mao, S.; Zhang, J.; Li, H.; Lin, J. M. Strategy for Signaling Molecule Detection by Using an Integrated Microfluidic Device Coupled with Mass Spectrometry to Study Cell-to-Cell Communication. *Anal. Chem.* **2013**, *85* (2), 868–876.

(113) Li, Y.; Sella, C.; Lemaître, F.; Guille-Collignon, M.; Amatore, C.; Thouin, L. Downstream Simultaneous Electrochemical Detection of Primary Reactive Oxygen and Nitrogen Species Released by Cell Populations in an Integrated Microfluidic Device. *Anal. Chem.* **2018**, *90* (15), 9386–9394.

(114) Tavakolian-Ardakani, Z.; Hosu, O.; Cristea, C.; Mazloum-Ardakani, M.; Marrazza, G. Latest Trends in Electrochemical Sensors for Neurotransmitters: A Review. *Sensors (Switzerland)* **2019**, *19* (9).

(115) Das, P.; Das, M.; Chinnadayyala, S. R.; Singha, I. M.; Goswami, P. Recent Advances on Developing 3rd Generation Enzyme Electrode for Biosensor Applications. *Biosensors and Bioelectronics*. Elsevier Ltd May 15, 2016, pp 386–397.

(116) Bang, S.; Jeong, S.; Choi, N.; Kim, H. N. Brain-on-a-Chip: A History of Development and Future Perspective. *Biomicrofluidics* **2019**, *13* (5), 51301.

(117) Schmelzeisen-Redeker, G.; Schoemaker, M.; Kirchsteiger, H.; Freckmann, G.; Heinemann, L.; Del Re, L. Time Delay of CGM Sensors: Relevance, Causes, and Countermeasures. *J. Diabetes Sci. Technol.* **2015**, *9* (5), 1006–1015.

(118) Bergman, J.; Mellander, L.; Wang, Y.; Cans, A.-S. Co-Detection of Dopamine and Glucose with High Temporal Resolution. *Catalysts* **2018**, *8* (1), 34.

(119) Rebrin, K.; Sheppard, N. F.; Steil, G. M. Use of Subcutaneous Interstitial Fluid Glucose to Estimate Blood Glucose: Revisiting Delay and Sensor Offset. *J. Diabetes Sci. Technol.* **2010**, *4* (5), 1087–1098.

(120) Jansson, P. A.; Fowelin, J.; Smith, U.; Lonnroth, P. Characterization by Microdialysis of Intercellular Glucose Level in Subcutaneous Tissue in Humans. *Am. J. Physiol. - Endocrinol. Metab.* **1988**, *255* (2 (18/2)).

(121) Rebrin, K.; Steil, G. M. Can Interstitial Glucose Assessment Replace Blood Glucose Measurements? *Diabetes Technol. Ther.* **2000**, *2* (3), 461–472.

(122) Lipman, R. L.; Raskin, P.; Love, T.; Triebwasser, J.; Lecocq, F. R.; Schnure, J. J. Glucose Intolerance during Decreased Physical Activity in Man. *Diabetes* **1972**, *21* (2), 101–107.

(123) Sarelius, I. H.; Duling, B. R. Direct Measurement of Microvessel Hematocrit, Red Cell Flux, Velocity, and Transit Time. *Am. J. Physiol. - Hear. Circ. Physiol.* **1982**, *12* (6).

(124) Pasarica, M.; Sereda, O. R.; Redman, L. M.; Albarado, D. C.; Hymel, D. T.; Roan, L. E.; Rood, J. C.; Burk, D. H.; Smith, S. R. Reduced Adipose Tissue Oxygenation in Human Obesity Evidence for Rarefaction, Macrophage Chemotaxis, and Inflammation without an Angiogenic Response. *Diabetes* **2009**, *58* (3), 718–725.

(125) Lillioja, S.; Young, A. A.; Culter, C. L.; Ivy, J. L.; Abbott, W. G.; Zawadzki, J. K.; Yki-Järvinen, H.; Christin, L.; Secomb, T. W.; Bogardus, C. Skeletal Muscle Capillary Density

and Fiber Type Are Possible Determinants of in Vivo Insulin Resistance in Man. *J. Clin. Invest.* **1987**, *80* (2), 415–424.

(126) Ward, W. K.; Troupe, J. E. Assessment of Chronically Implanted Subcutaneous Glucose Sensors in Dogs: The Effect of Surrounding Fluid Masses. *ASAIO J.* **1999**, *45* (6), 555–561.

(127) Gifford, R. Continuous Glucose Monitoring: 40 Years, What We′ve Learned and What's Next. *ChemPhysChem* **2013**, *14* (10), 2032–2044.

(128) Henninger, N.; Woderer, S.; Kloetzer, H.-M.; Staib, A.; Gillen, R.; Li, L.; Yu, X.; Gretz, N.; Kraenzlin, B.; Pill, J. Tissue Response to Subcutaneous Implantation of Glucose-Oxidase-Based Glucose Sensors in Rats. *Biosens. Bioelectron.* **2007**, *23* (1), 26–34.

(129) Sharkawy, A. A.; Klitzman, B.; Truskey, G. A.; Reichert, W. M. Engineering the Tissue Which Encapsulates Subcutaneous Implants. I. Diffusion Properties. *J. Biomed. Mater. Res.* **1997**, *37* (3), 401–412.

(130) Novak, M. T.; Reichert, W. M. Modeling the Physiological Factors Affecting Glucose Sensor Function in Vivo. *J. Diabetes Sci. Technol.* **2015**, *9* (5), 993–998.

(131) Zou, C.; Wang, Y.; Shen, Z. 2-NBDG as a Fluorescent Indicator for Direct Glucose Uptake Measurement. *J. Biochem. Biophys. Methods* **2005**, *64* (3), 207–215.

Ethan S. McClain

4507 Guy Court, Old Hickory, TN | 615-477-2880 | ethan.s.mcclain@vanderbilt.edu

EDUCATION

Vanderbilt University Nashville, TN
Ph.D. in Chemistry **2021**

University of Tennessee Knoxville, TN
B.S. in Chemistry **2016**

RESEARCH EXPERIENCE

Vanderbilt University Nashville, TN

Graduate Researcher with Dr. David E. Cliffel **2016 – Present**

Dissertation: Development and Application of Enzymatic Biosensors in the Investigation of Organophosphate Toxicity and Neurotransmission

- Developed and applied biosensors to the real-time detection of neurotransmitters, uncovering abnormal glutamate uptake in astrocytes from those with tuberous sclerosis complex disorder
- Led analysis team of 4 people in the completion of research milestones and the creation of deliverables for both EPA- and IARPA-funded projects
- Created MATLAB-based automated data analysis program—providing for a more efficient and robust analysis process, and allowing flexibility in experimental design
- Mentored/trained undergraduate and graduate students in the successful completion of research projects
- Published 3 papers in nationally recognized journals across multiple disciplines and presented research at conferences throughout the United States

University of Tennessee Knoxville, TN

Undergraduate Researcher with Dr. Mark D. Dadmun **2015 – 2016**

- Determined of the structure of star block copolymers through modeling small angle x-ray scattering data

LEADERSHIP EXPERIENCE

Vanderbilt Chemistry Department Nashville, TN

Discussion Leader **2019**

- Prepared and directed weekly discussions with undergraduate students to aid comprehension of class material through solving problems

Teaching Assistant **2016 – 2018**

- Prepared and presented weekly lectures, managed laboratory space, and assisted students in performing experiments

PUBLICATIONS

- **McClain, E. S.**, Miller, D. R., & Cliffel, D. E. (2019). Microfluidic Electrochemical Acetylcholine Detection in the Presence of Chlorpyrifos. *Journal of The Electrochemical Society*, *166*(16), G178–G181.
- Miller, D. R.*, **McClain, E. S.***, & Cliffel, D. E. (2018). Electrochemical Microphysiometry Detects Cellular Glutamate Uptake. Journal of The Electrochemical Society, 165(12), G3120–G3124.
  *co-first authors
- McClatchey, P.M., **McClain, E. S.**, Williams, I. M., Malabanan, C. M., James, F. D., Lord, P. C., Gregory, J.M., Cliffel, D.E. & Wasserman, D. H. (2019). Fibrotic Encapsulation Is the Dominant Source of Continuous Glucose Monitor Delays. *Diabetes*, *68*(10), 1892–1901.

MANUSCRIPTS IN PREPARATION

- Miller, D.R., **McClain, E.S.**, Dodds, J.N., Balinski, A., May, J.C., McLean, J.A., & Cliffel, D.E. (2020) Chlorpyrifos Disrupts Acetylcholine Metabolism Across Model Blood-Brain Barrier. *Frontiers in Bioengineering and Biotechnology.* Under Review.
- Miller, D.R., Schaffer, D.K., Neely, M.D., **McClain, E.S.**, Travis, A.R., Block, F.E., McKenzie, J.R., Werner, E.M., Armstrong, L.C., Bowman, A., Ess, K.C., Wikswo, J.P., & Cliffel, D.E. A Bistable, Multiport Valve Enables Microformulators Creating Microclinical Analyzers That Reveal Aberrant Glutamate Metabolism in Astrocytes Derived from a Tuberous Sclerosis Patient. *Sensor & Actuators: B. Chemical.* Under Review.
- **McClain, E.S.**, Xu, K., Miller, D.R., & Cliffel, D.E. Development of a Biosensor for the Simultaneous Detection of Multiple Neurotransmitters. In preparation for *Analytical and Bioanalytical Chemistry.*
- Tasneem, K.M., **McClain, E.S.**, Cliffel, D.E., & Hutson, S.M. Modeling Downstream Electrochemical Analysis of an Organ-on-a-Chip System. In Preparation.

PRESENTATIONS

- **McClain E.S.**, Miller, D.R., Brown, J.A., Wikswo, J.P., & Cliffel, D.E. (2019, October) Effects of Chlorpyrifos Exposure on Acetylcholine Metabolism Across a Model Blood-Brain Barrier. Presented at the 236th meeting of the Electrochemical Society, Atlanta, GA.
- **McClain E.S.**, Miller, D.R., Brown, J.A., Wikswo, J.P., & Cliffel, D.E. (2019, August) Effects of Chlorpyrifos Exposure on Acetylcholine Metabolism Across a Model Blood-Brain Barrier. Presented at the Gordon Research Conference for Cellular and Molecular Mechanisms of Toxicity, Andover, NH.

- **McClain E.S.**, Brown, J.A., Wikswo, J.P., & Cliffel, D.E. (2018, October). Effects of Organophosphates on Acetylcholine in a Model Blood-Brain Barrier System. Presented at the 70th regional meeting of the American Chemical Society, Augusta, GA.